A Near Wake Study of Vortex Shedding from Bluff Bodies at Low Reynolds Numbers

Anne Emily Corlett

Doctor of Philosophy
University of Edinburgh
1996

Declaration

I declare that this thesis was composed by me and that the work contained therein is my own, except where explicitly stated otherwise in the text.

(*Anne Emily Corlett*)

To my parents

Abstract

Vortex shedding in the near wakes behind a flat plate and a circular cylinder is studied for Reynolds numbers, R, between 80 and 235. Particle Image Velocimetry (PIV) is used to generate velocity maps of the surface flow from which the vorticity fields are found.

The majority of results are taken within the two-dimensional shedding regime for which $R < 180$. Vortex strength calculations of the Karman vortices show that there is little variation of this quantity with Reynolds number for both bodies, and that, for a circular cylinder, there is no discontinuity at a Reynolds number of 100 as found by Green & Gerrard (1991). When the Reynolds number is increased to above 180, no major changes are found. However, dye visualisations of the flow within the water indicate the presence of three-dimensional transitional modes.

The effect of rotation, at Reynolds numbers 100 and 200, on the vortex shedding from a flat plate is also investigated. All the flow characteristics are modified by the rotation. As the ratio of rotational to translational velocity (spin parameter, S) is increased the vortices become weaker and the wakes become increasingly asymmetrical. At Reynolds number 100, vortex shedding ceases by $S = 2.4$. Examination of the mean streamwise velocity profiles shows that the velocity deficit decreases with increasing spin parameter, and indeed for $S = 4.5$ and $Re = 100$, the mean velocity has a jet profile. Thus rotation is shown to be an effective means of wake control.

Acknowledgements

First of all I would like to thank Francis Barnes for his advice and guidance. Not only has he encouraged me over the past few years but also has been a generous provider of much appreciated chocolate digestives. I would also like to thank the people who have helped me whilst I've been in the Physics Department at Edinburgh University, especially Frank Morris.

Finally, I want to thank Rob Payne for reading this thesis and all those who have helped make my time in Edinburgh so enjoyable.

Table of Contents

Chapter 1

General Introduction

1.1 General Background

1.1.1 Subject Background

Vortex shedding is a phenomenon which often occurs when a bluff, or non-streamlined, body is placed in a flow. Coherent structures can form downstream from such bodies as telephone wires, chimneys and islands. Vortices form in the wakes of these bodies if the flow velocity, when scaled with respect to the body size, is above a value of approximately 50. This normalised quantity is known as the Reynolds number and is used extensively in periodic flow studies. It is found that bluff bodies are subject to vortex shedding in flows with Reynolds numbers up to approximately 10^7.

At moderate Reynolds numbers, vortices are shed alternately from either side of the body and form an ordered system, commonly referred to as the von Karman vortex street, in the wake. Initial studies of vortex streets were made by Strouhal [91] (from Williamson [109]) in 1878 in his examination of Aeolian tones; the sounds produced by wind over wire in an 'Aeolian harp'. However it is after von Karman, who in 1912 studied the stability of such configurations, that the streets are named.

Since these early studies, there has been sustained interest in bluff body wakes. They are complex systems which have been described by Morkovin [66] as containing

> a *kaleidoscope of challenging fluid phenomena*

Many fundamental questions are posed by these flows such as the nature of the instability which initiates the shedding process and the mechanism of vortex for-

mation. However, it is not only from an esoteric viewpoint that bluff body wakes are of interest since they are also of considerable significance to many aspects of engineering design. The alternate nature of vortex shedding results in a periodic loading on structures which produces vibrations which can lead to structural failure. It was the omission of such considerations in the design of the infamous Tacoma Narrows bridge which led to its collapse in 1947.

There are many reviews of bluff body flows, amongst which are those of Berger & Wille [8], Bearman [7] and Williamson [110].

1.1.2 Thesis Focus & Development

This thesis is concerned with the flow at low Reynolds number over a stationary flat plate and a circular cylinder. The wake behind a flat plate rotating about its axis of symmetry is also examined.

The primary investigative technique used throughout the study was Particle Image Velocimetry (PIV). PIV enables the instantaneous velocity field of the flow to be mapped thus, when translated to a vorticity field, it avoids the reference frame problems commonly associated with flow visualisations (Perry, Chong & Lim [75]).

Initially the focus of study was the effect of rotation on the vortex shedding process. It will be shown that as with other forms of wake control, simultaneously rotating and translating a body manipulates the wake structures such that the forced flow is significantly different from the unforced case. As a precursor to this investigation, a purely translating plate was to be studied. To date there have been relatively few experimental studies concerned with the laminar flow from this body (refer to Chapter 4). Hence the purpose of this investigation was to check both the PIV system and to provide new information about the shedding from a normal flat plate. However, as will be discussed later, the results of this exercise showed that it would be both interesting and useful to pursue this study further and to encompass, in addition, the flow from a circular cylinder.

The remainder of this chapter gives a background to wake flows. Although only two shedding regimes will be examined in this study, there are several others which act throughout a large Reynolds number range and these are discussed below. Common methods of wake control are also described. Finally there is a

brief description of the contents of this thesis.

1.2 Vortex Shedding Regimes: An Overview

The nature of the wake from a bluff body varies with Reynolds number. This variation can be catagorised into several, distinct regimes which are usually defined by 'mean' flow measurements such as the shedding frequency or base pressure. Generally the regimes are associated with certain Reynolds number ranges. The following regime terminology comes from a review by Williamson [109] and, except where stated otherwise, the reference body is a circular cylinder.

1.2.1 'Laminar Steady' Regime

This consists of a recirculation region containing two symmetrical eddies behind the body. For both a normal flat plate and circular cylinder, the length of the wake bubble grows linearly with Reynolds number (Fornburg [24], Hudson & Dennis [45] and Dennis *et al* [17]).

For the flow from a normal flat plate, Taneda [96] (from [45]) experimentally found that such eddies appeared at $Re = 0.4$ whilst Miyagi [62] calculated that the flow separated from the plate edges for any small but finite Reynolds number. Similarly, Hudson & Dennis [45] numerically found eddies at their lowest Reynolds number of 0.1. In contrast, there are no eddies behind a circular cylinder until a Reynolds number of 5 (Taneda [95]). Coutanceau & Bouard review low Reynolds number flows from a circular cylinder in [14].

As the Reynolds number is further increased, the wake starts to oscillate and a sinuous pattern is visible downstream of the body. Coutanceau & Bouard [14] defined the critical Reynolds number for this behaviour as being that at which there is an asymmetry in the two rear eddies. They found that this occurred at $Re = 34$ for a circular cylinder. This value was confirmed by Gerrard [28]. Both Taneda [96] and Arakaki [1] (both from Dennis *et al* [17]) gave a value of $Re = 25$ for the point of oscillation of the wake behind a normal flat plate.

1.2.2 'Laminar Vortex Shedding' Regime

This region extends from $Re = 49$ to approximately 180, the upper limit of this region is subject to much study which will be discussed later. Near the lower limit, the wake bubble becomes unstable, breaks down and vortices alternately

shed from the body. This instability is a global absolute instability and more details will be given in Chapter 4.

The two-dimensionality of the flow within this regime is sensitive to boundary conditions which can be manipulated to give different shedding modes (refer to Chapter 4).

1.2.3 'Three-Dimensional Wake Transition' Regime

At $Re \approx 180$ the wake becomes unstable to three-dimensional modes and undergoes a secondary instability. There is considerable scatter in the experimental values for this second critical Reynolds number (Williamson [110]) but recent three-dimensional stability analysis by Henderson and Barkley [5, 43] gave a value of $Re = 188.5 \pm 1.0$. This instability is intrinsic to the flow and is different from the three-dimensionalities due to experimental conditions.

The secondary instability is manifested by the appearance of streamwise vortices whose wavelength decrease as the Reynolds number is increased to approximately 250. These two shedding modes are known as mode A and mode B and will be discussed in greater detail in Section 4.5.

1.2.4 Shear-Layer Transition' Regime

Prior to this regime, between Reynolds numbers of approximately 270 to 1000, the three-dimensional structures become more disordered. This results in a decrease in the Reynolds stresses and hence base suction (Williamson [109]) and an increase in the formation length (Unal & Rockwell [104]).

As the Reynolds number is increased, the separating shear layer becomes unstable . There is a large disparity in the literature for values of the critical Reynolds number for this transition (Prasad & Williamson [77]). Prasad & Williamson investigated Re_{crit} and found that, as with laminar vortex shedding, the shear-layer is greatly influenced by boundary conditions. For parallel shedding (refer to Chapter 4), Prasad & Williamson found $Re_{crit} \approx 1200$. The frequency of the shear layer vortices are generally considered to scale as $Re^{0.5}$ however, re-examination of previous data together with their own, led Prasad & Williamson to propose that the frequency scaled as $Re^{0.67}$.

The transition position within the shear layers moves upstream as the Reynolds number is further increased (Schille & Linke [86] from [77]). This regime is present up to a Reynolds number of approximately 200,000.

1.2.5 'Asymmetric' & 'Symmetric Reattachment' Regimes

These two regimes are present between Reynolds numbers of approximately 2.10^5 and 10^6. In the former regime a separation-reattachment bubble forms behind the body which leads to a narrow wake and a decrease in the drag. In the latter, or 'super-critical', regime two separation bubbles form and the flow is symmetric.

1.2.6 'Boundary Layer Transition' Regime

At $Re \approx 10^6$, the boundary layer itself becomes turbulent and so transition occurs before separation. However, there is still periodic vortex shedding within this regime (for example Schewe [85]). The flow separates further upstream which leads to a higher drâg and a wider wake than in the previous regime.

1.3 Wake Control

Wake control is of considerable practical interest for several reasons. Due to the often destructive nature of vortex shedding, control is primarily discussed in the context of the elimination or reduction of the von Karman vortex street. However, there are cases in which the enhancement of vortex shedding is required such as the need to increase mixing or heat transfer behind the body or to aid combustion.

Monkewitz [64] proposed that wake control methods could be classified according to their hydrodynamic stability properties and hence fell into three catagories: **modification of the boundary conditions**; **unsteady open loop forcing** and **feedback control**. A selection of techniques within each of these catagories is discussed below.

1.3.1 Modification of the Boundary Conditions

Such control methods have been, in the majority of cases, linked to the suppression or reduction of the local absolute instability in the near wake.

Splitter Plates These have been used successfully behind circular cylinders to suppress the vortex shedding and the drag for many years since Roshko's study of 1955 [81]. Other experimental studies have been those of Gerrard [27] and Unal &

Rockwell [105] whilst, more recently, Kwon & Choi [54] numerically investigated the shedding mechanism.

Near-Wake Heating Heating the body or introducing heating wires into the near wake has been found to be effective in suppressing the shedding (Yu & Monkewitz [115], Lecordier *et al* [55]). Yu & Monkewitz suggested that this is due to a change in density of the fluid reducing the absolute instability, whilst Lecordier *et al*, in their air experiments, considered the resulting change in Reynolds number to be significant.

Base Bleed & Base Suction This reduces the reverse flow behind the body which in turn reduces the absolute instability of the wake (Monkewitz & Nguyen [65]). Base bleed is particularly effective at producing the transients used to investigate the governing instability (Schumm *et al* [87]).

Control Cylinder Strykowski & Streenivasan [92] inserted a small control cylinder into the near wake behind a larger cylinder and found that the vortex shedding was either suppressed or modified.

1.3.2 Unsteady Open Loop Forcing

This is a more complex form of control than modification of the boundary conditions since there is no longer a straightforward link to the flow's local stability properties. At present such control is considered to result from nonlinear interactions between the forcing and the global instability (Monkewitz [64], Schumm *et al* [87]). Some examples of this type of control technique follow.

Rotary Oscillation Tokumaru & Dimotakis [100] and Filler *et al* [23] were able to increase/decrease the drag, displacement thicknesses and freestream mixing by varying the frequency and amplitude of an oscillating cylinder.

Amplitude/Frequency Modulation Nakano & Rockwell excited cylinder wakes using both amplitude and frequency modulated signals ([69] and [70] respectively). Near wake manipulation was found to affect far wake structures.

Sinusoidal/Inline/Transverse Oscillations These are widely studied wake control methods and reviews can be found in Griffin & Hall [40].

1.3.3 Feedback Control

Feedback or closed loop control uses a combination of sensors and actuators to feedback information from the wake to the body or near wake so that the combined system is stable. Monkewitz [63] analytically investigated feedback control and concluded that stabilization would only be possible for a small Reynolds number range since at higher values, the feedback necessary to stabilize the most unstable mode would itself destabilize a higher mode.

Acoustic Feedback This is a common form of controlling the wake. Roussopoulis [82] was able to suppress vortex shedding up to a Reynolds number approximately 20% above the critical value at one position along the span. Suppression was not possible if the control sensor was too far downstream. Whereas Roussopoulis used a pair of loudspeakers as actuators, Huang [44] introduced the sound via slits on the cylinder's surface. He found that the position of the slits was critical for the amount of possible control.

Blowing/Suction Park *et al* [74] were able to suppress shedding at $Re = 60$ behind a cylinder but not at $Re = 80$. At the higher Reynolds number value, suppression of the primary instability mode led to destabilization of a secondary mode. As with Huang, the position of the blowers/suckers was important with regard to the actuators' effectiveness. Recently Lin *et al* [56] investigated the effect of blowing and suction using high-image-density particle image velocimetry and found that the wake structure could be altered substantially.

1.4 Thesis Content

The following is a brief overview of the content of this thesis. Chapter 2 gives details of the experimental method and also contains background information to, and a description of, the PIV technique. A variant on the traditional PIV method was used and full details are also given in Chapter 2. Chapter 3 describes the data analysis procedures employed in this study. It also includes an analysis of the errors associated with the experiments. Chapter 4 gives the results of the studies concerning simply translating bodies, a flat plate and a cylinder, and Chapter 5 is concerned with a simultaneously rotating and translating flat plate. Finally, Chapter 6 reiterates the main conclusions that can be drawn from the above studies and suggests avenues for future research.

Chapter 2

Experimental Facility & Procedures

2.1 Introduction

This chapter describes the experimental facility and procedures used in this study. The main data acquisition technique, particle image velocimetry (PIV), is considered in detail with background theory, practical considerations and error analysis being discussed.

2.2 Experimental Facility

The experimental facility at Edinburgh is described in this section. The apparatus was contained in a small laboratory with all the windows blacked out so that the PIV photography (Section 2.4) could be performed.

2.2.1 Towing Tank

All of the experiments were performed in a towing tank 2.5 m long, 0.315 m wide and 0.3 m deep. The water was filtered before entering the tank via a hose pipe at one end. At the same end as the filter, there was a slit in the tank's wall, which was used to run off the top water layer as described in 2.3.4.

2.2.2 Carriage

The carriage was 0.40 m long and ran on steel rails which were attached to the top of the tank's frame. It was set on two 'V' shaped rollers and one flat roller. The carriage was towed via a closed loop system with braided loomed steel wire driven by a stepper motor operating through a 40:1 reduction gear box. The

latter gave the carriage a continuous range of translation speeds from 2 mms^{-1} to 50 mms^{-1}. The carriage is shown in Figure 2.1.

2.2.3 Models

Two models were used for these experiments, a flat plate and a circular cylinder. The plate was made of ground flat stock and was of length 300 mm, width 10.05 mm and breadth 2.00 mm. The circular cylinder was a silver steel rod of diameter 10 mm and 300 mm long. Both models had brass collars at one end so that they could be flush fitted to the mount on the carriage which ran on a vertical dove-tailed slide. Both the flat plate and the mount can be seen in Figure 2.1.

2.2.4 Carriage Fixtures

Camera Mounting

As discussed in Section 2.4, photographing the near wake behind the bluff body was a central part of all experiments. In order to cover the largest area of this flow in the region between the body and the back of the carriage, the camera mounting was designed to enable movement in both the downstream and cross-stream directions. This flexibility was essential when the body was simultaneously translated and rotated since the wake centre line ceased to be parallel with the downstream axis. The camera with a lipped plate glued to its base was screwed on to the mount so that the camera was horizontally aligned. This arrangement meant that the camera could be replaced in the same position with great accuracy (refer to Section 2.4.2). This mounting system is shown in Figures 2.1 and 2.2.

Flashguns

The flashguns were mounted on an outrigger extension to the carriage which placed them outside the tank wall beneath the water surface. Each flashgun was attached to a slide which was screwed to the outlying rod (Figure 2.2). The height of the flashgun beneath the water surface could be adjusted by moving the slide vertically. The distance between the two flashguns was 0.13 m. The positioning criteria for the flashguns will be discussed more fully in Section 2.4.

2.2.5 Rotation System

This part of the experimental facility was used only for the experiments described in Chapter 5 where the flat plate was simultaneously translated and rotated. All rotation was about the body's vertical or z axis and was accomplished by a stepper

motor with a 10:1 reduction gear box. This motor was attached to the top of the carriage slide and is shown in Figure 2.1.

2.3 Experimental Procedures

The general procedures adopted for running the experiments are discussed here. Some procedures were executed prior to each run whereas others were only necessary before a set of runs. For all experiments, observations were made after the body had travelled approximately 600 mm. The experimental routine associated with particle image velocimetry is discussed within the context of the whole technique in Section 2.4.

2.3.1 Bluff Body Alignment

Before a set of experiments could begin, it was necessary to check that the chosen body was correctly aligned in its holding collar so that it penetrated the water surface at 90° . This was an important check since a deviation from the normal in this plane could introduce possible three-dimensionalities into the flow. For the circular cylinder this alignment could be examined by using the stepper motor to rotate the body at a continuous rate. If the motion was then viewed from above, any asymmetry was seen as a sideways oscillation of the cylinder. When the cylinder was considered to be aligned, a final check was made using the flow visualisations discussed in Section 3.4.1. If the cylinder was misaligned then the vortices were not shed parallel to the body along its length.

The procedure for the flat plate was different due to the added requirement of minimising the asymmetry in the x-y (downstream - cross-stream) plane. The first method for checking this alignment involved using a travelling microscope positioned just in front of the plate. The cross-hairs of the microscope were squared up with the edge of the plate which had been placed by eye normal to the freestream direction, and the scale reading taken. The plate was then rotated by 180° and the process repeated. Ideally, if the plates were aligned the two readings would be identical. However in practice this was extremely difficult to achieve and the entire process was extremely laborious. The plate was kept in a particular alignment if the difference between the two vernier readings was less than 0.3 mm which corresponded to a difference of less than 3% with respect to the plate diameter. For later experiments, the travelling microscope was replaced by a specially made telescope which had millimetre graduations on the viewing

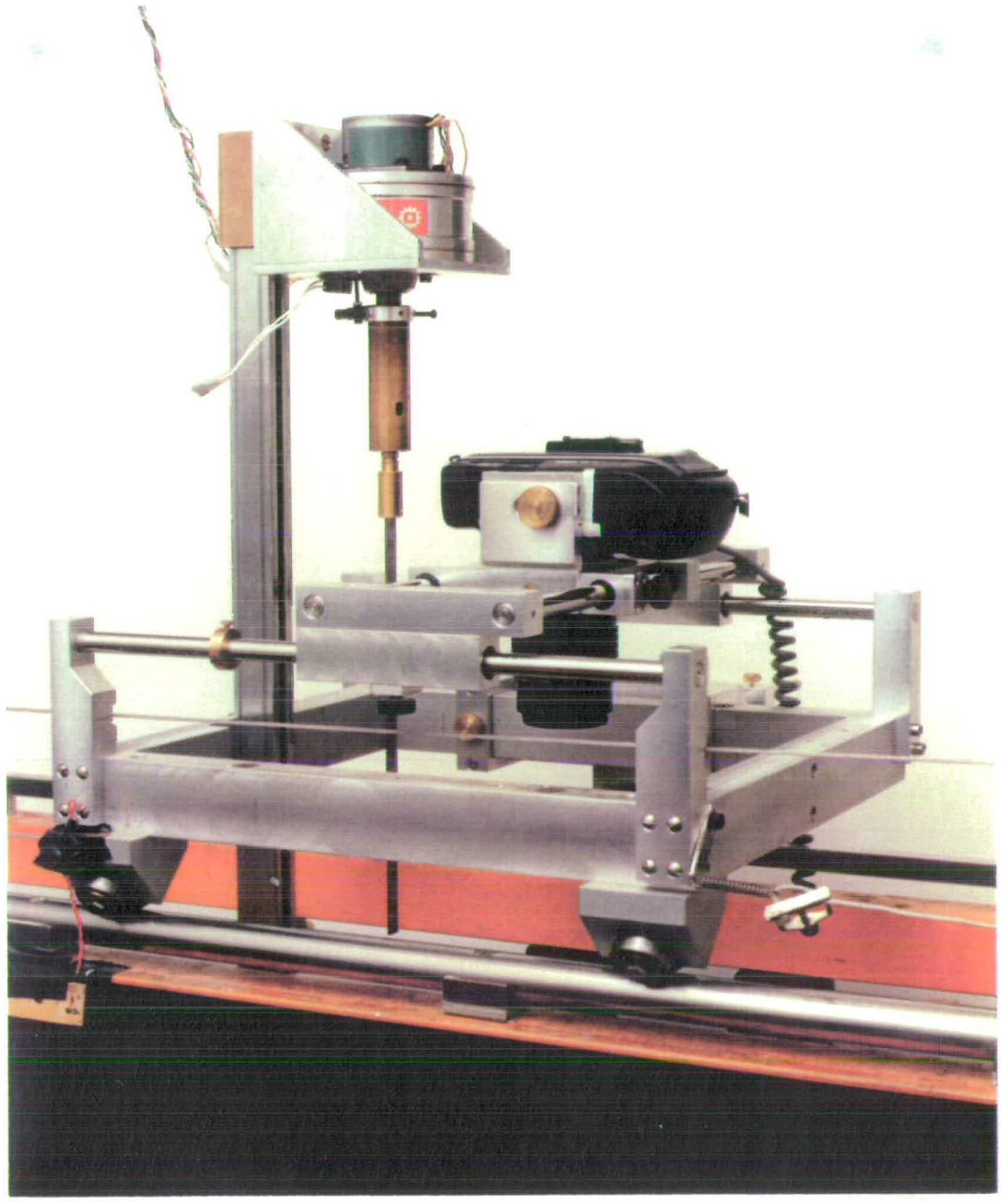

Figure 2.1: Photograph of Carriage showing Rotation & Camera Mounting Systems

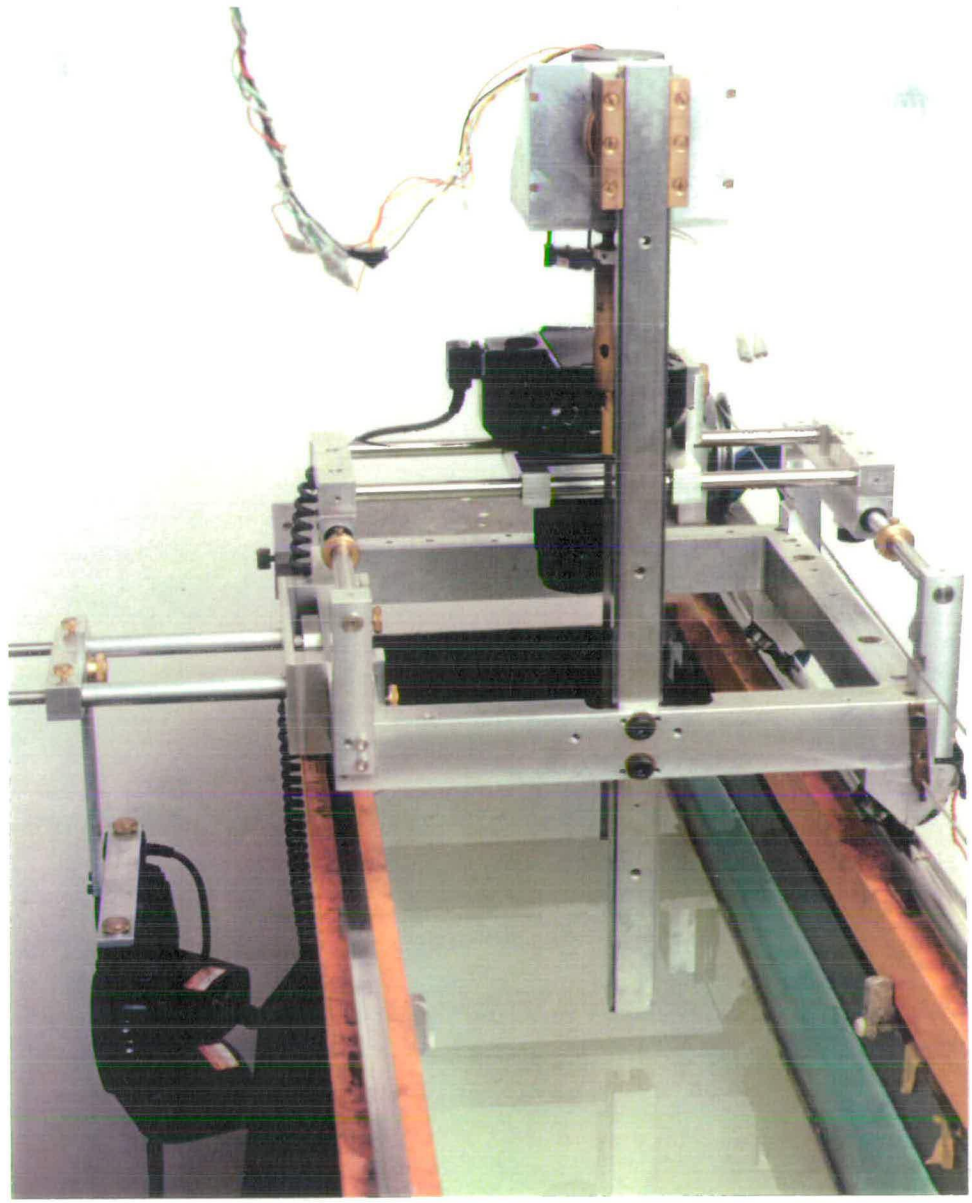

Figure 2.2: Photograph of Tank with Carriage and Flashguns

lens. This made the procedure slightly less awkward, and significantly faster, since it could be seen instantly if the deviation between the two readings was outside the accepted limits of $\pm$ 0.3 mm.

2.3.2 Field of View Calibration

Stops on the camera support allowed the camera to be returned to a fixed position each time an experiment was performed. It was therefore necessary to calibrate the distance from the body to the edge of the field of view only after a stop was newly positioned. To calibrate, a jack was raised to the height of the water after surface cleaning and placed in the tank behind the body. The water was then drained to the top of the stand. A rule was balanced on the stand so that the zero was touching the back of the body and the camera mounting placed at the stop. The distances to the start and end of the field of view could then be read off the rule. These readings gave the magnification of the lens (Section 2.4.2). This method was also used to measure the cross stream distances.

2.3.3 Rail Cleaning

In order to ensure that the carriage ran smoothly, the rails and carriage wheels were cleaned and polished for each run. This was performed just before the water surface was cleaned so that the surface was not repolluted or the bulk of water disturbed. The time between cleaning and the run was not sufficient for a significant buildup of dust to occur.

2.3.4 End Conditions

An essential condition in all experiments was for the vortices to be shed parallel to the body along the whole body length. This was of particular importance at the surface since is was critical that the surface motion was an accurate representation of the flow within the bulk of the water. To ensure that the shed vortices were undistorted and penetrated the surface vertically, the following end conditions had to be met (Slaouti & Gerrard [90]).

Top

The top end condition was of a clean water surface. This was achieved using the method described in Green & Gerrard [37]. A drop of Teepol detergent was placed on the water surface at one end of the tank and the top layer was then run off through a slit at the other end. Surface pollutants such as dirt and oil

were visible if the illumination was correct and so it was clear when the surface was clean. The tank was then left for up to three hours for the water to resettle. As in Section 2.3.3, this time was insufficient for shedding to be affected by any dirt which had reformed on the surface. A small quantity of dust on an otherwise clean water surface does not necessarily result in deformed vortices since the major contributor to the loss of two-dimensionality is oil (Green & Gerrard [37]). Resting time was needed also for the effect of the detergent on the water surface tension to decrease. It has been shown by Green [36] that after three hours the variation of surface tension with time is negligible.

The water was always drained to a constant level by the use of a marker on the glass wall of the tank. This was set at a height of 25.2 *cm* above the bottom. Care was taken to ensure that this level was reached since this was essential in keeping magnification errors to a minimum (Section 2.4.2).

Bottom

The second criterion for maximising the presence of a two-dimensional flow was the bottom end condition which required the distance between the bottom of the body and the tank to be minimised. This only needed to be performed once for each of the bodies, plate and cylinder, since the slide had a fixed lowest position. Feeler gauges were used to measure the tank-body distance (z) at various stations along the length of the tank. The tank was found to have a slightly uneven lower surface. However the distance z along the span for both bodies had a mean value of 0.22 d and was always under 0.25 d.

2.3.5 Parameter Setting

Reynolds Number

To set a particular value of Reynolds number, Re, it was first necessary to find the kinematic viscosity by taking the temperature of the water. Since the tank was not insulated, the water temperature increased from the morning run to the afternoon. However, over the short timespan of the experiment, it could be assumed that the temperature remained constant. Once the kinematic viscosity was found, the appropriate carriage velocity could then be calculated. The velocity was measured by timing the trolley's progress over a metre rule positioned just below the tank's rails.

Spin Parameter

The spin parameter, S, of a flow is the ratio of the angular to translational velocity. For experiments in which the body was rotated, S was set by calculating the correct stepper motor step frequency, τ, where

$$\tau_X = \frac{\pi d}{10 N_X U S} \tag{2.1}$$

U is the carriage velocity as calculated above, d is the body diameter and N_X the number of steps per revolution for a particular setting, X. The number of steps was multiplied by ten since a 10:1 gear box was used. Two settings were available for the stepper motor either half or full step. The latter was used only for values above $S = 2$ since the rest of the range could be covered adequately by the half step setting. The rotational period was monitored using a frequency meter.

2.4 Particle Image Velocimetry (PIV)

PIV is a non-intrusive technique which measures the velocity field of a given flow. It is accomplished by photographing a stroboscopically illuminated seeded flow such that multiple images are produced on the recording medium. The instantaneous velocities of the seeding particles and hence the carrier flow are thus encoded in the separation and orientation of these images. This velocity information is retrieved by analysing the images using a system such as the Young's fringe method as described in Section 2.4.3.

The PIV system generally used at Edinburgh University investigates the flow within an illuminated two-dimensional vertical plane through a volume of fluid. The plane is defined by a pulsed light sheet which is provided by a high powered laser directed through a scanning beam optical system. The box containing the scanning system is mounted on rails beneath the water tank allowing it to be wheeled to a particular measurement position. Details of this system may be found from several sources for example, Gray *et al* [35], and it has been highly successful in various studies conducted in specially designed wave flumes and water channels. However, the low Reynolds number work performed in this study used a smaller sized towing tank than was practical for use with this system. The tank also did not possess a glass base which is an essential requirement if the standard system is to be used. In order to eliminate the need of designing a new and complex laser delivery and light sheet production system, an alternative PIV method was used. This system utilised the two-dimensional plane inherent with

any channel flow, the surface itself. A simple, 'low tech' method was then used to illuminate the surface.

This section describes how surface PIV was used to investigate the wake flows discussed in this work. The following aspects are discussed:

- **System:** description of the surface system
- **Photograph Acquisition:** implementation of the system
- **Analysis:** conversion from image separations to velocity vectors
- **Errors:** analysis of inherent errors

2.4.1 Surface PIV System

The necessary requirements of a PIV system are

- **illumination**
- **seeding**
- **recording**

The significance and selection procedure for each of these factors will be discussed in this section.

Illumination

The presence of clear and and well-defined multiple images is extremely important if a PIV negative is to be successfully analysed (see Section 2.4.3). Although increasing the number of images increases the valid detection probability (Keane & Adrian [50]), image pairs can give good results. Image pairs are obtained if the film is exposed twice using a double pulsed illumination system. For the case described here, laser light was not necessary to illuminate the water surface. It was found that photographic flashguns were entirely satisfactory and had the additional merits of being compact and optically safe. They were also easy to traverse with the carriage and to align.

Flashguns The flashguns used were two Nikon SB-25 Speedlights. These were used in the manual mode with the flash synchronisation set at "normal" (front curtain sync). The zoom-head position was set to 24 mm which gave each flashgun a horizontal and a vertical coverage of 78° and 60° respectively. A flash output of 1/64 was used which corresponded to a flash duration of 1/23000 s.

Arrangement The flashguns were arranged so that the first flash was synchronised with the camera trigger and simultaneously a signal was sent to a delay box. After a preset interval the second flash was triggered. The delay unit was capable of delaying the pulse in 1 ms intervals from 1 ms to 999 ms. Care had to be taken to make sure that the wires within the circuit overlapped as little as possible since the resulting interference could produce an untriggered flash.

Flashgun Positioning The position of the flashguns was of prime importance to the generation of image pairs suitable for the analysis. The flow had to be evenly illuminated by both flashes with good contrast between the seeding particles and background. Finding the optimum position for the flashes was a fairly involved process since if the flashes pointed straight down on to the water surface then the film was completely overexposed with no particles visible. Lack of contrast also occurred if reflected light was used to illuminate the surface, with the flashes being fired opposite a sheet of aluminium foil. After some experimentation it was found that the best way to achieve visible particle images was to place the guns below the level of the water so that the lightsheet was below the seeding. The flashgun mount to give this position is described in Section 2.2.4. To ensure that the whole field of view was evenly illuminated, the flashgun heads were inclined at approximately 5° in the horizontal plane towards the centre of the trolley.

Seeding

Satisfactory seeding of the flow is crucial to the success of the PIV method. The selection process for finding a suitable seeding material is described by Gray [31], the primary criterion being that the seeding must passively follow the flow. A material found to satisfy these conditions was conifer pollen. This seeding was used throughout these experiments and was typically 50 μm to 70 μm in diameter and effectively neutrally buoyant. It has been shown by Quinn *et al* [79] that the pollen has a slight tendency to rise to the surface with velocities of the order of 0.25 mms^{-1}. If the fluid volume is being seeded, this effect could cause the seeding to move out of the measurement zone.

Camera

High quality optics are needed if the PIV negative is to be subjected to minimal optical distortions. The camera used in these experiments was a Nikon F4 series camera with a Nikon AF Micro-Nikkor 105mm lens. Both the ISO hot shoe

connection and sync terminal were synchronised to the shutter. High resolution black and white film Kodak T-max 100 was used throughout.

2.4.2 Acquisition of Photographs

Since the acquisition of negatives is central to the PIV technique, it is important to ensure that great care is taken at each stage of the process.

PIV Parameters

It is essential to optimise the following parameters if good, clear images and hence resolvable velocities are to be achieved. Optimum parameter values for multi-pulsed systems can be found from various sources, for example Gray [31], but these were not suitable for the flashgun illuminated, dual pulse system used here. However, a comprehensive optimisation study of the various parameters involved was performed numerically for a dual pulsed system by Keene & Adrian [49]. These parameters are discussed here.

Flash Separation Time The analysis system used in these experiments can resolve images separated by distances of between approximately 30 μm and 300 μm. With laser illumination systems, an image separation of 150 μm is desired (Gray [31]). However, it was found by experimentation that with the flashguns, fringe quality was improved if the separation was increased to 190 μm. This image separation concurs with the dual pulse results of Keane & Adrian [49]. They found that to achieve a high detection rate the maximum ratio of image separation, d_s, to beam diameter, d_i, had to be less than 0.25. With a beam diameter of 1 mm this corresponds to an image separation of $d_s < 250\mu m$. The flash separation time, in ms, was thus determined by the following equation

$$T^* = \frac{0.19}{MU} \tag{2.2}$$

where M is the real to film magnification and U the carriage velocity in ms^{-1}. For the range of Reynolds numbers covered here, the pulse intervals were typically $20ms \leq T^* \leq 60ms$. Since the duration of the flash was ≈ 0.04 ms there was no question of the two flashes overlapping with one another.

Shutter Speed This is generally determined by the number of exposures required on the film, for example six images at separations of 20 ms would require a shutter speed of at least 1/8 s. Since only two images were possible here, the shutter speed needed simply be greater than the flash separation time. There is

an upper limit to this time since it is essential that the flow does not significantly change whilst a particular frame is being exposed. A shutter speed of 1/4 s was found to be suitable for satisfying both of these conditions.

Aperture Size Finding the optimum aperture size is of some importance since this does not simply affect the exposure. Spherical aberrations are introduced if a large aperture (small F number) is used, whereas diffraction effects are increased if the aperture is very small. It has been shown by Gray *et al* [34] that the best way to balance these two factors is to use an aperture one stop down from the maximum. However, for the illumination system and camera position used here, this aperture value (f4) greatly overexposed the film making it impossible to distinguish any particle images. It was found that an aperture of f11, halfway through the range, allowed an acceptable exposure but was also a satisfactory balance between the two aforementioned extremes. A film speed of ASA rating 100 gave sufficient exposure.

Magnification

The magnification was measured using the same method as that used for the calibration of the camera's field of view (Section 2.3.2). Since the measurement technique was both very intrusive and time-consuming , the magnification was not recalibrated each time the camera was replaced on its mounting. However, great care was taken to ensure that the camera was always aligned horizontally, using a spirit level, and that the water level after draining was constant. Random checks on the magnification throughout the experimental runs found that it did not vary by more than $\approx 1\%$.

Field of View Selection

Successful analysis of a negative will only be achieved if the velocity does not change appreciably over the interrogation area. It has been found by Gray [31] that images will only be resolved if velocity differences within the interrogating area are less than 3%. A lens must be carefully chosen so that the magnification keeps the change of velocities on the film below this threshold. A 60 mm lens was used in initial experiments. This gave an extensive field of view but velocities within the vortex centres could not be resolved. A compromise between view and magnification ranges thus was made by use of the 105 mm lens mentioned in Section 2.4.1.

Seeding Density & Application

Gray [31] found that using the system described in Section 2.4.3, the optimum seeding density was such that the mean number of particle pairs in the interrogation area, N, was ≥ 6. Similarly, Lourenco & Krothapalli [58] gave an estimate of $N \geq 4$. However, Keane & Adrian [49] found that this particle density was insufficient for a double pulsed system and needed to be increased to $N \geq 15$.

A high concentration of particles was used for the study here, an estimate being $N \approx 20$. The pollen needed to be introduced to the water surface by a method which caused minimal disturbance and which gave an even coverage. It was found that the best way to achieve both of these criteria was to shake the pollen on to the surface using, as a 'pepper pot', a film container covered with a piece of fine muslin. A third of a pot of pollen was enough to give a suitable seeding density over the whole of the water surface.

Focussing on the pollen was performed by shining a lamp at an obtuse angle to the surface; direct light gave a complete 'white out' in the field of view. Although the focus was checked before every run, due to the precautions taken in Section 2.4.2, it very rarely needed altering throughout the experiments.

Camera Triggering

The camera was triggered via an external cable screwed into a synchronisation socket on the body. For the experiments when the body was simply translated with the carriage, this cable was linked to a manual triggering device and the camera was fired by hand. Triggering was automated when the bluff body was simultaneously rotated and translated since the cable was connected to a contact circuit just above the holding collar on the carriage. Pins screwed into the collar then fired the camera as they passed the contact. Up to eight phase positions per cycle were available.

Film Developing

All films were developed using T-Max solution. To increase the contrast between the particle images and the background, the stated developing time at a particular solution temperature (e.g 6.5 minutes at 24°) was increased by one minute. The tank was constantly agitated throughout this time so that the effect of image drift due to uneven development was minimised (Gray [31]). The film was then

fixed for 7 minutes using Amfix and washed for 30 minutes to ensure that all the solution was removed.

2.4.3 PIV Analysis

The aim of the analysis stage of the PIV process is to extract flow velocity information from the separation and orientation of the image particle pairs. This aim is achieved by systematically examining small portions of the negative and finding the mean displacement of the particles within these interrogation areas. Hence a whole velocity flow field can be built up. Figure 2.3 shows a sketch of a negative together with a 'magnified' view of the pairs within an interrogation area.

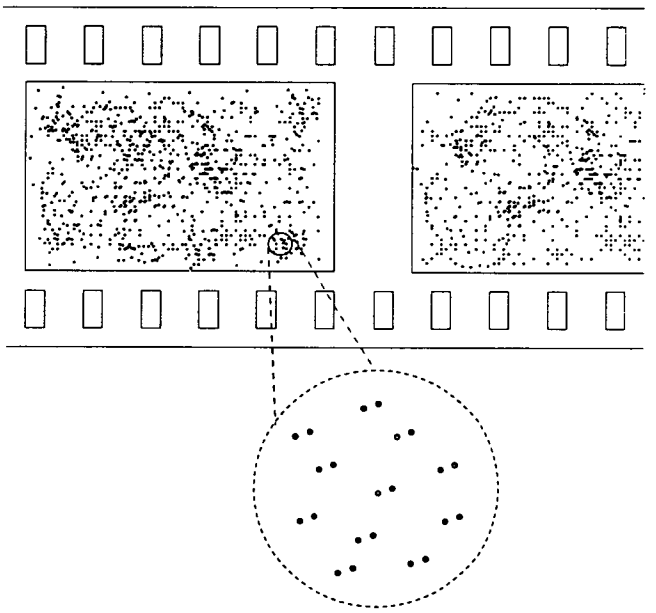

Figure 2.3: Sketch of Negative showing Interrogation Area with Particle Pairs

Theory

The mean displacement of the particle image pairs within the interrogation area is most reliably found by autocorrelation over the area. The autocorrelation function is given by

$$R(\vec{s}) = \int g(\vec{r})g(\vec{r}+\vec{s})d\vec{r} \tag{2.3}$$

where $g(\vec{r})$ is the image intensity distribution of the given area of negative and $R(\vec{s})$ the autocorrelation. This process is equivalent to performing two consecutive Fourier transforms (FTs) since by the Wiener-Khintchine or Autocorrelation theorem the autocorrelation function is simply given by the Fourier transform of

the image intensity distribution. The FTs of equation 2.4 are two-dimensional.

$$R(\vec{s}) = FT\{[FT\{g(\vec{r})\}]^2\} \tag{2.4}$$

The autocorrelation domain is dominated by the self-correlation peak of the correlation of each particle image with itself. Either side of this central peak are the signal peaks from the correlation across the interrogation area of the mean displacement. Two peaks result due to the inherent 180° directional ambiguity of PIV. Either can be used in the analysis process since they are identical. The presence of the central peak can pose some problems when analysing and so techniques for its removal are discussed later. A picture of the autocorrelation plane together with the aforementioned peaks is shown in Figure 2.4 (from Keane & Adrian [49]). In this picture, R_p is the self-correlation peak, R_{d+} and R_{d-} the signal peaks and the remainder is background noise.

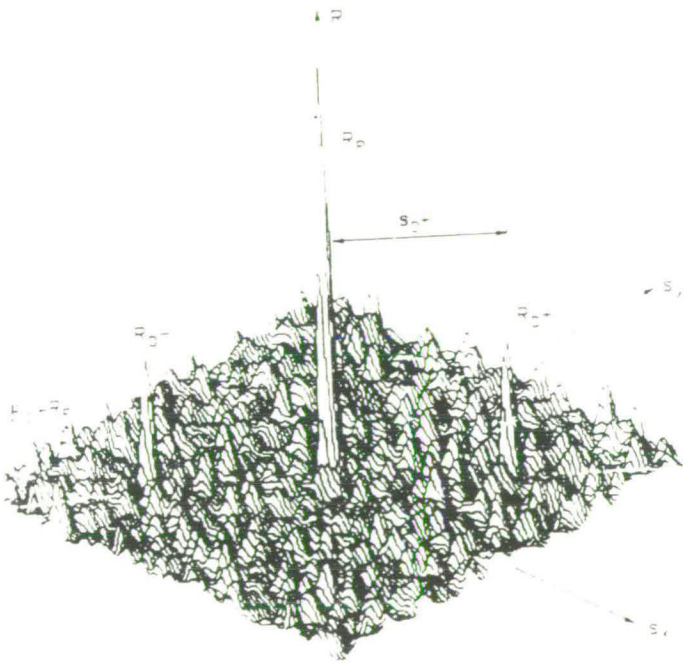

Figure 2.4: Autocorrelation Plane

Analysis System

The analysis system used in these experiments was first developed by Gray [33] and later upgraded by Skyner [89]. It performs the autocorrelation process by

first transforming optically and then digitally. The basis of the optical transform is as follows. If the negative is illuminated with spatially coherent, monochromatic light, the image pairs generate Young's interference fringes in the focal plane of a lens. The intensity of this pattern is the squared Fourier transform of the original distribution. A schematic layout of the system can be seen in Figure 2.5. The negative is mounted on computer driven x - y microtranslator

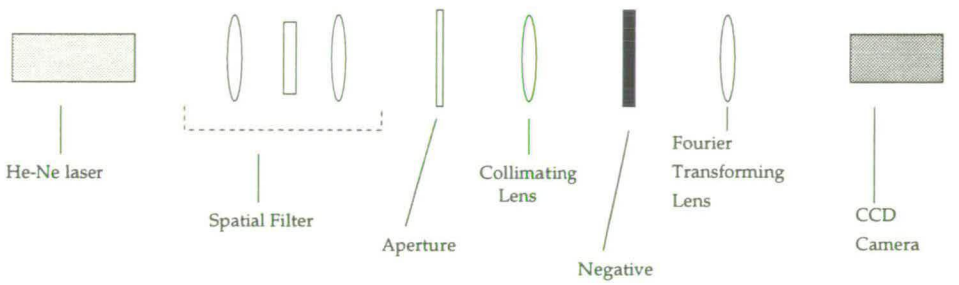

Figure 2.5: Sketch of Analysis Rig Layout

and illuminated using a coherent, collimated 1 mm beam from a low power, He - Ne laser. The beam has already passed through a spatial filter to remove high frequency noise from the assumed Gaussian beam profile. A CCD camera, placed at the focal length of the lens fixed behind the negative, collects the intensity of the fringe pattern. A frame-grabber than passes the digitised information onto a microcomputer which then performs the second Fourier transform. The separation and orientation of the signal peaks in the autocorrelation domain are located, and using the magnification and pulse delay time, the mean velocity of the particles in the interrogation beam area is calculated. The translator then moves the negative so that the next point can be examined. The time taken to analyse a point is about 2 s if a 2D FFT (Fast Fourier Transform) is performed on a 64 x 64 digitised array by a 486DX computer. The structure of the analysis program written to perform these tasks can be found in Skyner [89].

Process

The negatives were analysed on a grid which corresponded to 2 mm in real, or tank, space. This grid spacing was fine enough to give a useful number of velocity vectors for flow structural resolution but was not so fine that the analysis time for a negative was inconveniently long. A 35 mm x 24 mm format film took an average of 40 minutes to analyse with this grid spacing.

The advantage of using the Young's fringe method of analysis is that it is generally very clear before the analysis begins as to whether it is indeed worth

performing. If a negative is held in front of the interrogating laser and clear fringes are visible across the frame, it can be reasonably assumed that the velocity vectors will, on average, be resolved.

It has been previously mentioned that the central self-correlation peak may present a problem in the analysis of a negative. The reason for this is as follows. If the velocities are very small, the displacement of the primary peak from the centre will be small also and there is a chance that it will impinge on the central one. Thus the signal peaks will not be detected by the search program and so the displacement, and hence velocity vector, will not be resolved. The chance of this happening is increased also if the fringe visibility is low. It is therefore highly desirable to remove this central peak from the correlated data. This is achieved by the 'halo' facility in the pre-analysis routine. A single negative is rotated in front of the laser beam and 20 random diffraction patterns are collected and averaged by the computer. This gives an average diffraction halo, which corresponds to the pattern which would result if the negatives were singly exposed and is then subtracted from the data before the second FT is executed. Figure 2.6 shows sections through an autocorrelation plane.

Although in the top picture there would be no ambiguity in distinguishing the signal peaks since they are clearly separate from the self-correlation peak, the latter is removed by the halo function. This helps prevent the situation shown in the bottom picture, of the signal peaks impinging on the central one. In this case, the velocity would not be resolved.

An inherent problem with PIV is its 180° directional ambiguity, it cannot distinguish which image of a pair came first in time. This problem comes to the fore when the raw velocity data is to be processed since the map will have vectors pointing in random directions. However, with the flow described within this work, the flow direction is known since the camera is being translated with the carriage. Thus the velocity vectors can be aligned the correct way (from left to right) using the post-rig analysis program which again was written by Skyner [89]. For those flow situations where the flow direction is not known or where the velocity range is extremely large then it is necessary to use an image shifting system. This technique is well documented and a comprehensive study can be found in Morrison [67] which also includes a description of the inherent errors.

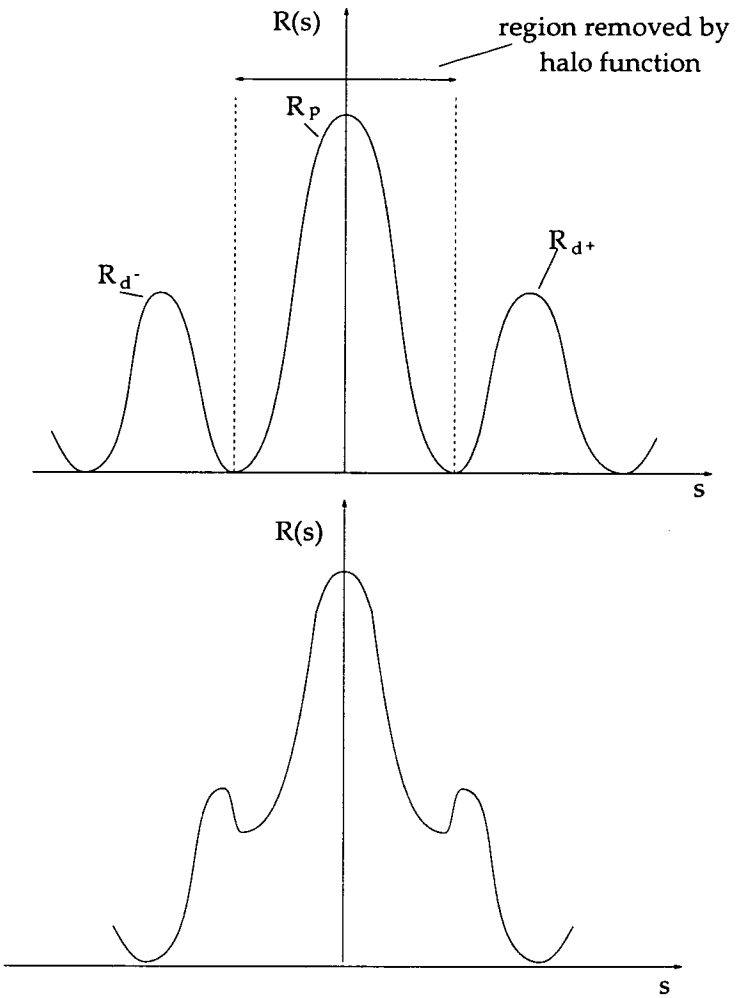

Figure 2.6: Slice through Correlation Plane showing 'Normal' and Impinging Signal Peaks

Another aspect of the post-rig analysis of vector maps is data validation. Each vector is assigned a 'quality' value which is a measure of the strength of the correlation peak as compared with the background noise. Vectors can be rejected if the quality is below a certain threshold value.

The velocity maps were manually edited to remove erroneous vectors. Although this process is very subjective, for the flow maps produced by these experiments it was usually obvious if a vector was incorrect since its magnitude was several orders either above or below the mean. Such vector dropout normally occurred if the seeding was poor in a particular area, or if the velocity gradient was too large.

2.4.4 PIV Errors

It is essential to evaluate the errors present in any experimental technique particularly if it is providing quantitative information. This section discusses the inherent errors associated with the surface PIV method and the limitations of the analysis system used.

The main sources of error may be summarised as follows:

- **Photographic Recording**
  - *Random*
    - image distortion
    - illumination interval
  - *Systematic*
    - geometric distortion
    - seeding
    - out of plane motion
- **Analysis Process**
  - *Random*
    - velocity gradients: peak broadening
  - *Systematic*
    - velocity gradients: velocity bias

Other more fundamental sources of error associated with the analysis process, such as the effects introduced by randomly sampling points from a continuous flow as described by Gray [31], have been reduced by system upgrades and can be estimated by the technique described later in this section.

Photographic Recording

Geometric Distortion As previously mentioned, a high quality Nikon lens was used which kept optical distortions to a minimum. However, to give a quantitative estimate of this error, a regular grid was photographed and the grid spacings remeasured from the developed negative. The deviation was found to be $\ll 1\%$. This compares very well with the $\leq 1\%$ deviation of the Hasselblad camera and lens which generally are used in multi-pulse, laser illuminated studies at Edinburgh University. Although this distortion value is dependent on grid accuracy and measurement, its main purpose was to provide a comparative link with the Hasselblad lens. Calibration of the analysis system is described later.

Seeding The effectiveness of the seeding following the flow is affected by three factors.

- Inertia
- Gravity
- Spatial averaging of turbulence

Since for the studies discussed here the flow is laminar, the final point above can be dismissed at once. The first two effects are significant only if there are greatly mismatched fluid/particle densities. This aspect has already been covered by Section 2.4.1 and the slight rise velocity found in some studies is not a problem here. Hence the error due to the seeding particles is negligible compared to the velocity gradient errors which will be discussed in a later section.

Out of Plane Motion If this motion is of the same order as the in plane motion then errors can be about 20% (Sinha [88]). However, an inherent assumption about the PIV work conducted here is that the flow is two-dimensional and so there is no out of plane motion. Checks were made to test this assumption, including the effect of seeding the surface, and these are described in Section 3.4.1. Hence it can be assumed that the this error is negligible.

Illumination Interval This was measured using a oscilloscope and the error on the pulse separation time was found to be $< 1\%$.

Image Distortion This is due to the effects of the recording materials used such as grain size of emulsion. These cannot be determined for a particular experiment but their overall effect on velocity measurements can be found by calibrating the analysis system. The combined error can then be used in later analysis.

Analysis Rig Calibration

The effects of various sources of error may be accounted for in this calibration which determines the accuracy with which a particle displacement in the flow is represented by an analysed vector. Both Skyner [89] and Quinn [79] have made estimates of this value and found it to be $\approx 0.1\%$. Such studies were made by generating artificial PIV negatives with particle spacings of known distance, photographing and then analysing them on the rig. Since the distortions of the Hasselblad and Nikon lenses were comparable, it is reasonable to assume that the rig calibration for the present experiments was also $\approx 0.1\%$.

Velocity Gradients

The presence of velocity gradients within a flow are responsible for both random and systematic errors in the analysed vectors. These gradients will be shown to be the major source of error in the velocity vectors generated by these experiments.

An inherent random error of the analysis process is the uncertainty in the mean particle displacement across the interrogation beam area due to the sampling of points. Although this error is primarily due to the effects of velocity gradients, the seeding density should also be considered since a low density decreases the possible number of images to be sampled. Thus, if there is a high velocity gradient in conjunction with a low seeding density, the variation of the measured displacements will be large. However, if there is only a slight velocity gradient together with a large number of particles, this variation will be much smaller. As the velocity gradient increases, the range of particle displacements also increases and the correlation peak broadens. Hence the uncertainty of finding this peak increases. The effects of these factors on the random error have investigated by Gray [31] and by Keane & Adrian [49, 50]. When using the present analysis system, the former found that for a range of velocity gradients, the as-

sociated random error was decreased greatly if, on the film, seeding densities of $\approx$ 20 particles/mm^2 were present. Increasing the density above this value did not decrease the error significantly. Using Gray [31], the random error for the experiments described here was conservatively estimated to be $\approx 1\%$. However, as discussed in Skyner [89], the random errors do not significantly affect the final velocity maps since they generally are manifested as erroneous vectors. These vectors are edited out in the post-rig processing.

Of greater significance are the systematic errors introduced by velocity gradients. If within the beam area there is a large range of velocities, the probability of finding a complete image pair with a large displacement is reduced. Hence the system is biased towards smaller velocities. This effect cannot be detected in the vector maps. Keane & Adrian [49] found that this systematic bias increased linearly with the displacement gradient within the flow. These are related to velocity gradients by

$$\frac{\partial \delta_x}{\partial x} = T^* \frac{\partial u}{\partial x} \tag{2.5}$$

for a velocity whose components are u and v in the x and y directions respectively and a pulse separation time of T^*. Displacement gradients were calculated for a number of velocity maps for flow behind the flat plate at both high and low Reynolds numbers. For wakes containing vortices, there are velocity gradients in the x and y directions hence the total displacement gradient consists of x and y gradient components where

$$\frac{\partial \delta}{\partial x} = \sqrt{\left(\frac{\partial \delta_x}{\partial x}\right)^2 + \left(\frac{\partial \delta_y}{\partial x}\right)^2} \tag{2.6}$$

$$\frac{\partial \delta}{\partial y} = \sqrt{\left(\frac{\partial \delta_x}{\partial y}\right)^2 + \left(\frac{\partial \delta_y}{\partial y}\right)^2} \tag{2.7}$$

The results of this study are shown in the form of histograms in Figure 2.7. Figures 2.7(a) and 2.7(b) have been compiled from 6 and 10 velocity maps respectively and show the fraction of points with total displacement gradients at Reynolds numbers of 80 and 180. These histograms are plotted in the manner of Skyner [89] and also show the variation of velocity bias with displacement gradient (from Keane & Adrian [49]). From these plots it can be seen that at both $Re = 80$ and $Re = 180$, the majority of points have a systematic bias of $\leq 2\%$. Using the data within these plots, the mean velocity bias at $Re = 80$ was calculated to be $\approx 1\%$ and at $Re = 180$, $\approx 1.5\%$. These values will be used later in further estimates of the velocity error.

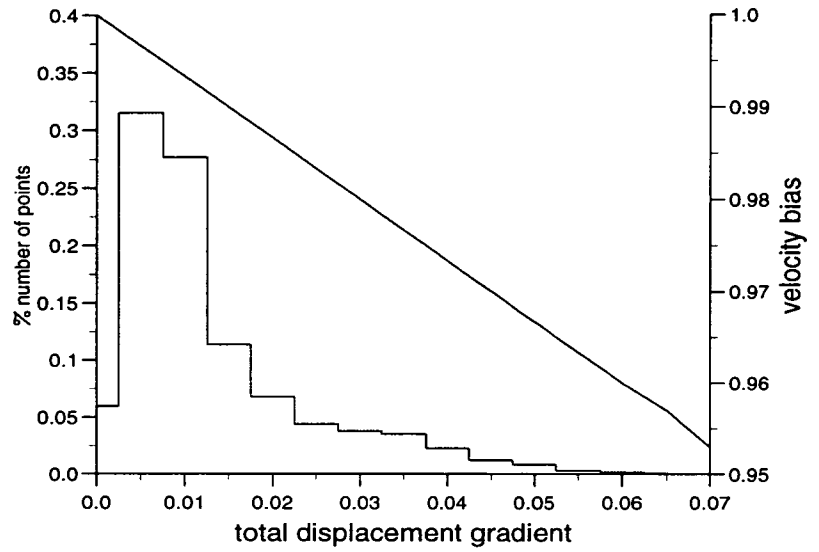

(a) $Re = 80$

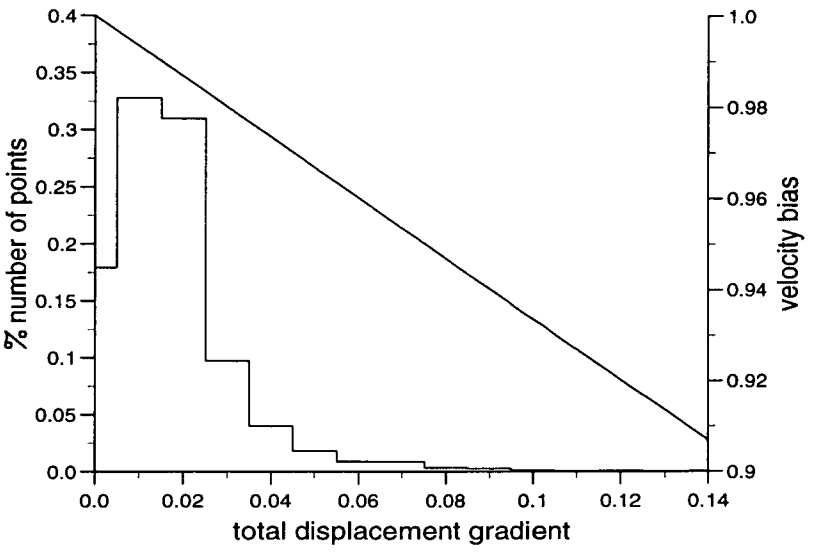

(b) $Re = 180$

Figure 2.7: Total Displacement Gradients and Velocity Bias

Chapter 3

Data & Error Analysis

3.1 Introduction

Data and error analysis are central to any experimental study. This chapter discusses the techniques used throughout this study together with an examination of their inherent problems and selection criteria. Sources of error are considered in detail and estimates are made of their combined values for various flow situations.

3.2 Post-PIV Processing

3.2.1 Velocity

The PIV technique produces a velocity vector map. This initial velocity map needs to be edited to remove spurious vectors. As discussed in Section 2.4, erroneous vectors have a magnitude and direction which differ greatly from those of the adjacent vectors. If the seeding is particularly poor over the whole frame, or if the contrast between the particle images and the background is insufficient, then large numbers of vectors can be affected. In this case, the quality factor of the vectors (refer to Section 2.4) can be used to reject those vectors with quality values below a certain threshold thus reducing manual inspection. The threshold found to be most consistent throughout these experiments was one of value 0.1.

When editing the vector maps it was found to be useful to change reference frames. The velocity maps were produced in the reference frame of the carriage and so the details of the vortices were not visible. To transform the reference frame to that of the vortices, the vortex convection velocity should have been subtracted. However, this value was not known and so the carriage velocity was subtracted instead. This transformed the reference frame to one in which the vortices' velocity was small rather than zero. In this frame, deviation of the velocity

vectors from normal vortex vector behaviour became clearer.

The data analysis procedures required a complete set of data points. Since an edited velocity map would often have several missing vectors, it was important to generate values for these points by applying an interpolation algorithm to the velocity data. This program used NAG routines E01SEF and E01SFF to interpolate and evaluate velocity vectors (Iain Morrison, private communication).

3.2.2 Vorticity

The vorticity of the vector fields of Chapter 4 was calculated, on the same grid as the PIV analysis stage, using a nearest four-neighbour scheme. For a velocity grid point at position (i,j) with velocity $(u_{i,j}, v_{i,j})$, the vorticity, $\omega_{i,j}$, at the point is given by

$$\omega_{i,j} = \frac{(v_{i+1,j} - v_{i-1,j})}{2\Delta x} - \frac{(u_{i,j+1} - u_{i,j-1})}{2\Delta y} \tag{3.1}$$

where Δx, Δy are the x, y grid separation distances. Although the latter is an adequate method for calculating vorticity, a more sophisticated program was used in later experiments (see Chapter 5). This program estimated the partial differentials by fitting a fourth order polynomial to the point (i,j) and its neighbours.

3.3 Quantitative Analysis Techniques

3.3.1 Integrated Vortex Strength: K

The vortex strength, K, is defined by integrating the vorticity values, ω, of the vortex over a given area

$$K = \int \vec{\omega}.d\vec{a} \tag{3.2}$$

where $d\vec{a}$ is the element of area over which the vorticity is being integrated. In this study $d\vec{a}$ was the square defined by the grid separations $(\Delta x \Delta y)$ which was used in the PIV analysis.

Calculation

The first vorticity summation method involved defining a perimeter around the vortex. The vorticity around this boundary was then summed and the one with the lowest total was chosen. This was an attempt to find the optimum boundary between neighbouring vortices. Once defined, the total vorticity within the perimeter was calculated. However, this technique was unsuitable for several reasons. Firstly since for simplicity of calculation the perimeter was either a square

or a rectangle, it was insensitive to the various shapes and configurations displayed by the vortices. If the flow pattern was complex then it was possible for either more or less vorticity to be added to the total than was strictly valid, thus biasing the strength. This technique was also particularly time-consuming due to the necessity of manually finding the minimum vorticity perimeter for each vortex.

To keep the biasing of the system to minimum, a summation method had to be found which allowed for variable vortex shapes. This was achieved by a computer program which only summed those points which had a vorticity above a certain boundary value. This method ensured that only those points within the vortex with vorticities higher than a desired minimum were included in the summation. When the program was run, a picture of the grid points summed was drawn to screen. This helped with the vortex selection process. The selection of the optimum boundary condition is discussed next.

Boundary Selection

Before the integrated vortex strength could be used as a means of characterising a vortex, it was essential to determine the vortex boundary, or minimum value of vorticity above which the integration of equation 3.2 took place. Strictly this area is defined by the zero vorticity contour, however in practice this was not a feasible choice due to presence of background vorticity. It therefore was necessary to define another, seemingly more arbitrary, boundary. The criteria for finding the optimum boundary were considered to be

- *consistency*: the boundary had to give satisfactory results over the widest range of flow conditions
- *simplicity*: the boundary needed to be straightforward in order to deal with large quantities of data

An initial method of defining the boundary was to use a fixed value of vorticity for all Reynolds number. This value was chosen so that for a range of Reynolds numbers the value of this vorticity contour was both above that of the background vorticity and at least half the value at the vortex centre. This was a simple method for finding the vortex boundary but it did not give consistent results. It will be shown from experimental data (Chapter 4) that a vortex formed at a high Reynolds number is stronger than one formed at a lower number, and so to use a common contour value as the boundary does not accommodate this significant difference. It therefore was necessary to find a boundary condition which was

based on the global properties of the general flow, such that it depended on the maximum vorticity of a vortex and also on the background vorticity.

Maximum Vorticity Vortices have often been modelled by an Oseen vortex. This model will be discussed in more detail later (Section 4.4). It consists of a potential vortex with a viscous core and its strength, K, and vorticity at time, t, and position $\vec{r}$ can be written as

$$K = K_0\{1 - e^{-r^2/4\nu t}\} \tag{3.3}$$

$$\omega = \omega_{max} e^{-r^2/4\nu t} \tag{3.4}$$

where K_0 is the strength at zero time and ω_{max} is the maximum vorticity. If, for a given vortex, a value of $\omega/\omega_{max} = X$ is used to define the boundary, then the strength from equation 3.3 is $K = (1 - X)K_0$. Thus, the strength of an Oseen vortex is directly related to the fraction of its maximum vorticity used as the boundary value.

It was assumed initially that the vortices produced in these experiments were of the Oseen type and so a suitable choice of boundary condition was a fixed percentage, X, of the maximum vorticity, ω_{max}, of each vortex. This condition ensured that for all the vortices, $(100 - X)\%$ of their total strength, K_0, was calculated. Thus it was possible to extrapolate the strength back to K_0.

Figure 3.1 shows how the integrated vortex strength varies with the fractional value of the maximum vorticity chosen to define the boundary of the vortex. The strengths of two vortices from the same vorticity field are shown on each graph. It is clear that the variation is linear at least up to a value of 10% ω_{max}. Thus the real vortices behave as Oseen ones.

Another reason for using ω_{max} as the scale for the boundary value was that it was easy to find. The fraction of the maximum vorticity was chosen to be 10%. This value was chosen because, for a sample of different Reynolds number flows, it was sufficiently below the peak to prevent encroachment into the inner vorticity contours but sufficiently high to be above the background vorticity which was typically 0.1 - 0.3 s^{-1}

Background Vorticity A contour value just above the background vorticity level can be used as the boundary for vorticity integration. The principal problem

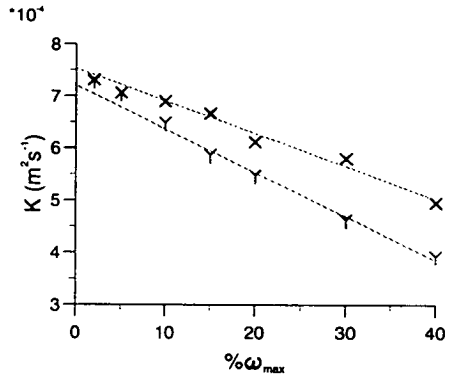

(a) Plate: $Re = 100$

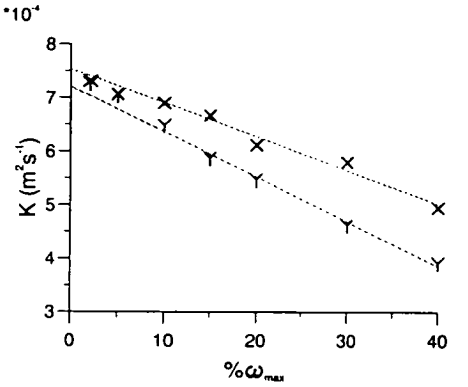

(b) Plate: $Re = 180$

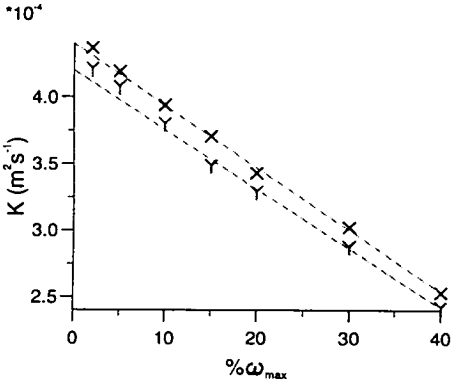

(c) Cylinder: $Re = 120$

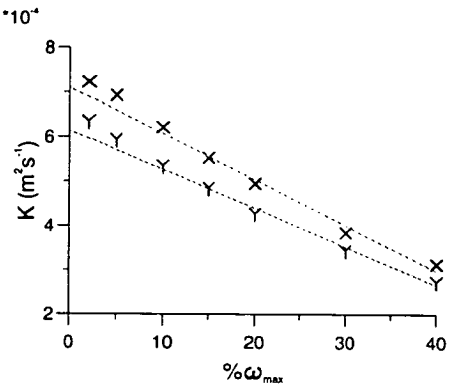

(d) Cylinder: $Re = 180$

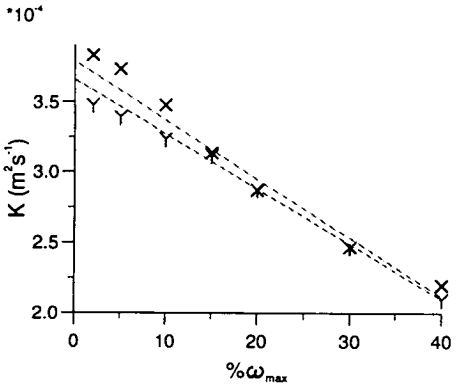

(e) Plate: $Re = 100$, $S = 0.3$

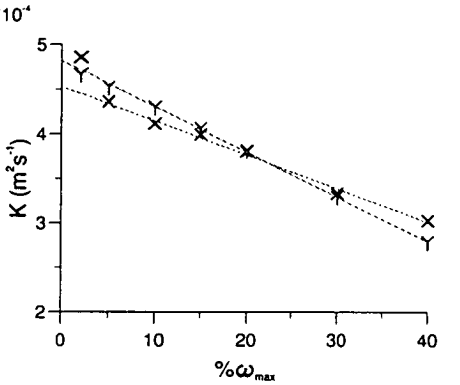

(f) Plate: $Re = 200$, $S = 1$

Figure 3.1: Variation of Vortex Strength with Boundary Value (Percentage of Maximum Vorticity): X = vortex 1; Y = vortex 2 where $x/d(1) < x/d(2)$

with this method is determining the background vorticity. One method is to examine vorticity profiles through the centre of the vortices. Figure 3.2 shows the variation of vorticity with with cross-stream distance for four vorticity maps, two each for Reynolds numbers 100 and 180. Each plot shows the profiles of two vortices from the same frame but at different downstream positions.

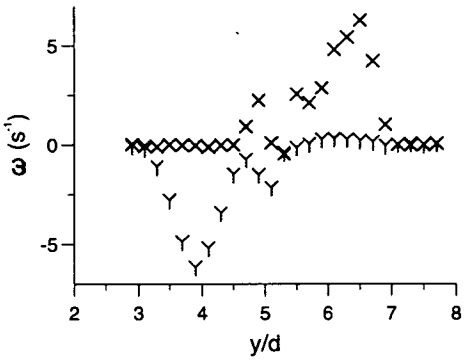

(a) $Re = 180$

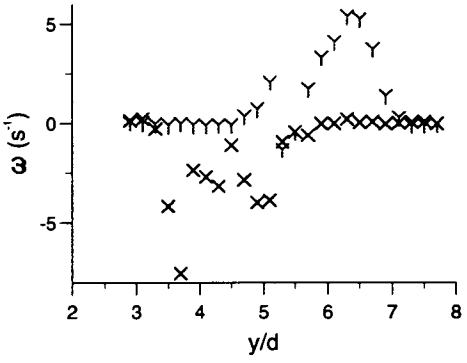

(b) $Re = 180$

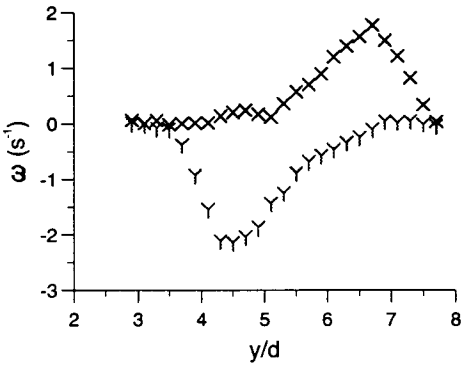

(c) $Re = 100$

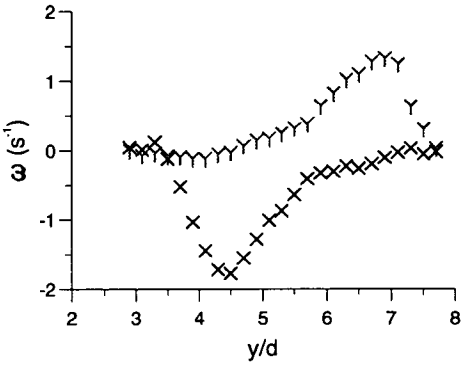

(d) $Re = 100$

Figure 3.2: Variation of Vorticity with Cross-stream Distance

The plots for these numbers are very different. Figures 3.2(a) and 3.2(b) for $Re = 180$, have sharp peaks which drop off to values of $\omega \approx 0$ whilst Figures 3.2(c) and 3.2(d) for $Re = 100$ have more gradual gradients with the possible background ranging from $\omega \approx 0$ to $\omega \approx 0.25\ s^{-1}$. Hence choosing a value for the background from these graphs is somewhat arbitrary.

A small deviation in the boundary vorticity value can have a critical effect on the vortex strength. For example at Reynolds number 100, using a vorticity

value of 0.5 s^{-1} as the summation boundary, gives a strength $\approx 3\%$ different from that using a boundary value of 0.2 s^{-1}. If these values are then used for summation boundaries at Reynolds number 180, the difference in strength increases to $\approx 6\%$. This is due to the larger vorticity gradient at $Re = 180$ because a small increase in the vorticity summation boundary will exclude proportionally more points from the summation than at $Re = 100$.

Using the background vorticity removes the error associated with using a single value of vorticity (ω_{max}) as the boundary level for a given summation. However, the possible large variation of strength values described above does not make this method a significantly better choice. Although the technique could be refined, at present it is more inconvenient and time-consuming than that of the maximum vorticity.

Choice of Routine After reviewing the cases described above, the best choice of boundary value was considered to be 10% of the maximum vorticity of a vortex.

Filtering

Once the vortex strengths of a set of vortices had been calculated, it was often necessary to filter out certain values. This process used the picture facility of the vorticity summation program. Vortices were rejected if the picture showed that excessively large numbers of points had been included in the summation (points which could not be considered as being part of the vortex). This problem occurred more often at low rather than high Reynolds numbers when the difference between the background vorticity and the boundary value was very small. Other causes for rejection were if points in the vortex centre were missing from the summation or if too few points were included. After filtering, the vortex strengths for a set of data were averaged. This was the value then used in further data analysis.

3.3.2 Circulation: Γ

The circulation of a vortex is given by

$$\Gamma = \oint \vec{u}.d\vec{\ell} \tag{3.5}$$

where $d\vec{\ell}$ is the unit length over which the velocity is being integrated. In practice, this length was either the x or y grid separation distances. A vortex's circulation is equivalent to its integrated strength if the same circuit is used for each. As with K, it is critical to find the optimum boundary for the calculation so that

values for the circulation are consistent for a wide range of wake conditions. The main advantage circulation calculations have over integrated strengths is that their inherent error is lower (Section 3.4.3).

Boundary Selection

The problems encountered with regular perimeters have already been discussed (Section 3.3.1). Various boundary conditions were tested and comparisons made with the vortices' integrated strengths as calculated using the 10% ω_{max} boundary. For a vortex at position (i, j) the first circuit tried was $(i \pm \frac{\ell}{2}, j \pm b)$ where l and b were the streamwise and cross-stream distances between the vortices respectively. The geometry of the vortex street meant that the cross-stream circuit length had a far more critical effect on the circulation than the streamwise length. For the data in this study, when the circulation values were compared with the integrated strengths, this circuit with its large cross-stream component, gave variations of $> 10\%$.

The circulation of a vortex was then calculated using the following circuits. If for a given velocity plot $b \approx \ell$, the co-ordinates for the integration circuit were $(i \pm \frac{\ell}{2}, j \pm \frac{b}{2})$ whereas if the cross-stream distance between the vortices was far less than the wavelength $(b \ll \ell)$, then the co-ordinates were $(i \pm \frac{\ell}{2}, j \pm \frac{\ell}{2})$. Tests showed that the use of these circuits gave values of circulation which matched those of the integrated vortex strength to within $5 - 10\%$.

The above boundaries were used for the calculation of the circulations of vortices of Chapter 4. However, once the bluff body was rotated as in Chapter 5, the use of a square or rectangular circuit became difficult to implement due to the increased complexity of the wake. Another boundary was used for these vortices. In this method, the vortex integration program was run on the vorticity files to produce a picture of the points summed. Hence co-ordinates of the closest circuit around the area described by these points were found and used for the velocity summation on the velocity file. Results showed that the circulation/vortex strength comparisons, including those for a non-rotating body, were much improved and matched to within 5%.

3.3.3 Choice of Integrated Strength or Circulation

Although the inherent error of a circulation calculation is lower than that of an integrated strength, calculation of the former quantity is more complex. As

discussed above, the boundary which gave the best comparison with the integrated strength involved performing the K calculation routine to acquire the summation picture, manually finding the co-ordinates of the closest circuit and then executing another summation program. Thus this method itself relied upon the boundary selection criteria for K and was very time-consuming. Therefore, in balance, the use of the integrated vortex strength was chosen to be the method usually employed for quantifying the vortices. In summary, the integrated vortex strength is

- **simple** - easy to implement and less time-consuming
- **versatile** - complex structures can be easily accommodated

3.3.4 Divergence

The divergence of a velocity field from the two-dimensional continuity equation is another useful quantity to investigate. Since the divergence is ideally zero , experimentally determined values give an indication of the errors in the downstream and cross-stream velocities. The divergence can also be used to give a comparison between the accuracy of the generated vorticity field with those produced by other techniques. For a velocity grid as detailed in Section 3.2.2, the divergence, $\zeta_{i,j}$, at a point (i,j) is given by

$$\zeta_{i,j} = \frac{(u_{i+1,j} - u_{i-1,j})}{2\Delta x} + \frac{(v_{i,j+1} - v_{i,j-1})}{2\Delta y} \tag{3.6}$$

Since divergence is calculated in a similar way to vorticity, their typical errors should be the same order of magnitude. Thus if the divergence is normalised with respect to the vorticity, an estimate of the measuring technique's accuracy should be given (Green & Gerrard [38]) . Nguyen Duc & Sommeria [71] used half the difference between the minimum and maximum vorticity as their normalisation factor and found that 95% of grid points had a normalised divergence of less than 0.1. When using this normalisation factor, Green & Gerrard [38] found that 80% of their grid points, derived using the Particle Stream Method (PSM), had this divergence.

Calculation & Use

The divergences of a set of random velocity files were calculated using a program similar to that used to compute the vorticity field. A separate program then normalised the values with respect to $\frac{1}{2}(\omega_{max} - \omega_{min})$ and partitioned the data into

pre-specified ranges. A vorticity value of zero was used as the minimum for all vortices and the maximum for each vortex was the value previously found when calculating its vortex strength. The results found were that 75% of the files had 95% of their grid points with a normalised divergence of less than or equal to 0.1. All files had greater than 80% of their grid points with this value. These results compare very well with those cited above and so this technique compares favourably with the Particle Stream Method of both Nguyen Duc & Sommeria and Green & Gerrard.

The divergence of the velocity could be used as a filter for choosing the velocity and hence the vorticity field. This is because it would not be desirable to have vorticity values included in the vortex strength summation whose corresponding velocity vectors diverged significantly from zero. Although this test was not performed for the majority of fields, a subset of the samples used above was examined for correlations between divergence and vorticity. It was found that those velocity fields which had $< 90\%$ of their grid points with a normalised divergence of 0.1 typically exhibited non-uniform vorticity behaviour and so the corresponding strengths would not have been included in the averages.

3.4 Error Analysis

3.4.1 Sources of Experimental Error

The sources of error introduced into the experiments are categorised below.

- *Systematic*
  - Two-Dimensional Flow
  - Blockage
  - PIV
- *Random*
  - PIV
  - Carriage Velocity
  - Angular Velocity
  - Temperature

Two-Dimensional Flow

The assumption central to this study was that the vortices were shed parallel to the body. Section 2.3.4 described the steps taken within the experimental procedure to ensure this condition. However, the top end condition of a clean water surface would seem to be compromised by the essential PIV requirement of seeding the flow. A series of flow visualisations were performed at low and high Reynolds numbers and with non-rotating and rotating cylinders to examine the effects of surface seeding on the shedding.

The visualisations were filmed using a CCD camera linked to a video recorder and monitor. The camera was fixed to a tripod and placed in front of the towing tank so that it recorded the flow in the x - z plane. The tripod was fifty diameters downstream of the initial start position. One side of each of the bodies was painted lengthways with blue EDICOL food dye. The experimental procedure was otherwise the same as that for the PIV experiments discussed in Section 2.3. The visualisations showed that for $Re = 120$ and 150 the vortices for all bodies vertically penetrated the surface and were parallel to the cylinder over its length.

Blockage

The blockage ratio of the facility was 0.032. Dennis *et al* [17] studied the effects of this ratio on the steady flow from a normal flat plate. They found that the flow was dependent on this ratio but for their lowest value of 0.05, the effect did not appear to be significant. Gerrard [28] noted that using a cylinder with blockage ratio 0.033 may have led to an increased distance being necessary for shedding to start at higher Reynolds numbers (≈ 100).

PIV

The systematic and random errors associated with the PIV process have been discussed previously in Section 2.4.4.

Carriage Velocity

An error in the translation velocity of the carriage could affect both the Reynolds number and the spin parameter. A stopwatch was used to time the trolley over the distance of a metre. The error associated with this measurement was typically less than 0.5% over the range of Reynolds numbers covered.

Angular Velocity

The angular velocity of a rotating body was found to be stable over the time of an experimental run. Hence this contributed an error of less than 1% to the variation of the spin parameter.

Temperature

The kinematic viscosity of the water was dependent on the temperature and so any errors in the temperature would give rise to an error in the Reynolds number. As mentioned in Section 2.3.5, the water temperature was considered as being constant over the time of the run. The reading error on the thermometer was $\pm$ 0.1°. This corresponded to an error of less than 1% over the Reynolds number range of 80 to 180.

3.4.2 Error in Vorticity & Vortex Strength Calculations

The quantity of vortex strength was used extensively in the present study. Hence it was extremely important to estimate its associated experimental error. Calculations of this error took place in the following stages.

1. % error in **velocity**
2. **absolute** error in **vorticity**
3. % error in **K**

Estimates of the percentage error associated with the derivation of velocity values from PIV analysis have been discussed in Section 2.4.4. These values were then used in steps (2) and (3).

Absolute Error in Vorticity

Calculating the error associated with a vorticity value takes several stages due to the nature of equation 3.1. Computer programs were written to generate and analyse the required data. A set of example experimental frames were studied to calculate general estimates for the absolute error in the following experiments.

- **flat plate** : no rotation
- **flat plate** : rotation
- **circular cylinder** : no rotation

The variation of vorticity error with Reynolds number for the flat plate and cylinder experiments is shown in Figure 3.3. It can be seen that the absolute error increases effectively linearly with Reynolds number for both the cylinder and the plate. The variation of the vorticity error with spin parameter was also examined for those experiments in which the flat plate was rotated. The results of this analysis showed that the rotating plate error behaviour was the same as that for the non-rotating case. The curves in Figure 3.3 were used in further calculations of the error in the integrated vortex strength.

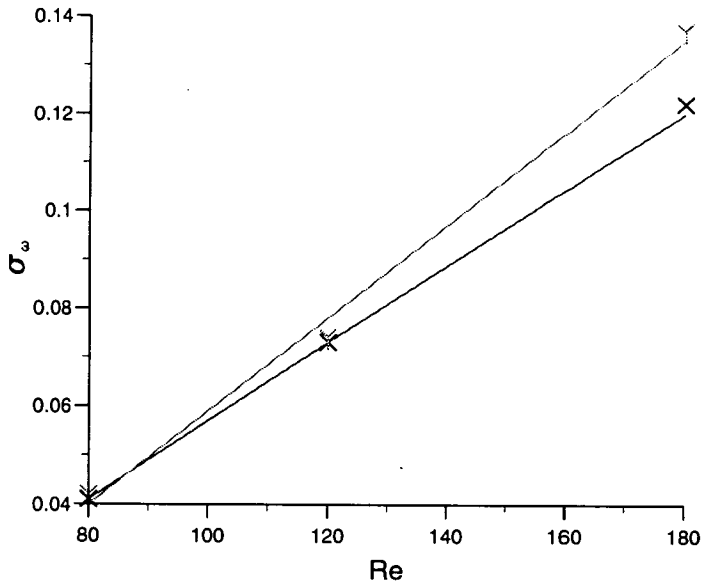

Figure 3.3: Calibration Curves for Variation of Vorticity Error with Reynolds Number: X, plate; Y, cylinder

Error in Integrated Vortex Strength

The error in the integrated vortex strength can be written as

$$\left(\frac{\sigma_K}{K}\right)^2 = \left(\frac{\sigma_{\omega'}}{\omega'}\right)^2 + \left(\frac{\sigma_a}{a}\right)^2 \tag{3.7}$$

where

$$\omega' = \sum_{i=1}^{n} \omega_i \tag{3.8}$$

Thus if the absolute error of the vorticity is known together with the magnification error and number of points used in the summation, the error in the value K

can be easily calculated. The magnification error has already been used in the estimation of the error in a velocity measurement (Section 2.4.4). This procedure can also be extended for the normalised vortex strength, $K/\pi Ud$, where U is the carriage velocity and d the body diameter.

A summary of the results of an analysis of data files is shown in Table 3.1. The errors in vortex strength when the plate is rotated are the same as when it is simply translated. If the strength is normalised then the percentage error is increased by less than 1%.

Re	σ_K(Plate)	σ_K(Cylinder)
80	4%	6%
180	9%	9%

Table 3.1: Errors in Integrated Vortex Strength

3.4.3 Error in Circulation

The error calculation for this quantity is simpler than that for the integrated vortex strength and is given by

$$\left(\frac{\Gamma}{\Gamma}\right)^2 = \left(\frac{\sigma_{V'}}{V'}\right)^2 + \left(\frac{\sigma_\ell}{\ell}\right)^2 \tag{3.9}$$

where

$$V' = \sum_{i=1}^{n} V_i \tag{3.10}$$

The percentage error of the velocities is already known from Section 2.4.4, so this is a straightforward calculation. For the range of Reynolds numbers considered here, the variation of the circulation is typically 2 - 3 %, depending on the Reynolds number of the flow.

Chapter 4

Vortex Shedding from Bodies in Uniform Flow

4.1 Introduction

4.1.1 Background

The work discussed in this chapter was to have been a precursor to the work described in Chapter 5 in which the wake behind a rotating flat plate was investigated. To act as a comparison with the rotating case, a preliminary study of the flow from a non-rotating flat plate placed normal to the free-stream in the nominally two-dimensional laminar shedding regime was investigated. In contrast to a circular cylinder, there is a considerably smaller catalogue of literature for this body particularly in this flow regime and so it was hoped that a quantitative examination would, in addition, provide some new information.

Of particular interest was the variation of the vortex strength (refer to Chapter 3) with Reynolds number. This interest stemmed from a study by Green & Gerrard [37] in which they found a discontinuity in the normalised vortex strength at a Reynolds number of approximately 100, for the flow behind a circular cylinder. Green & Gerrard used a Fizeau interferometer to measure the water surface deformation caused by vortices in the wake of a circular cylinder. A crucial part of this study was the assumption that the vortices could be described by a theoretical model known as the Oseen vortex model (refer to Section 4.4). The strengths of the vortices were found by fitting a theoretical surface profile, from the Oseen model to experimental data. Green & Gerrard found that the strength increased linearly with Reynolds number from 80 to 102, and then decreased as the Reynolds number was further increased. Hence the question asked was would there be the same discontinuity for a flat plate which has fixed separation points.

PIV measures the velocity flow field and so, unlike the method of Green & Gerrard, the vortex strength could be directly calculated from the experimental results. The results of the present study did not suggest that there was a discontinuity in the normalised strength of vortices shed from a flat plate. The experiments were then repeated for a few Reynolds numbers using a circular cylinder. These were designed to act as a check to compare the results with those of Green & Gerrard and hence confirm the technique used here. However, as with the flat plate, no discontinuity could be found. Thus the preliminary study was extended to consider the wakes behind both a flat plate and a circular cylinder in more detail.

To give a background to this study, a review of some of the previous investigations into the wake behaviour of a flat plate is given below. Also, since Green & Gerrard's result suggested the existence of an intermediate wake transition, other wake transitions, both established and disputed are discussed.

The remainder of the chapter is as follows. Firstly, the results of the study of the wakes behind a flat plate and a circular cylinder are presented. Vorticity fields are shown together with qualitative and quantitative analysis of the wake and vortex structures. An analysis of these results is then made using the Oseen vortex model and the validity of using this model to describe the laminar wakes studied here is discussed. A description is finally given of a short study of the transitional flow regime between two and three dimensional shedding.

4.1.2 Flat Plate: Previous Work

Whilst the laminar wake of the circular cylinder is perhaps one of the most well-studied of the shedding regimes, there is relatively little experimental work concerned with the same regime for a normal flat plate. The majority of work, both numerical and experimental, has been concerned with either the steady (non-shedding) or turbulent regimes. Examples of investigations of the former regime have been given in Section1.2.1 whereas those of the latter include Fage & Johansen [20], Perry & Steiner [76] and Kiya & Matsumura [51] all of which were experimental. Lisoski [57] performed both towing tank experiments and two-dimensional numerical calculations to study the nominally 2D flow at $Re > 1000$ whilst Chein & Chung [11], although not explicitly specifying a Reynolds number range, were concerned with turbulent flow in their discrete vortex simulation.

A study at a Reynolds number of 120, which is within the region of interest here, was performed by Taneda & Honji [97]. However, they were concerned only with the initial, start-up flow. Yoshida & Nomura [114] attempted to replicate numerically the results of [97] and extended their runtimes to include regular periodic shedding . They reported a Strouhal number ($St = fd/U_0$, for shedding frequency f, plate diameter d and freestream velocity U_0) and a streamline plot. Gerrard [28] provided frequency information for the laminar regime whilst Joshi [46] gave numerically derived Strouhal numbers for Reynolds numbers 60, 100 and 250. Tamaddon-Jahromi *et al* [94] and Najjar & Vanka [68] looked at shedding from a flat plate but both were primarily concerned with verifying their numerical code. Najjar & Vanka in addition to providing Strouhal numbers and streamlines included descriptions of vortex geometry and shape. However, the most detailed information available about the flow from a normal flat plate has been given by a Direct Numerical Simulation (DNS) study by Henderson [42].

4.1.3 Wake Transitions

Steady to Non-Steady Transition: Primary Instability

Central to any discussion of wake transitions is the instability which causes the wake bubble to break down and initiates the vortex shedding process. Over the past decade, instability analysis has been applied to bluff body wakes in order to establish a link between a local absolute instability and a global, self-excited response of the near wake, that is, vortex shedding (Triantafyllou *et al* [101], Monkewitz & Nguyen [65], Noack & Eckelmann [72]). A review of these numerical studies is given by Oertel [73].

Physically, the instability characteristic of a flow is determined by examining its impulse response. If a transient moves downstream, leaving the flow undisturbed, the flow is *convectively* unstable whereas, if the transient grows exponentially in place, eventually saturating the whole flow, then the flow is considered to be *absolutely* unstable. An important aspect of an absolutely unstable flow is that the final disturbance at a particular flow position is different from the initial one; the flow gives its own response to forcing which is independent of the nature of the external disturbance. Thus, the above studies were concerned with establishing that the von Karman vortex street was such an intrinsic response.

Transient experiments by Provansal *et al* [78] have shown that vortex shedding is indeed a limit-cycle oscillation of the near wake which results from a time-amplified global instability. They also found that the shedding frequency at Reynolds numbers slightly above critical was close to the frequency of the instability which produced the shedding. Provansal *et al* were able to describe the wake by a single Stuart-Landau non-linear model equation. Further transient experiments by Schumm *et al* [87] have found the values for further coefficients for this model.

Intermediate Transitions & Shedding Modes

Despite the extensive research into the shedding behind a circular cylinder, there was until recently much controversy concerning the existence of an intermediate wake transition and different shedding modes within the laminar regime.

In 1959, Tritton [103] reported that the relationship between the Reynolds number and Strouhal number as found by Roshko [80] was not completely correct and that there was a discontinuity in the frequency/Reynolds number relationship. The Reynolds number range of $80 < Re < 105$ was considered to be within the transitional regime. The onset of the transition was found to be at a lower Reynolds number in water-channel experiments. This discontinuity provoked much discussion. Proposed mechanisms included high/low speed shedding modes (Tritton) and shear in the free stream velocity (Gaster [26]).

There was a similar debate concerning the co-existence of parallel and oblique shedding modes at low Reynolds numbers. Although there was evidence that vortices often shed at an angle to the body there was no general consensus as to why this occurred (Berger & Wille [8]). However, it has now been shown that oblique shedding and the variation of measured Strouhal/Reynolds number relationship are related phenomena which are caused by three-dimensionalities within the flow.

There is a discontinuity in the Strouhal number relationship at $Re \approx 64$ even if external influences such as shear and cylinder vibrations are removed (Williamson [106]). Williamson [107] showed that laminar shedding is directly influenced by end conditions and it is these which determine the angle at which the vortices are shed. At Reynolds numbers above 64, the vortices form a periodic chevron pattern whilst for $Re < 64$ there are cells of different shedding frequencies across the span ([107], Eisenlohr & Eckelmann [19]). It is the transition between these

two modes which leads to the discontinuity in the $StRe$ relationship ([107, 19]). Williamson [106] proposed that if the Strouhal number were modified according to equation 4.1 then a 'Universal St - Re Curve' could be described for which there were no discontinuities.

$$S_o = S_\theta / cos\theta \tag{4.1}$$

where S_o, S_θ are the parallel and angled Strouhal numbers respectively and θ the shedding angle.

Parallel shedding is the most unstable mode and so is present at the start of shedding. Over long bodies it takes time for the end conditions to affect the whole span and so the chevron pattern may take many diameters of travel to develop.

It is possible to enforce purely two-dimensional (parallel) shedding by manipulating the end conditions. This can be performed in many ways, for example by suitably angled end plates or, as more recently shown by Miller & Williamson [61], by end suction. Although it is possible to force the vortices to shed at any angle, for example [61], there is evidence that the naturally occuring wake has only four shedding angles (Köenig *et al* [52]).

Thus, there is no intermediate transition which is manifested by a discontinuity in the Strouhal number/Reynolds number relation. Although the discontinuity does exist, it is a consequence of experimentally introduced three-dimensionalities and is not an intrinsic flow response. Examples of the latter are the primary transition, which was discussed above, and the secondary wake transition which is discussed in Section 4.5.

4.2 The Two Dimensional Flow Regime

This section considers various aspects of wake behaviour for both a flat plate and a circular cylinder.

4.2.1 Vorticity Visualisations

Flat Plate

The following figures, 4.1 - 4.5 show the instantaneous vorticity fields behind a flat plate normal to the flow for Reynolds numbers 80 to 150. The wake centreline is at $y/d = 2.7$ and, as is seen in the plots, the field of view starts at 3.4 diameters

downstream of the plate.

There is a clear progression in the appearance of the vortices as the Reynolds number is increased. At Re =80 it is clear that the vortices with maximum vorticity at $x/d \approx 6$ and ≈ 8.6, respectively, are not circularly symmetric and are more elliptical. The vortex at the smaller downstream distance has a vorticity 'tail' linking it back towards the region immediately behind the plate. The vortex which is just visible on the left hand side of the field of view is orientated very differently from the other vortices.

The vortices at $Re = 90$ are similar to those at $Re = 80$ but showing signs of becoming more circular downstream. However as the Reynolds number is increased to $Re = 100$ (Figure 4.3), the vortices' appearance has changed. Although they are still 'elliptical' in shape, the vortices are slightly more rounded, more tear-drop shaped than those at $Re = 80$ and $Re = 90$. The 'tail' structure is visible at $Re = 100$ for only the vortex centred at $x/d \approx 4.6$. The structure is not present for the vortices centred at larger downstream directions ($x/d \approx 6.6$ and ≈ 8.8. respectively). Figure 4.4 shows the vorticity field for the flow at a Reynolds number of 120. Its appearance is similar to that at $Re = 100$ with the same tear-drop shaped vortices.

When the Reynolds number is increased to 150, the appearance of the wake is different from that exhibited at lower Reynolds numbers. This is shown in Figure 4.5. Although the vortex at $x/d \approx 5.4$ is still elliptical in shape, beyond $x/d \approx 7.4$ the vortices have become slightly more circular.

Circular Cylinder

The vorticity contour maps showing the flow behind a circular cylinder are shown in Figures 4.6 to 4.10.

The appearance of the wake at $Re = 80$ can be seen in Figure 4.6. Again, as in Figure 4.1, the vortices are elliptical and there are tail regions of vorticity linking the vortices back to the immediate near wake. However, in this case, the tail of the vortex centred at $x/d \approx 6.6$ is far more extensive than that in Figure 4.1 and both the visible vortices are less upright than those shed behind the plate.

When the Reynolds number is increased to $Re = 90$ the first two vortices are

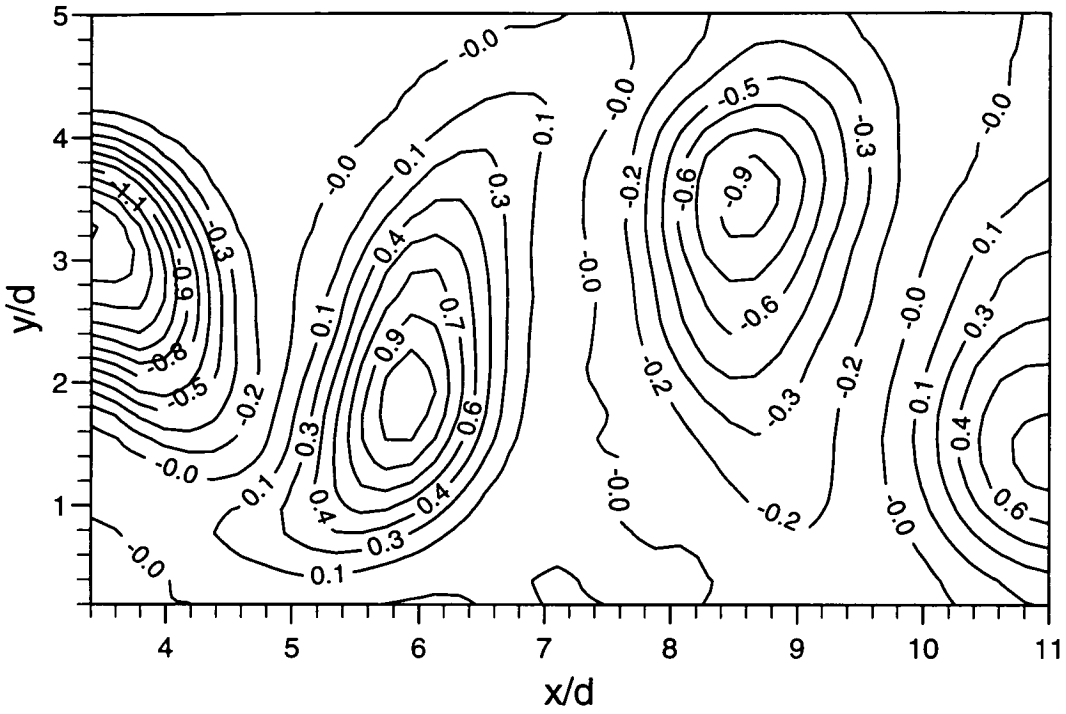

Figure 4.1: Vorticity plot (s^{-1}): Flat Plate; $Re = 80$

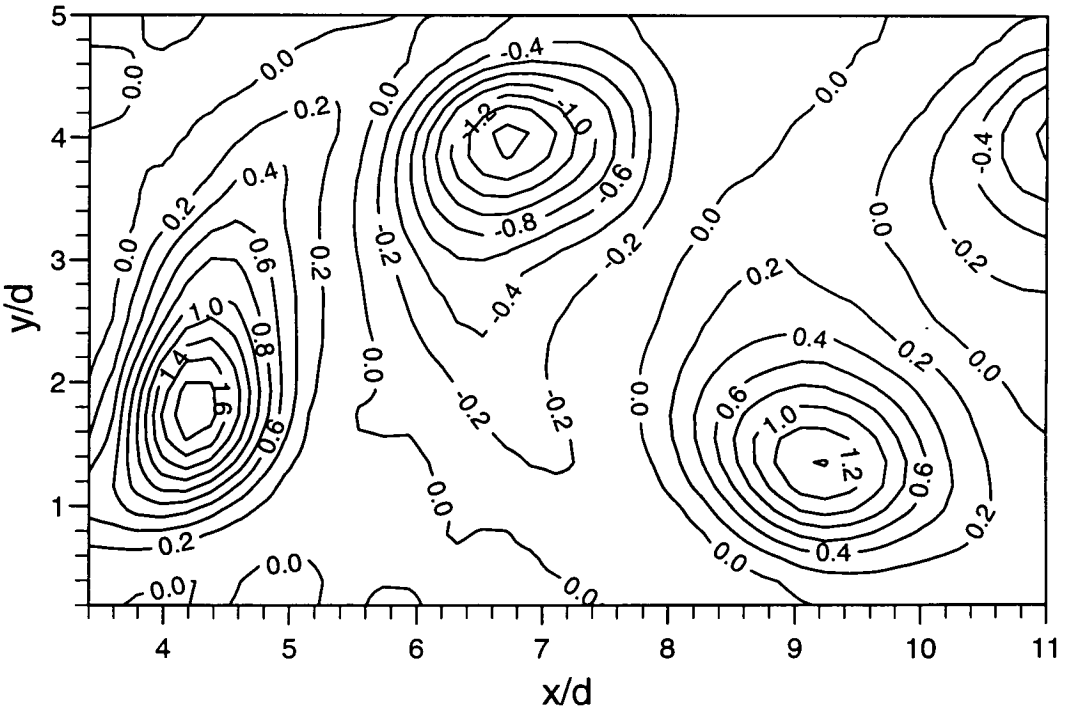

Figure 4.2: Vorticity plot (s^{-1}): Flat Plate; $Re = 90$

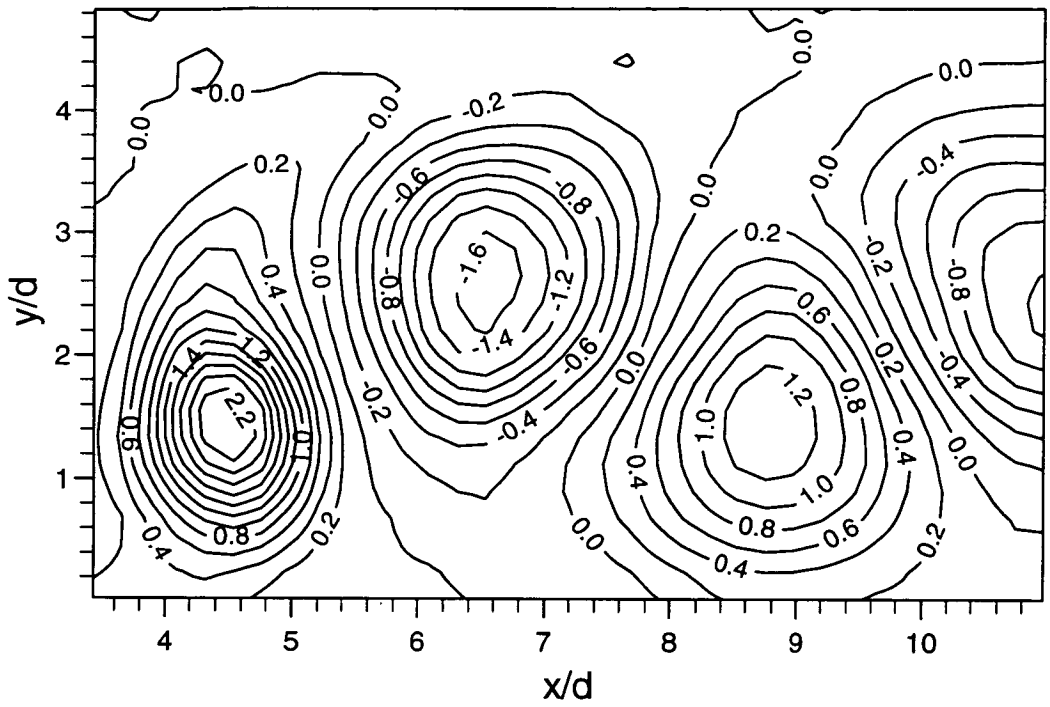

Figure 4.3: Vorticity plot (s^{-1}): Flat Plate; $Re = 100$

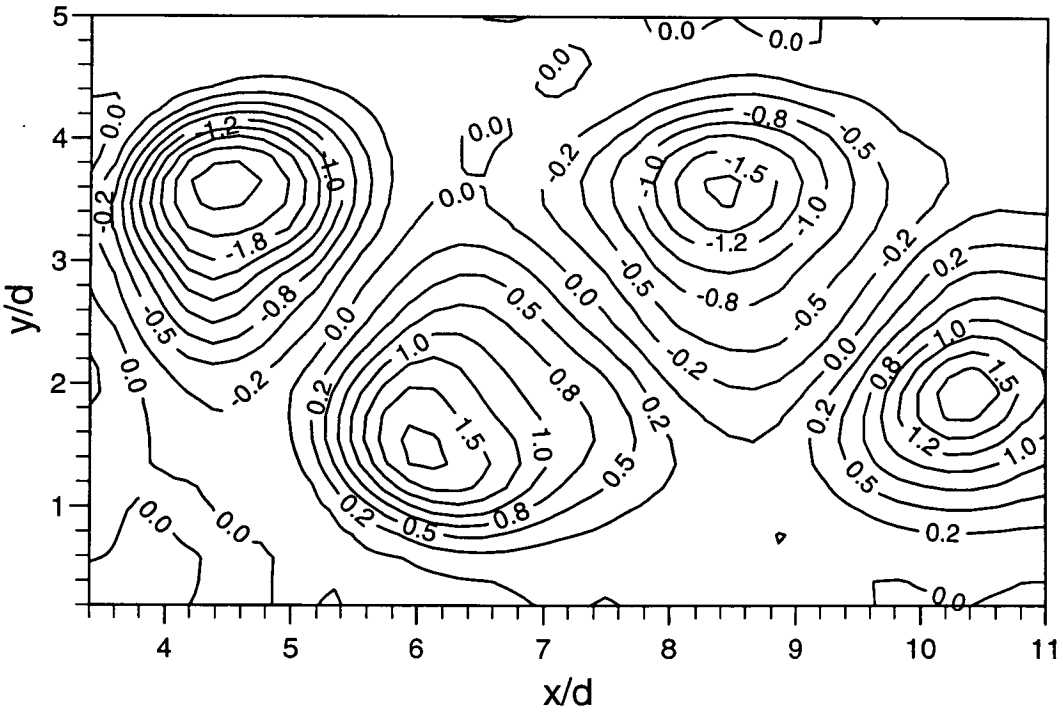

Figure 4.4: Vorticity plot (s^{-1}): Flat Plate; $Re = 120$

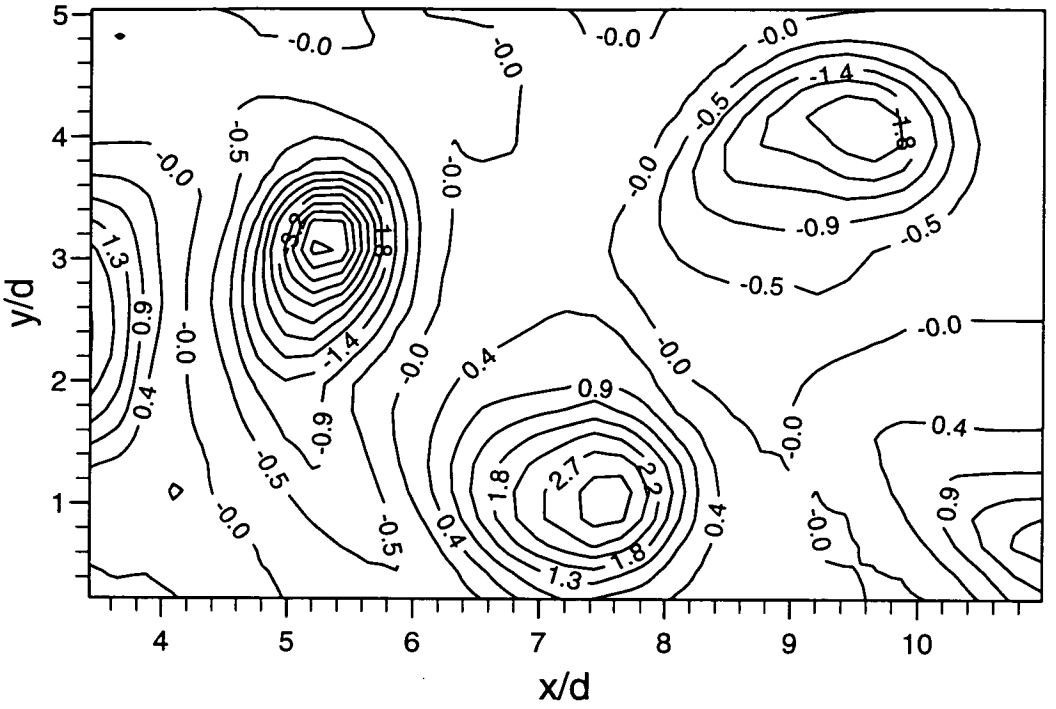

Figure 4.5: Vorticity plot (s^{-1}): Flat Plate; $Re = 150$

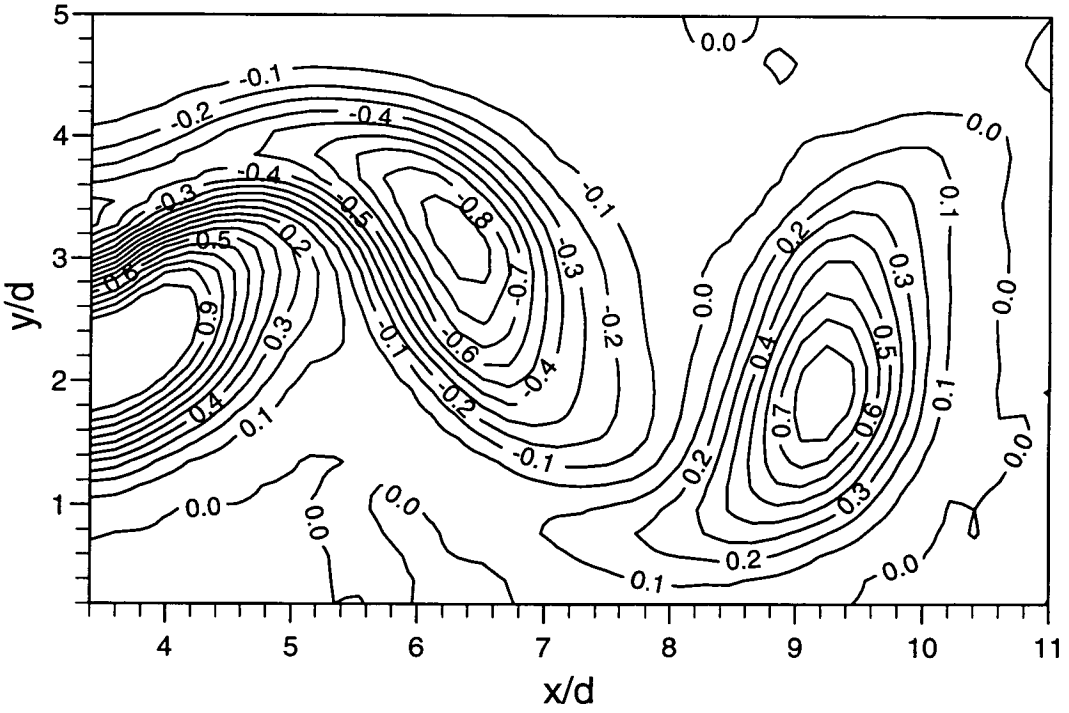

Figure 4.6: Vorticity plot (s^{-1}): Circular Cylinder; $Re = 80$

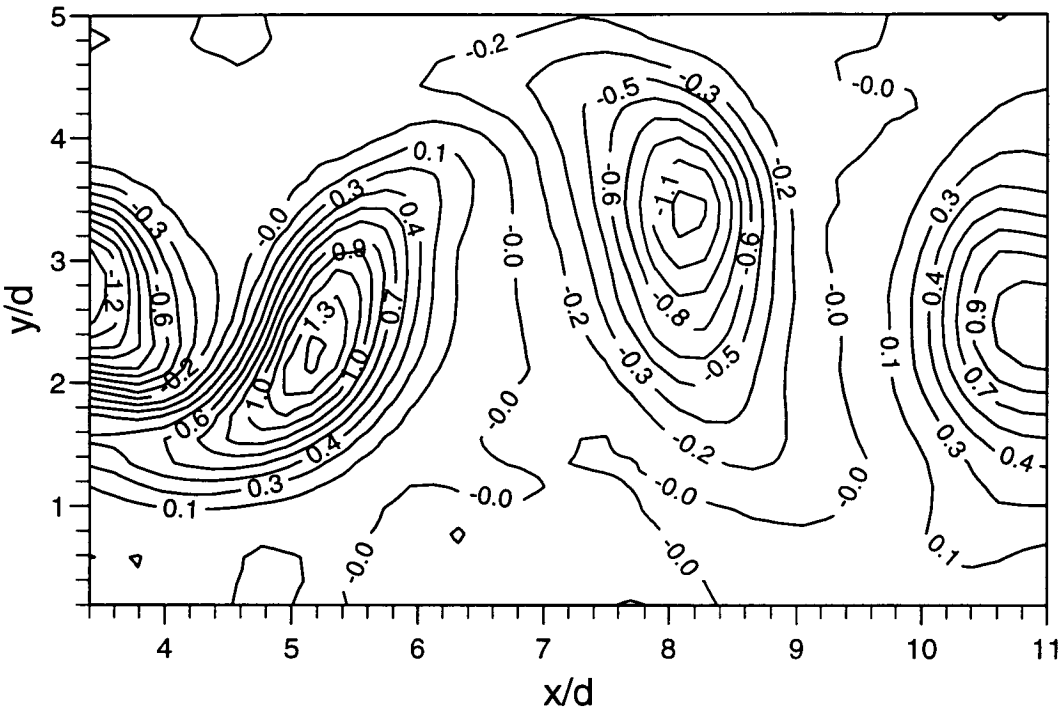

Figure 4.7: Vorticity plot (s^{-1}): Circular Cylinder; $Re = 90$

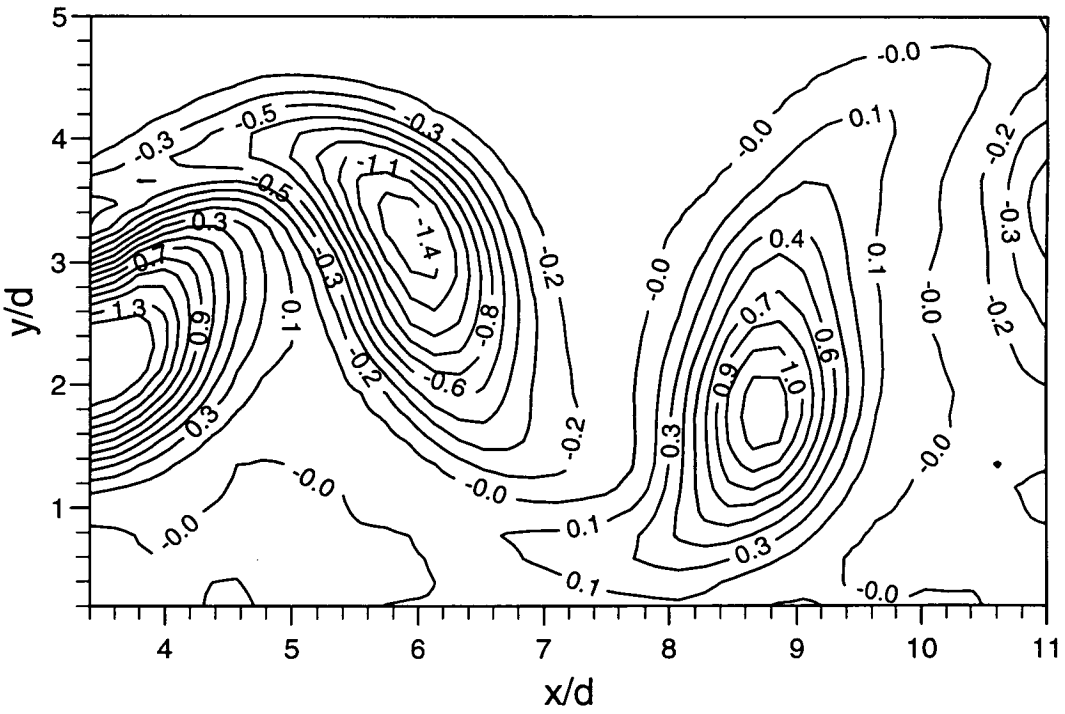

Figure 4.8: Vorticity plot (s^{-1}): Circular Cylinder; $Re = 100$

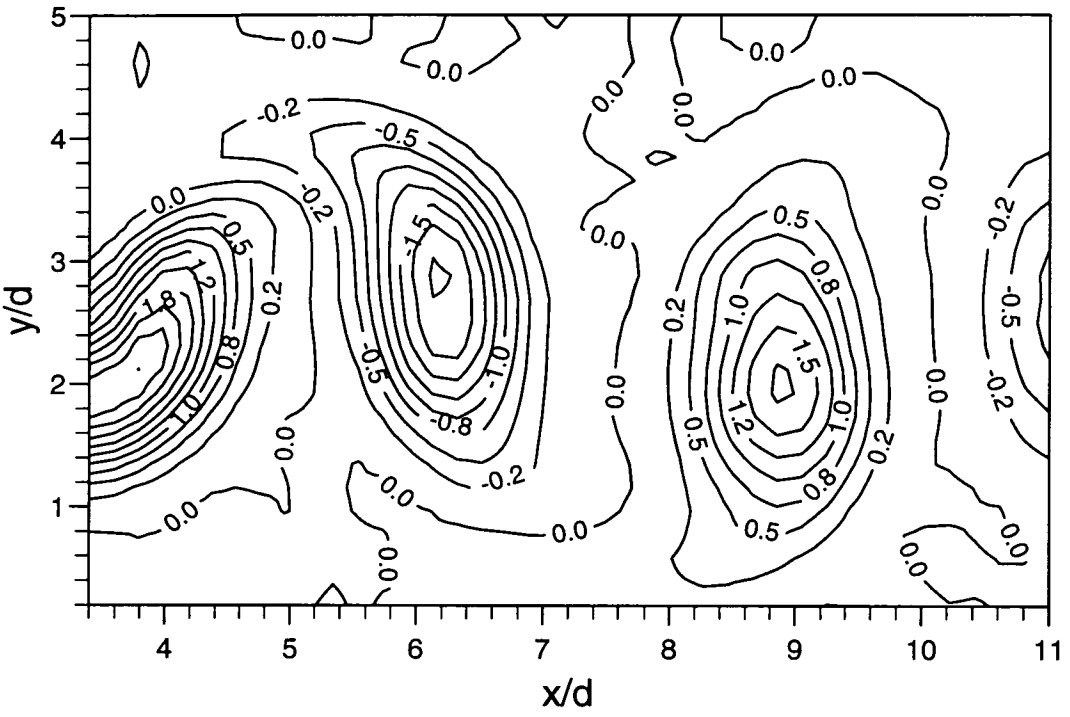

Figure 4.9: Vorticity plot (s^{-1}): Circular Cylinder; $Re = 120$

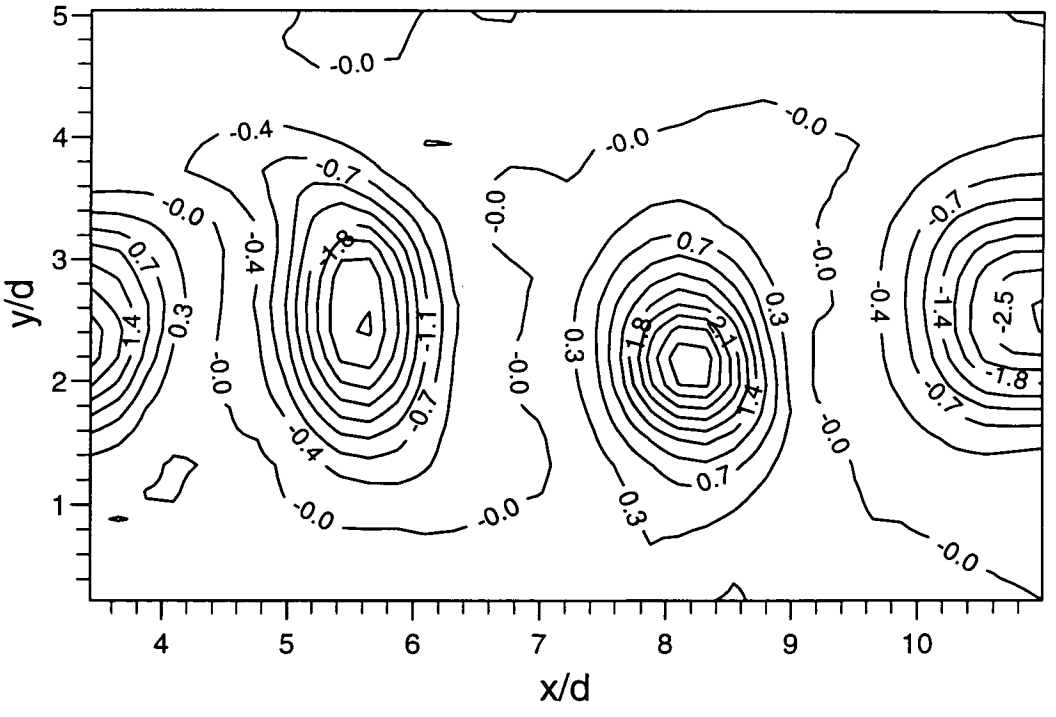

Figure 4.10: Vorticity plot (s^{-1}): Circular Cylinder; $Re = 150$

much the same as for $Re = 80$ but the third vortex, at $x/d \approx 11$, has lost its vorticity tail. Figure 4.8 shows the wake at a Reynolds number of 100 and it is again similar to those at $Re = 80$ and 90. This is in contrast to the wake behind the plate since by this Reynolds number the vortices were substantially different from those at $Re = 90$.

If the contour map at $Re = 150$, Figure 4.10, is compared with those at lower Reynolds numbers two developments in the wake are evident. Although the vortex is still elliptical in shape at $x/d \approx 5.6$, as with the wake from the flat plate, as the downsteam distance is increased, the vortices become more circular. Also, even though the region $x/d < 3.4$ is excluded from the maps, there is still sufficient detail to suggest that the formation region is decidedly shorter at $Re = 150$ than at the lower Reynolds numbers.

4.2.2 Wake Geometry

The wake geometry was calculated from the vorticity fields of all the analysed PIV pictures. The streamwise vortex spacing, a, was taken to be the distance between two vortices of the same rotational sense, whilst the transverse spacing, b, was the cross-stream distance between two vortices of opposite rotation. The distances were measured between the positions of maximum vorticity.

The following basic theory was used to calculate comparison values for the streamwise spacings. If the convection velocity of the vortices, U_v, at a Reynolds number, Re, is

$$U_v = fa \tag{4.2}$$

where f is the shedding frequency and

$$\frac{U_v}{U_0} = C_v \tag{4.3}$$

and where C_v is a constant and U_0 is the freestream velocity, then

$$\frac{a}{d} = \frac{C_v}{St} \tag{4.4}$$

where

$$St = \frac{fd}{U_o} \tag{4.5}$$

For a circular cylinder, Williamson's universal curve ([106]) can be used to calculate the Strouhal number where

$$St = \frac{-3.3265}{Re} + 0.1816 + 1.6 \times 10^4 Re \tag{4.6}$$

and C_v for a laminar flow at low x/d is 0.84 (Zhou & Antonia [117]). Hence values of a/d can be derived.

If a similar calculation is to be made for the flat plate some approximations must be made since experimentally determined values for the convection velocity are not available. For a Reynolds number of 100, Najjar & Vanka [68] found numerically $a/d = 4$ and $St = 0.166$. This corresponds to $C_v = 0.66$. If this is then used together with experimentally derived Strouhal numbers from Barnes (private communication) using the relation

$$\frac{fd^2}{\nu} = 0.2Re - 4 \tag{4.7}$$

then an indication of the streamwise spacings can be calculated. Gerrard [28] also gave values for the relationship of equation 4.7 for a normal flat plate but his plot contained discrete points. However, both sets of values compare very well with each other, for example at $Re = 60$, $St = 0.133$ from both Gerrard and equation 4.7.

Circular Cylinder

The variations of the streamwise and cross-stream distances with Reynolds number are plotted in Figure 4.11(a). It can be seen that there is only a slight variation in the streamwise spacing as the Reynolds number increases. Although there is a decrease from $Re = 80$ to 100, the remaining points could be considered to be constant to within experimental error. The cross-stream distance between vortices appears to decrease as the Reynolds number increases.

The hot-wire study of Schaefer & Eskinazi [84] found that both a/d and b/d decreased with increasing Reynolds number. Their values for a/d at $Re = 75$, 98 and 122 were approximately 5.8, 5.3 and 5 respectively whilst those of b/d at $Re = 94$ and 118 (both at $x/d = 10$) were 1.2 and 1.

The calculated values of a/d which are indicated by the straight line on Figure 4.11(a) correspond to within experimental error except at $Re = 80$. At this Reynolds number there is only one fully detached vortex visible in the frame of view (for example Figure 4.6) and so the streamwise wavelength has to be deduced from the half period distance. The orientations of forming and fully formed vortices differ, which suggests that the streamwise spacing between fully detached vortices is smaller. Hence the the value of a is possibly overestimated.

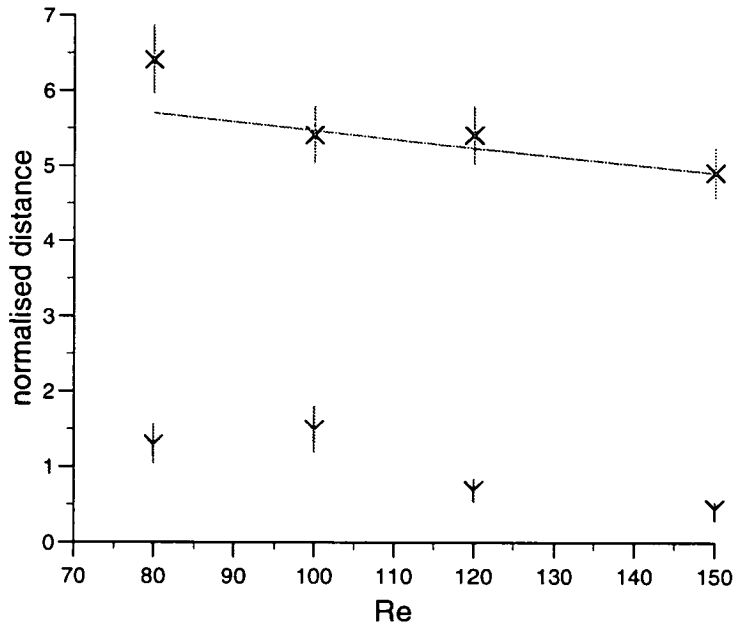

(a) Circular Cylinder

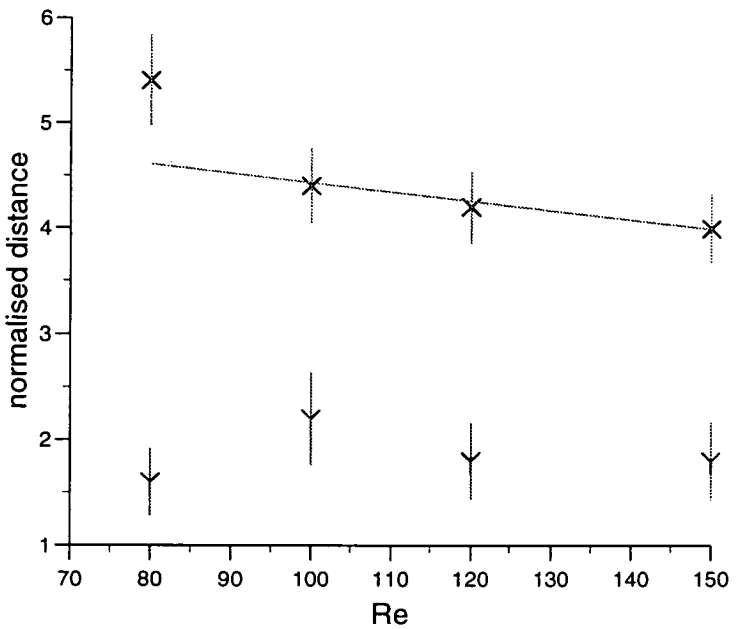

(b) Flat Plate

Figure 4.11: Wake Geometry: X, a/d ; Y, b/d ; -, numerical fit

Although the trend is for a/d to decrease as the Reynolds number increases this is not clearly happening with the experimental values. However it will be seen in Section 4.5.1 that, at higher Reynolds numbers, the values of a/d are lower than those presented here.

Flat Plate

The corresponding plots for a flat plate are shown in Figure 4.11(b). Both the streamwise and cross-stream vortex spacings show little variation with Reynolds number. The former behaviour is consistent with the circular cylinder whilst the latter is not. However, the structure of the vortices at $Re = 150$ is less consistent than at the other Reynolds numbers, there is a greater variation in their appearance, and so the errors associated with the derived quantities are larger. The value of a/d calculated by Najjar & Vanka [68] at $Re = 100$ has already been mentioned (4) whilst their value for b/d was 3. The value found in the present study is 2.2 ± 0.4.

The match between the calculated values and the experimental ones is satisfactory. Again, the discrepancy at $Re = 80$ could be due to an underestimation of the experimental streamwise spacing or the error associated with assumptions made with the theoretical values.

It is clear from the plots that the streamwise spacings of the vortices from the plate are less than those from the cylinder and the corresponding cross-stream distances are higher. An increase in the transverse vortex spacing is consistent with a decrease in the streamwise spacing since if the vortices form closer together downstream, the induced velocity field pushes them transversely further apart. This difference in wake geometries of a circular cylinder and a flat plate was noted by Henderson [42] for $Re = 250$.

4.2.3 Vortex Strength

The vortex strengths for Reynolds numbers in the range $80 \leq Re \leq 150$ were calculated using the method described in Section 3.3.1. The values presented below are the average values found from a minimum of four vortices. Most of the Reynolds numbers were covered more than once. Hence, for a given Reynolds number, vortex strength values were averaged from all analysed frames from all the experimental runs.

Although the vortex strength values were initially filtered for obvious rejections such as points being obviously missing from the vorticity summation (refer to Section 3.3.1), a further selection process was also performed. Vorticity plots have shown that a vorticity 'tail' is common at low Reynolds numbers within the field of view of the photographic frames. The vorticity within the tails generally is above the value taken as the summation boundary level (Section 3.3.1) and so is included in the vorticity summations. As the Reynolds number is increased, only those vortices closest to the body have a tail. Therefore these vortices have a larger number of points with a vorticity value which can be included in the summation. Hence the summation total for these vortices is higher than those in the rest of the field of view and the overall vortex strength within a frame is biassed. Therefore if in a particular frame there was a mixture of vortex states, one with a tail and one or more without, only those without a tail were counted in the final averaging of strength values. If it had been possible to sum the vorticity just within the tailed vortex itself and not include the tail this filtering process would not have been necessary.

Flat Plate

Figure 4.12 illustrates the normalised vortex strength relationship with Reynolds number for the flow behind a flat plate. The strength has been normalised with respect to the carriage velocity, U. It is clear that to within experimental error the normalised strength is constant across the Reynolds number range. The error bars indicate the standard deviation of the vortex strength values when averaged from multiple frames.

A least squares best fit line through these points is described by

$$\frac{K}{\pi U d} = 1.21 - 2.8 \times 10^{-4} Re \tag{4.8}$$

These results do not show a discontinuity in the vortex strength at approximately Reynolds number 100 as found by Green and Gerrard [37] for a circular cylinder.

Circular Cylinder

The vortex strength results for a circular cylinder are shown in Figure 4.13. Also included are those of Green and Gerrard (values abstracted from [37]). It can be seen that the plots are very different. The present results follow those of the flat plate and show that there is little variation of the normalised strength as the Reynolds number is increased. In contrast, Green & Gerrard's plot increases

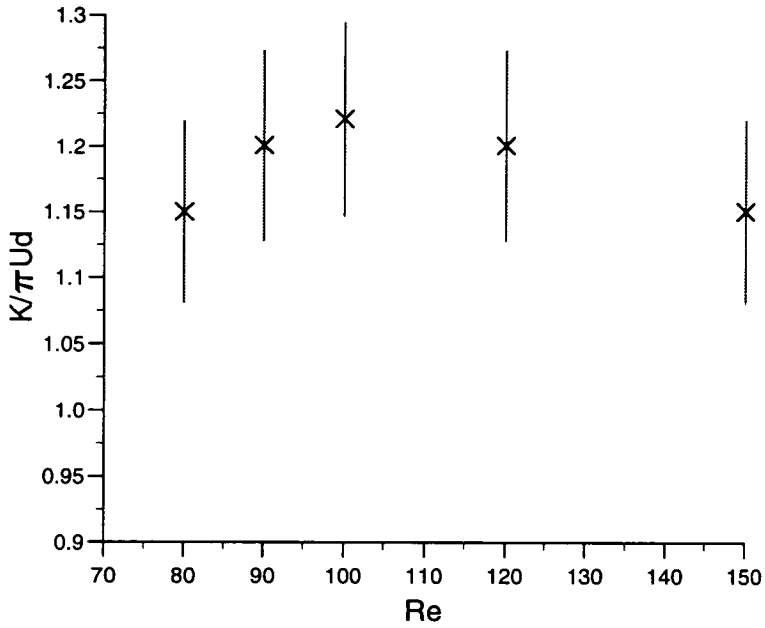

Figure 4.12: Variation of Vortex Strength with Reynolds Number for a Flat Plate

linearly by some 25% from $Re = 84$ to $Re = 102$ and then decreases immediately by 10% to $Re = 122$.

The results of the present study are plotted again in Figure 4.13(b), to enable a comparison with those of Henderson [42], the strengths have been modified. Henderson used Direct Numerical Simulation (DNS) to generate numerically the velocity and vorticity fields of the flow behind bluff bodies. He was then able to perform numerically the summation of vorticity within a vortex up to a given boundary value to calculate its strength. Henderson found that the values of the normalised vortex strength fitted a universal curve with the form of equation 4.9.

$$\frac{K}{\pi UD} = \frac{-5.38}{Re} + 0.948 + 3.1 \times 10^{-4} Re \tag{4.9}$$

All vortices within the range $5 \leq x/d \leq 15$ were included in the production of a vortex strength for a given Reynolds number. No definition of a boundary value for these strength calculations was included in Henderson [42]. However it is considered by Henderson (private communication) that a value of 5% of the maximum vorticity of the vortex was used as the boundary summation.

Due to noise levels in the present study it was impractical to use a summation boundary of less than 10% of the maximum vorticity (refer to Section 3.3.1). How-

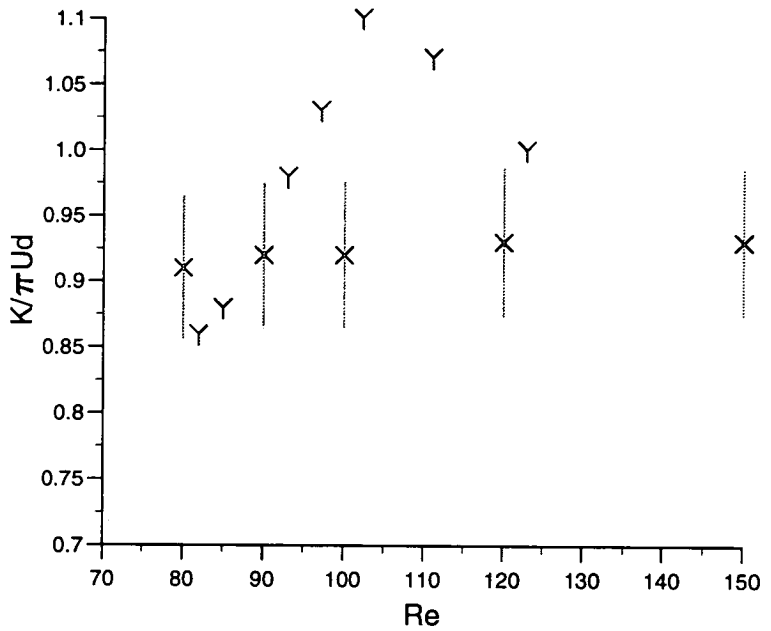

(a) X, present study; Y, Green & Gerrard (1991)

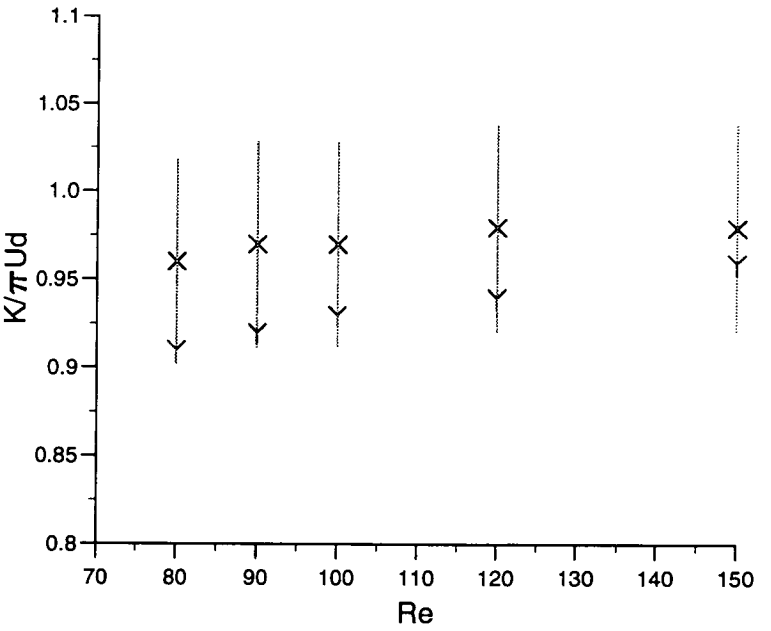

(b) X, present study (modified); Y, Henderson (1995)

Figure 4.13: Variation of Vortex Strength with Reynolds Number for a Circular Cylinder

ever, as illustrated in Figure 3.1, the variation of vortex strength with percentage of the maximum vorticity (ω_{max}) used as the boundary, is linear. Hence if the vortex strength using a summation boundary of 10% ω_{max} is known, the strength using one of 5% ω_{max} can be calculated. It is these latter values which are plotted with those of Henderson in Figure 4.13(b). It can be seen from Figure 4.13(b) that the numerical results are to within approximately 5% of those of the present study. The difference between the present results and those of Henderson is probably systematic since, due to difference in techniques, Figure 4.13(b) does not exactly compare like with like.

4.2.4 Loss of Circulation

The strength of a vortex depends on two factors: the flux of the circulation shed into the wake, and the formation process behind the body. A method of quantifying the difference between the generated circulation and the resulting vortex strength is by calculating the lost circulation. This is defined as

$$FractionalLoss = 1 - \frac{K}{\Gamma_0} \tag{4.10}$$

where K is the experimentally measured vortex strength and Γ_0 is the shed circulation from the body. At low Reynolds numbers the main mechanism for destruction of vorticity within the wake is diffusion; diffusing vorticity crosses the wake centre line and cancellation occurs.

Green & Gerrard [37] plotted the variation of lost circulation with Reynolds number and found that the percentage loss decreased from 55% at $Re = 70$ to 32% at $Re = 100$ and then remained constant. They proposed that the change in behaviour after $Re = 100$ was a result of the decreasing effect of diffusion and the increasing one of convection. This in turn was linked to a transition at approximately Reynolds number 100 which was manifested by a discontinuity in the normalised vortex strength (also refer to Green [36]). Since the present study did not find a discontinuity in the vortex strength, a change in behaviour of the lost circulation would not be expected.

Estimating Shed Circulation

The value of Γ_0 can be estimated as follows. The rate at which vorticity is shed into the wake can be approximated by (from Sarpkaya [83])

$$\frac{\partial \Gamma}{\partial t} = \frac{1}{2}(V_1^2 - V_2^2) \approx \frac{1}{2}V_1^2 \tag{4.11}$$

where V_1 and V_2 are the velocities on the outer and inner edges of the separating shear layer respectively. If V_1 is approximated by the separation velocity of the boundary layer, U_s then for a wake period of T,

$$\Gamma_0 = \frac{1}{2}U_s^2 T \tag{4.12}$$

Circular Cylinder

For a circular cylinder, the velocity at the edge of the separating shear layer is found generally from measurements of the base pressure coefficient, C_{pb} where

$$C_{pb} = \frac{(P_b - P_s)}{\frac{1}{2}\rho U_0^2} \tag{4.13}$$

P_b is the base pressure measured 180° from the front stagnation point, P_s is the static pressure, ρ the density of the fluid and U_0 the freestream velocity. From Bernoulli's theorem

$$\left(\frac{U_s}{U_0}\right)^2 = 1 - C_{pb} \tag{4.14}$$

hence, if for a given Reynolds number both C_{pb} and the Strouhal number are known, the circulation shed into the wake from the boundary layer can be found.

For the present investigation, the Strouhal numbers were calculated from Williamson's relationship [106] and the base suction coefficients from Williamson & Roshko [111]. Over the Reynolds number range of 80 to 150 the circulation lost in vortex roll up decreases from 47% to 42% (refer to Figure 4.14). The error associated with each of the data points is between approximately 4% and 7% depending on the body and the Reynolds number.

Flat Plate

Since there are no studies of the base suction coefficient behind a flat plate, it was necessary to use a value from the literature for the separation velocity. Fage & Johansen [20] and Sarpkaya [83] have both given values for U_s/U_0 but the one used here is that of Chein & Chung [11]), 1.45. This value was used for all the examined Reynolds numbers. The Strouhal numbers were calculated from equation 4.7.

The loss of circulation from the flat plate is also shown in Figure 4.14 and it can be seen that the decrease is from a 48% loss at $Re = 80$ to one of 37% at $Re = 150$.

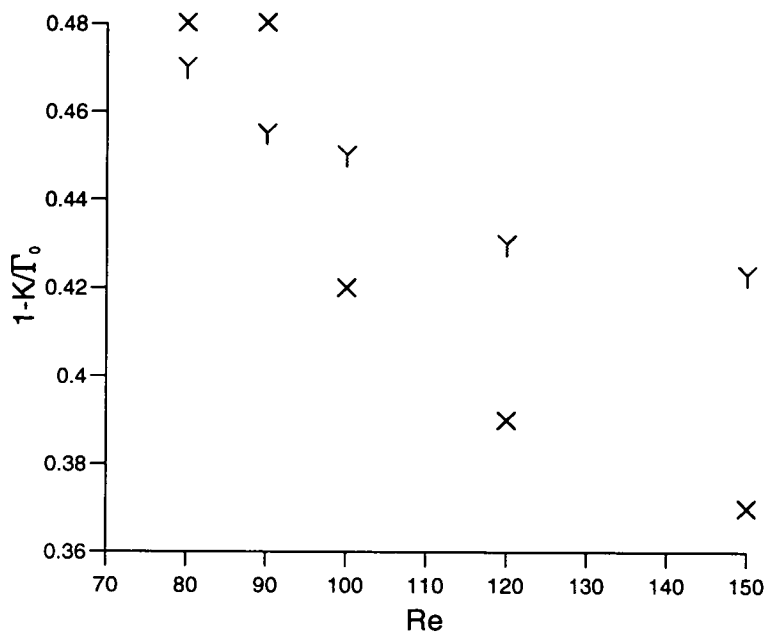

Figure 4.14: Loss of Circulation with Reynolds Number: X, plate; Y, cylinder

4.2.5 Variation of Maximum Vorticity

To highlight body shape effects and to enable comparison with the numerical results of Henderson [42], the variation of the maximum vorticity with downstream distance was considered. The results are shown in Figures 4.15(a) and 4.15(b) for the circular cylinder and flat plate respectively for $Re = 100$ and $Re = 180$. The error associated with each point is effectively the same as the error in the vorticity for the particular Reynolds number and body since the effect of the carriage velocity and body diameter errors are negligible (Section 3.4.2).

The results for the plate (Figure 4.15(b)) show that at $Re = 100$ there is a decrease in the maximum vorticity until $x/d \approx 8$ after which it remains constant. Although measurements were not possible for $x/d \leq 5$, it would appear that the maximum vorticity decreases rapidly in this region of the wake. For the circular cylinder at this Reynolds number, Figure 4.15(a), shows that, to within experimental error, the maximum strength is constant over the range of downstream distance. Overall, the values for the maximum of the vortices shed from the plate are higher than those from the cylinder until $x/d \approx 8$ and then are barely distinguishable.

The results for the circular cylinder are compared for $Re = 100$ with those of

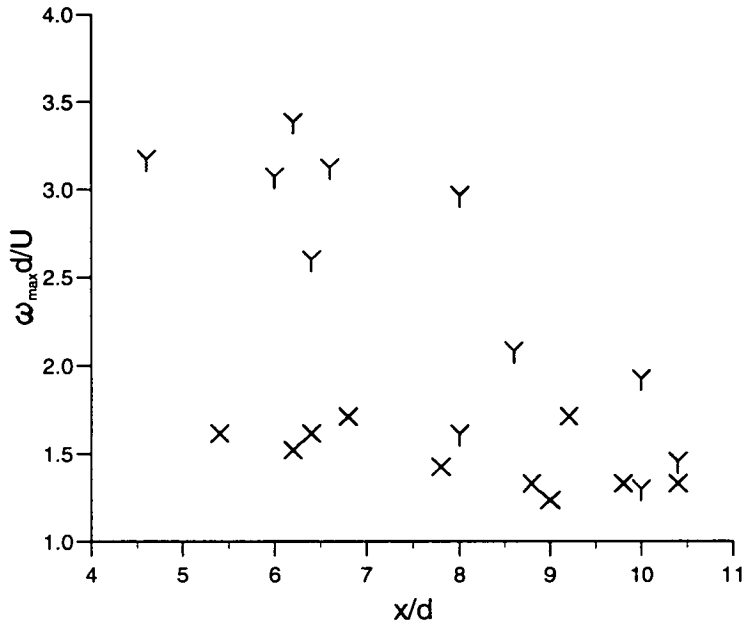

(a) Circular Cylinder

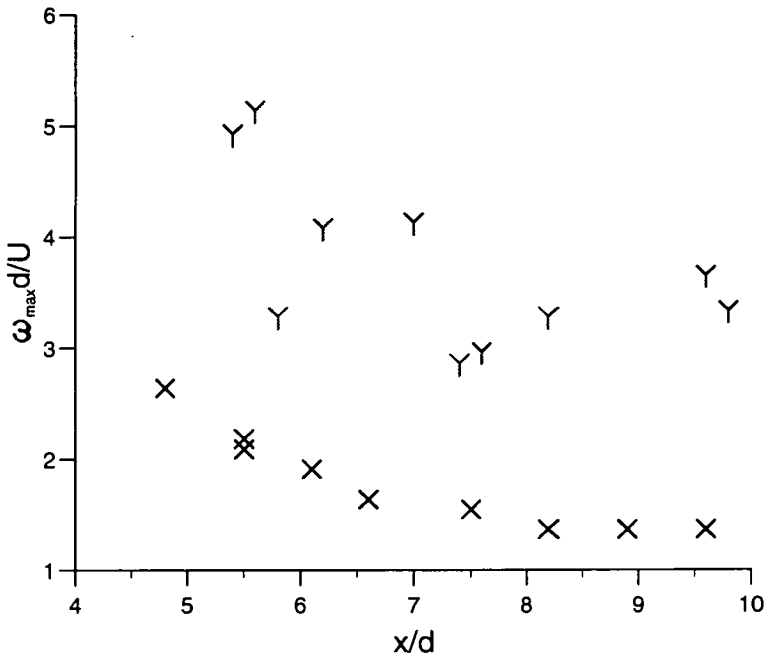

(b) Flat Plate

Figure 4.15: Variation of Maximum Vorticity with Downstream Distance: X, $Re = 100$; Y, $Re = 180$

Henderson (values abstracted from Figure 4.20 [42]) in Table 4.1. It is clear that both sets of results agree to within experimental error.

x/d	ωd/U (Corlett)	ωd/U (Henderson)
5	1.60 ± 0.06	1.57 1·85
10	1.33 ± 0.06	1.29

Table 4.1: Comparison of Numerical and Experimental Maximum Vorticity Values at $Re = 100$

Although $Re = 180$ is not strictly within the two-dimensional regime, the variation of the maximum vorticity at this Reynolds number is included here because of the contrast with the results at $Re = 100$. Despite the wider scatter of values, at $Re = 180$ both bodies show an increased rate of decrease in the maximum vorticity with downstream distance. For the flat plate, ω_{max} decreases from $\approx 5\ s^{-1}$ to $\approx 3\ s^{-1}$ for $5 \leq x/d \leq 9$ whilst, for the same range of downstream distance, the cylinder maximum vorticity decreases approximately from approximately $3.2\ s^{-1}$ to $2\ s^{-1}$. A direct comparison with Henderson is not possible with the high Reynolds number example of [42] since he used $Re = 250$. For $Re = 250$, Henderson showed (Figure 4.22) that the maximum vorticity decreased from approximately $3.5\ s^{-1}$ to $2.6\ s^{-1}$ for x/d of 5 to 10.

4.3 Discussion

4.3.1 Vorticity Plots & Shedding Mechanisms

The vorticity plots of the wake behind both the flat plate and the circular cylinder show a clear progression in appearance as the Reynolds number is increased. Primarily, the region of vorticity linking back towards the body (the 'tail') decreases in length with increasing Reynolds number and the vortices appear to be more compact at smaller downstream distances. These observations are connected to the vortex formation processes within the wake.

Two shedding mechanisms have been identified, a high Reynolds number mode and a low-Re mode. The boundary between the two mechanisms is $Re = 350$ (Griffen [39]). The high Reynolds number mechanism was proposed by Gerrard [27]. A vortex forming from a separating shear layer on one side of the body

remains stationary with respect to the body and draws the shear layer on the opposite side of the wake across the centreline. This oppositely signed vorticity is entrained into the separating shear layer. Eventually the oppositely signed vorticity cuts off the circulation supply to the vortex and it is shed.

At low Reynolds numbers, a vortex does not form whilst remaining stationary with respect to the body, but instead splits apart. The observation of vortex splitting by Freymuth *et al* [25] was incorporated by Green & Gerrard [38] into their low Reynolds number vortex formation model. In this model, there are two stages to vortex shedding; vortex formation and then vortex shedding. Circulation is lost by oppositely signed vorticity being cancelled by diffusive mixing, but otherwise the circulations on either side of the body remain constant. Close to the body there is a region of high shear stress but further downstream, outside of this region, a coherent structure of vorticity forms. This vortex eventually possesses its own entrainment properties and is able to induce cross-stream flow, eventually cutting off its circulation supply and hence being shed. As the Reynolds number is increased the strand of vorticity behind the splitting vortex becomes smaller. Green [36] found that this shedding behaviour at $Re = 73$, 92 and 150.

The vortex formation length was identified by Green & Gerrard [38] as being the distance to the position of maximum vorticity. The agreement of this definition with others which have been proposed was discussed by Griffen [39]. As the Reynolds number is increased, the formation length decreases (Green & Gerrard). For a circular cylinder, they found that the position of maximum strength occured at $x/d \approx 2.6$ at $Re = 80$ whilst at $Re = 150$ this distance had reduced to $x/d \approx 2.1$. Thus the vortices shed closer to the body as the Reynolds number increases. The decrease in the vorticity tail length agrees with these findings; the tail region persists at higher Reynolds numbers but moves closer to the body and so moves out of the camera's field of view.

4.3.2 Vortex Strengths

The vortices shed from a flat plate are stronger than those shed from a circular cylinder. This is in accord with the separation velocity from the plate being higher than that from the cylinder (refer to equation 4.12) and the shedding periods being comparable.

Over the Reynolds number range studied, the variation of the normalised vortex strength was continuous for both bodies. No discontinuity was found at $Re \approx 100$ for a circular cylinder. This is in stark contrast to the results of Green & Gerrard. The present vortex strengths are in agreement with the numerical values of Henderson [42]. Both of these studies directly calculated the vortex strengths rather than indirectly like Green & Gerrard who used a vortex model. Hence the validity of using this model, the Oseen vortex model, to describe the vortices generated here needs to be questioned. This question is addressed in the following section.

The present results are also in agreement with the trends shown by other mean quantities of the cylinder wake. Both the variations of the Strouhal number and base suction coefficient with Reynolds number are continuous (refer to Williamson [106] and Williamson & Roshko [111] respectively). Although, as discussed by Green & Gerrard and Green [36], this does not preclude the possibility of a transition being manifested in another quantity such as the vortex strength, the likelihood of such a transition is lower than if other discontinuous relationships were present.

4.3.3 Loss of Circulation

The loss of circulation between the shedding shear layer and a photographed vortex has been shown to vary continuously with Reynolds numbers between 80 and 150. As expected, this is in contrast to the results of Green & Gerrard who found the relationship with Reynolds number to change at $Re = 100$.

Figure 4.14 indicates that the rate of circulation loss with Reynolds number from the flat plate is greater than that from the circular cylinder. This suggests that the diffusive interaction between oppositely signed vortices is greater for the plate. However, the shear layer separates from a flat plate at an angle away from the wake centreline whilst that from a cylinder separates more towards the centre. This suggests that less interaction rather than more is possible in the near wake between flat plate vortices than the cylinder's. Thus possible reasons for the differing behaviour are as follows.

The method of calculating the circulation shed from the plate is different from that used for the circular cylinder. Section 4.2.4 described how a single value of U_s/U_0 was used to estimate the circulation over the Reynolds range from 80 to

150. This value, in common with the other possible choices, was taken from a study of turbulent flow. It therefore is almost certainly not appropriate for use at low, laminar Reynolds numbers. The ratio of the shedding velocity to the free-stream velocity does not remain constant over the investigated Reynolds number range and so, by implication, the use of a single, constant, ratio for the plate is perhaps flawed.

Equation 4.12 is commonly used to estimate the circulation in the shedding shear layer. However results from Henderson [42] showed that the approximation of $\partial v/\partial x << \partial u/\partial y$ across the shear layer, used in the derivation of equation 4.12, is not wholly valid. Neglecting this derivative underestimates the value of Γ_0 and hence affects the percentage of circulation lost.

4.3.4 Maximum Vorticity

The value of the maximum vorticity of a vortex shed from a flat plate is higher than that from a circular cylinder because of the increased separation velocity. Similarly, the maximum vorticity is higher at $Re = 180$ than at $Re = 100$.

Figures 4.15(a) and 4.15(b) also indicate that the rate of decrease of the maximum vorticity with downstream distance increases as the Reynolds number is increased. This increase is due to the relative vorticity gradients within the vortices. For both bodies, the vortex sizes at $Re = 100$ and 180 are comparable but the maximum vorticity at $Re = 180$ is more than 100% higher. This implies that the vorticity gradient associated with a vortex at $Re = 180$ is higher than that at $Re = 100$. Hence the vorticity diffuses more quickly at the larger Reynolds number.

The increased scatter of data points at $Re = 180$ is due to a decrease in the regularity of the vortices at higher Reynolds numbers. This will be discussed further in Section 4.5.

4.4 Oseen Modelling

Before the advent of instantaneous flow field measuring techniques, wake and vortex models were necessary if certain quantities of the flow such as the circulation associated with a diffusive vortex were to be calculated. At first, the wake vortices were assumed to have a simple potential velocity distribution but this

was later modified to allow for the effect of viscosity. This model of a potential vortex diffusing under the action of viscosity is the Oseen vortex model. Schaefer & Eskinazi [84] used the model as the basis for the development of an analytic solution for the velocity field of a viscous, laminar vortex street and to determine the geometry of the wake. Their experimental, hot wire values corroborated the analytic ones.

Bloor & Gerrard [9] initially used the model to study turbulent vortices in a cylinder wake in conjunction with hot wire anemometers. An Oseen distribution was chosen because it had been previously used by Timme [99] to match with results from experiments at a Reynolds number of 1000. Although Bloor and Gerrard found that this velocity distribution did not fit with their experimental data for radii in excess of the position of maximum velocity, the exponential form was nonetheless suitable for positions within the inner turbulent core.

In his study of lock-in behind a D-section cylinder, Davies [16] found that the vortices within a conditionally averaged turbulent wake could be modelled by an Oseen distribution with an added mean shear. This model was used by Armstrong *et al* [2] in their study of a turbulent wake behind a circular cylinder and was found to give satisfactory matches with both steady flow and perturbed flow with lock-in.

More recently, and with direct relevance to the present study, Green & Gerrard [37] used the Oseen vortex model to calculate the strengths of vortices shed from behind a circular cylinder. They found the pressure distributions assuming an Oseen vortex and then related it to a surface profile. An interactive method of fitting a theoretical to experimental profile was then used in which the strength and age of the vortex were iterated until a best fit was found. This method of calculating the normalised vortex strength gave rise to a discontinuity in the strength at a Reynolds number of 102.

As discussed in the previous section, the PIV results of the present study did not find this discontinuity in the vortex strength. This section describes the Oseen vortex modelling performed which led to questioning the model's suitability for describing the vortices within a laminar wake.

4.4.1 Theory

The Navier-Stokes equations for a two-dimensional flow in the $x\,y$ plane can be written as

$$\frac{D\omega}{Dt} = \nu\left\{\frac{\partial^2\omega}{\partial x^2} + \frac{\partial^2\omega}{\partial y^2}\right\} \tag{4.15}$$

where ω and ν are the vorticity (z component) and kinematic viscosity respectively. For an isolated, rectilinear vortex, equation 4.15 reduces to

$$\frac{\partial\omega}{\partial t} = \nu\left\{\frac{\partial^2\omega}{\partial r^2} + \frac{1}{r}\frac{\partial\omega}{\partial r}\right\} \tag{4.16}$$

where r is the radial distance from the vortex centre. Thus for an isolated, rectilinear vortex of circulation $\Gamma_0/2\pi$ the vorticity at a time t and at a distance r is given by

$$\omega = \frac{\Gamma_0}{4\pi\nu t}\, e^{\frac{-r^2}{4\nu t}} \tag{4.17}$$

which is equation 3.4 The circulation around a circuit of radius r is

$$\Gamma = \int_0^{2\pi} U_\theta r d\theta = \int_0^{2\pi}\int_0^{r} \omega r d\theta dr = \Gamma_0\left\{1 - e^{\frac{-r^2}{4\nu t}}\right\} \tag{4.18}$$

where θ is the polar angle, which is same as equation 3.3. The circumferential velocity is hence defined by equation 4.19.

$$U_\theta = \frac{\Gamma}{2\pi r} \tag{4.19}$$

If the boundary of the vorticity core is defined as the radius, R_0, at which the velocity is a maximum (Schaefer & Eskinazi [84]), then differentiation of equation 4.19 yields

$$\frac{R_0^2}{4\,\nu\,t} = 1.26 \tag{4.20}$$

Hence

$$U_\theta = \frac{\Gamma_0}{2\pi r}(1 - e^{\frac{-1.26r^2}{R_0^2}}) \tag{4.21}$$

$$\omega = \frac{1.26\,\Gamma_0}{\pi R_0^2} e^{\frac{-1.26r^2}{R_0^2}} \tag{4.22}$$

4.4.2 Initial Fitting Techniques

Since the results of Green & Gerrard [37] suggested that the wake vortices could be described by Oseen vortices, the Oseen vortex model was assumed to be valid. Hence, attempts were made to compare the experimental velocity and vorticity fields produced in the present study with those predicted using the model. The

first method of fitting experimental and theoretical profiles was to substitute experimental values of the integrated vortex strength, K, for Γ_0 in equations 4.22 and 4.21 together with estimates of the vortex core radius, R_0.

The core radii were first calculated from the velocity profiles through the vortex centre. In this case the centre was considered to be the grid position at which the vorticity was a maximum. The value of R_0 used was half the distance between the velocity maxima either side of the vortex centre. The velocity reference frame used was the one in which the carriage velocity had been subtracted. However, this was not a satisfactory method of estimating the core radius, an important parameter in the fitting process, since the there was rarely an even number of grid points between the velocity maxima. Hence the radii were later calculated using the experimental value of ω_{max}, since from equation 4.22, $\omega_{max} = 1.26\Gamma_0/\pi R_0^2$.

This technique provided profiles which adequately fitted the experimental data near the vortex centre. However as the radial distance was increased, the match between theoretical and experimental profiles deteriorated. Vorticity results of this particular fitting technique are not shown here since their appearance within the vortex core are effectively the same as those produced by the single vortex fit of Section 4.4.3. However, a theoretical x-velocity distribution (from equation 4.24) fitted to a velocity profile from a flat plate at a Reynolds number 100, is shown in Figure 4.16.

Three Vortex Fit

The Oseen vortex model is for a single, isolated vortex. Vortices within a wake are not isolated, since they are surrounded by neighbours of both opposite and same signed vorticity. The effect of the neighbouring vortices on the velocity and vorticity profiles is considered by use of a nearest neighbour scheme. The effect of the next neighbours is negligible.

For a vortex A of circulation Γ_A with nearest neighbouring vortices of circulations Γ_B and Γ_C, the total vorticity at a radial distance $\vec{r}_a$ from the centre of vortex A is

$$\omega(\vec{r}_a) = \omega_A(\vec{r}_a) + \omega_B(\vec{r}_b) + \omega_C(\vec{r}_c) \tag{4.23}$$

where $\vec{r}_b$ and $\vec{r}_c$ are the radial distances from the centres of vortices Γ_B and Γ_C respectively.

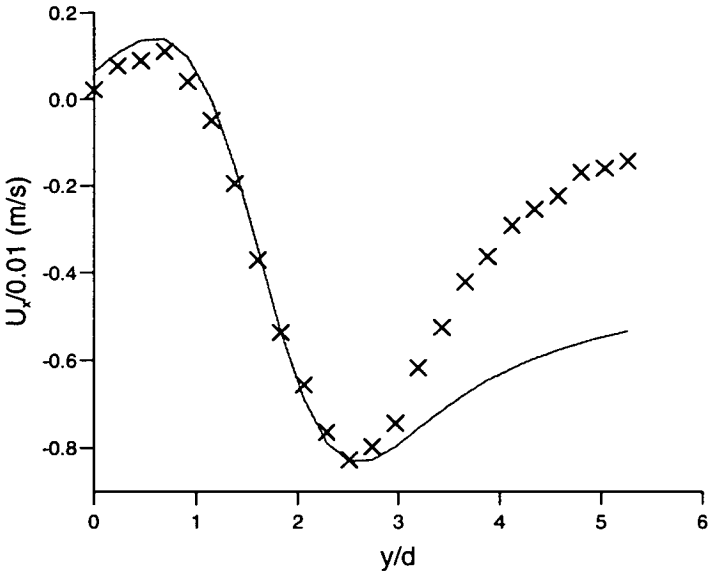

Figure 4.16: Velocity Profile through a Vortex at $Re = 100$ for a Flat Plate: X, experiment; -, Oseen profile

If this is extended to a velocity profile, equation 4.21 must be expanded to give

$$U_x = \frac{\Gamma y}{2\pi r^2}(1 - e^{\frac{-1.26r^2}{R_0^2}}) \tag{4.24}$$

$$U_y = \frac{\Gamma x}{2\pi r^2}(1 - e^{\frac{-1.26r^2}{R_0^2}}) \tag{4.25}$$

Hence, the total x and/or y velocity at a position $\vec{r}$ can be found. A schematic diagram of the relative positions of the vortices in shown in Figure 4.17. The vorticity profiles produced by this technique were not significantly different from those found by the Gaussian technique of the following section and hence are not shown here.

4.4.3 Vorticity Profiles: Gaussian Curve Fitting

A general Gaussian curve has the form

$$y = y_0 e^{\frac{-(x-x_0)^2}{2\sigma^2}} \tag{4.26}$$

If this equation is compared with equation 4.22 then it follows that

$$1.26/R_0^2 = 1/2\sigma^2 \tag{4.27}$$

and

$$\Gamma = y_0\pi(2\sigma^2) = \omega_{max}\pi(2\sigma^2) \tag{4.28}$$

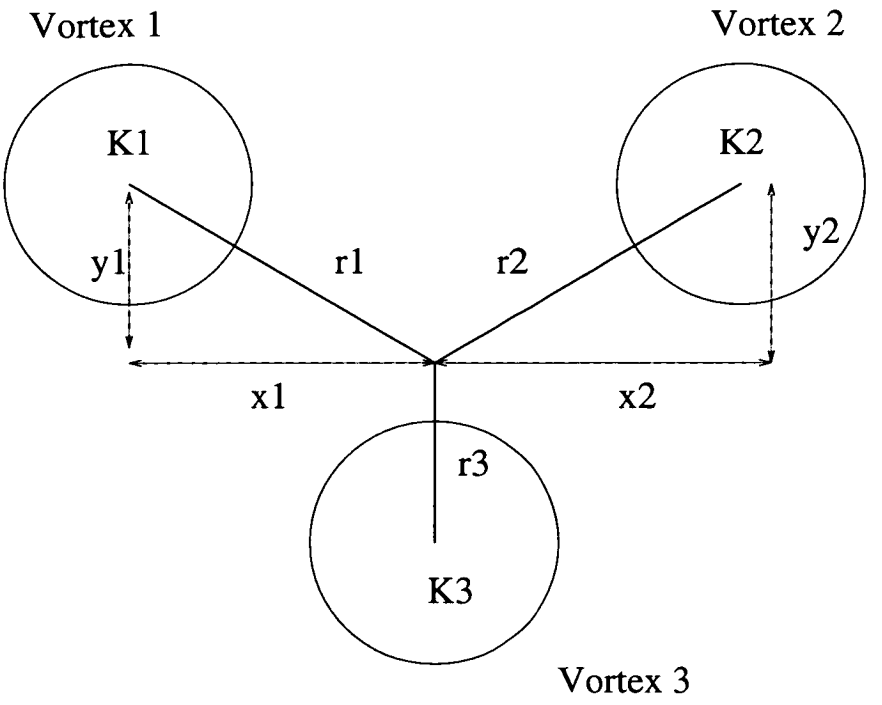

Figure 4.17: Relative Positions in Three Vortex Fit

The previous technique generated theoretical profiles by substituting experimentally determined values into the equations 4.22 and 4.21. In contrast, this method matches a Gaussian profile to an experimental theoretical profile by searching through combinations of curve parameters, σ and y_0, until a best fit is found. Significantly, the theoretical values for Γ and ω_{max} can hence be calculated and compared with those from experiment.

Single Vortex Fit

A least squares fitting program was written which found the combination of σ and y_0 values for which $[\omega_{expt} - \omega_{theoretical}]^2$ was a minimum. The corresponding theoretical profile was then plotted together with the experimental one for a visual comparison and the calculated value of Γ compared with the experimental value of K found from vorticity summation.

Profiles in both the x and y directions were taken from vorticity fields of both the flat plate and circular cylinder. Vortices at all Reynolds numbers for which data was available and from different downstream positions were used. Two examples of this fitting process are shown in Figure 4.18. The vorticity plots from which these profiles are taken are Figure 4.3 (flat plate, $Re = 100$) and Figure 4.10 (circular cylinder, $Re = 150$). The examples are from a flat plate and

a circular cylinder to show that the results are independent of the body shape. For ease of calculation the vortices were all made to have a positive circulation.

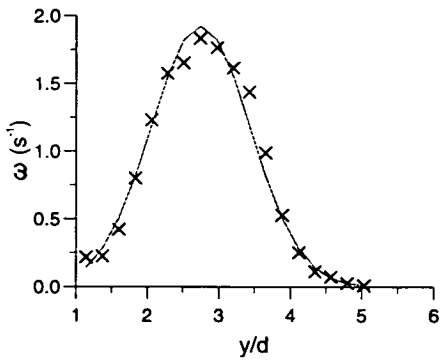

(a) Plate: $Re = 100$

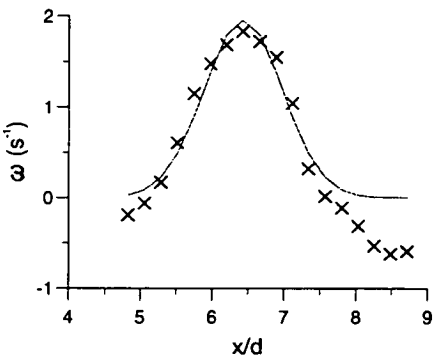

(b) Plate: $Re = 100$

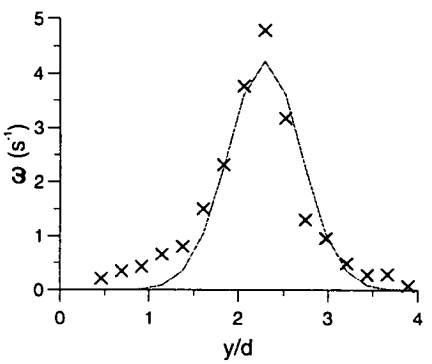

(c) Cylinder: $Re = 150$

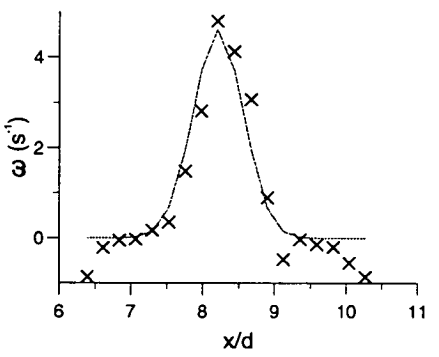

(d) Cylinder: $Re = 150$

Figure 4.18: Vorticity Profiles through Vortex Centres: X; experiment; -; single vortex fit (Gaussian)

Figures 4.18(a) to 4.18(d) illustrate that the simple Gaussian distributions fit the experimental data for the majority of the points particularly in the x/d = constant profiles. However, in Figures 4.18(b) and 4.18(d), where the profiles are in the y/d = constant direction, the experimental vorticity values change sign and become negative. This is due to the presence of adjacent vortices within the wake. Since these do not feature in this single Oseen vortex model, the single Gaussian profiles deviate from the experimental data.

The values of Γ found from the curve parameters for the above distributions are shown in Table 4.2 together with the values derived by vorticity summation.

	Body	$K/10^{-4}$ **Expt**	Profile Axis	$K/10^{-4}$ **1 Vortex Fit**	$K/10^{-4}$ **3 Vortex Fit**
$Re = 100$	*Flat Plate*	4.15	X Y	4.0 5.9	4.44 6.0
$Re = 150$	*Circular Cylinder*	4.44	X Y	3.55 4.46	3.34 4.29

Table 4.2: Strengths of Example Vortices using Oseen Vortex Model

It is clear that for both bodies, the strengths in the x direction are very different from those in the y direction. For each of the examples, one of the fits gives a value of Γ which, to within experimental error, is a good approximation of the experimental strength. However if the value of Γ taken from the profile in the other direction is considered, it is far from satisfactory. Thus the direction in which the profile is taken is evidently very important in determining the correspondence of the theoretical with experimental vortex strength.

Three Vortex Fit

This used the vorticity relation for a wake vortex of equation 4.23. The Gaussian fitting program used to find the best fit values of σ and y_0 for a single Gaussian was extended to allow a search through three sets of variables. That is, the combination of σ_i and y_{0i} for $i = 1, 2, 3$ was found for which the calculated value of $\omega_{theoretical}$ gave a minimum value for $[\omega_{expt} - \omega_{theoretical}]^2$. In this case, all three vortices were assumed to have the same values of maximum circulation (Γ_0).

Figures 4.19(a) to 4.19(d) also show the results of the best fit vorticity profiles in which the combined effects of three vortices are considered. This procedure does not greatly change the profiles in the x/d = constant plots of Figures 4.19(a) and 4.19(c), however in the plots where y/d = constant, it significantly improves the match between experiment and theory. The theoretical circulation values generated by this technique are also shown in Table 4.2. As with the single vortex fit, the values in the x and y directions are significantly different.

The y axis separation distance seems to affect which multi-fit profile leads to the closest match between theoretical and experimental vortex strength. For example, at $Re = 150$, the cross-stream distance between the vortices is very small ($b/d = 0.46$) and so the effect of the neighbouring oppositely signed vortices

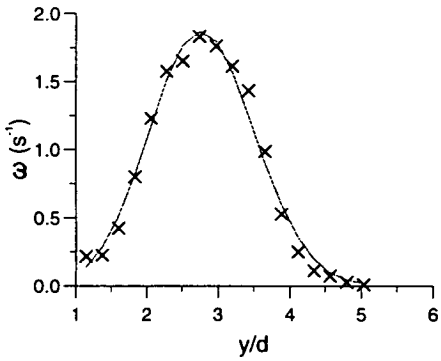

(a) Plate: $Re = 100$

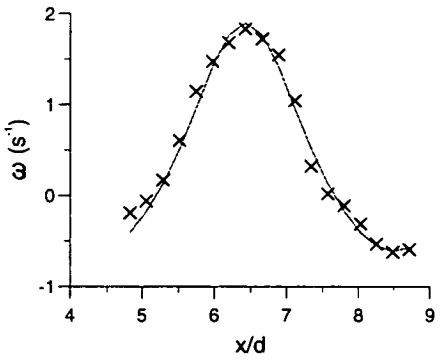

(b) Plate: $Re = 100$

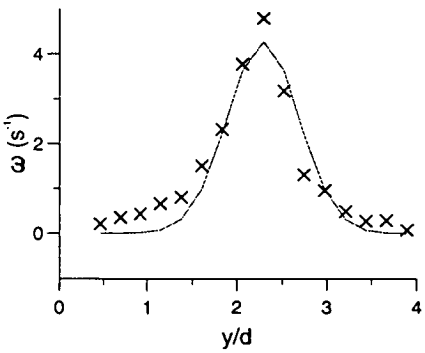

(c) Cylinder: $Re = 150$

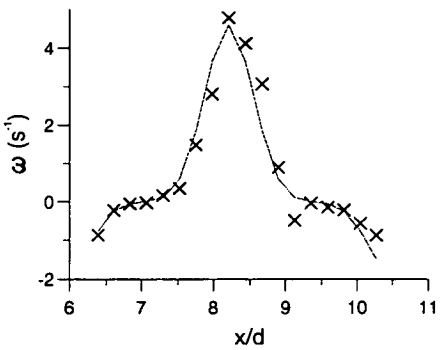

(d) Cylinder: $Re = 150$

Figure 4.19: Vorticity Profiles through Vortex Centres: X; experiment; -; three vortex fit (Gaussian)

along the x axis is far more intense than along the y axis. The resultant profile along the former axis is therefore unrepresentative. Hence the vortex strength calculated from a profile along the y axis gives a better approximation to the experimentally determined value. For the example at $Re = 100$, the cross-stream distance has increased and, as illustrated in Figure 4.19(b), the x axis profile is more representative of the whole vortex. Thus the vortex strength calculated from this fit is closer to the experimental value.

4.4.4 Discussion

The results have shown that the relationship between an Oseen vortex and a wake vortex is not straightforward. Good matches can be made between theoretical and experimental velocity and vorticity profiles within the central, core region. This confirms the result of Section 3.3.1 which found that the variation of vortex strength with the percentage of the maximum vorticity used as the summation boundary was consistent with that of an Oseen vortex. However, once the radial distance is increased beyound this core, the correspondence between a single theoretical fit and the experimental profile decreases. This decrease has been shown to be due to the influence of neighbouring, oppositely signed, vortices by fitting a theoretical profile which is a combination of three Oseen distributions. With this modified model, using both semi-empirical and Gaussian fitting procedures, there is an improvement in the match between theory and experiment. However, the x and y distributions are not the same.

This asymmetry becomes more apparent when the second, Gaussian fitting, technique is used. This is because the method generates best fit values from which the circulation of the vortex can be calculated. Even if a three vortex fit is used, the circulation values are significantly different in the x and y directions. In general, one of the profiles gives a circulation value which is close to the experimental one (to within experimental error). However it is not possible to know reliably in advance of performing the fit which profile will give this closest circulation value.

The asymmetry of the profiles is both Reynolds number and body shape independent. Although the vortices have been shown to be, in general, elliptical (refer to Section 4.2.1) and so perhaps such asymmetry would be expected, even those vortices which are more circular in shape have dissimilar x and y circulations.

Thus the results of Green & Gerrard [37] need to be discussed within the

context of these findings. Although their fitting method was different from the present study, Green & Gerrard [37] used the outer half of the x/d = constant profile through the centre of a vortex to generate a value for the vortex strength. This section was chosen because it was assumed to be the most representative of the whole vortex (Green [36]). However, as illustrated above, such an assumption is not always valid. Hence the calculated vortex strengths do not reflect the 'true' value. Therefor it is suggested that the discontinuity in the vortex strength/Reynolds number relation found by Green & Gerrard was due to a flaw in their calculation procedure rather than a manifestation of an intrinsic flow transition.

4.5 Transitional 2D-3D Regime

The second wake transition regime when the vortex shedding changes from being purely two-dimensional to three-dimensional has become of increasing interest over the past few years. Improvements in experimental techniques have enabled more accurate measurement of the flow and the introduction of direct numerical simulations have also increased understanding of this regime.

Perhaps the first study to notice three-dimensional effects in the laminar wake of a circular cylinder was that of Hama [41] in 1957. He found that when the Reynolds number was increased above 150 a transverse waviness was introduced into his flow visualisations. Grant [30] (1958) used hot-wire anemometry to study cylinder wakes in cross flow and noticed that above certain Reynolds numbers, three-dimensionalities were present in the flow in the form of counter-rotating vortices. In 1978 Gerrard [28], in his comprehensive flow visualisation study of the circular cylinder wake, found that above Reynolds numbers of approximately 140, 'fingers of dye' formed along the cylinder span. These 'fingers' and Hama's waviness can now be considered to be part of the same phenomenon, the formation of longitudinal vortices perpendicular to the primary vortices.

It was shown experimentally by Williamson [106, 108] that there are two modes of transition to three-dimensionality in which longitudinal vorticity is introduced into the wake. The modes are known as A and B and are dominant over different Reynolds numbers ranges. Mode A is initiated at Reynolds numbers approximately above 180 and consists of regular streamwise vortices with a spanwise wavelength of 3 - 4 diameters (Williams[106], Zhang *et al* [116], Brede *et*

al [10]). When the Reynolds number is increased to approximately 230, mode B appears. The streamwise vortices of this mode are less regular and have a smaller wavelength of approximately one diameter. Energy is redistributed between the modes for $230 \leq Re \leq 260$ and within this range the two modes can coexist but not simultaneously (Thompson *et al* [98]). It has been shown by Zhang *et al* that mode *A* vortices are present in both the near and far wake whereas mode *B* vortices are purely near wake phenomena.

Modes *A* and *B* are of fundamentally different natures. Mode *A* vortices result from a deformation of the primary vortices. This deformation leads to the formation of spanwise vortex loops which then stretch to form the streamwise vortex pairs (Williamson [109]). A more recent study by Brede *et al* [10] gave a description of the formation of Mode *A* in which vortex sheets in the shape of 'tongues' were pulled out of a primary vortex tube and wrapped themselves around the following tube. In contrast, Mode *B* is considered by Williamson [110] to result from an instability which scales with the thickness of the vorticity layer in the braid region between the vortices. Brede *et al* suggested that Mode *B* vortices arose from an instability of the separating shear layer. Reviews of the transition regime and its corresponding phenomena are given in Williamson [109, 110].

This section describes a short study of the wakes behind a flat plate and circular cylinder for Reynolds numbers above 150. The main aim was to investigate the effect of three-dimensionalities on the primary vortex behaviour. Flow visualisation was also performed to see if the bulk flow exhibited transitional wake structures.

4.5.1 PIV Experiments

Vorticity Plots

Flat Plate Figures 4.20 and 4.21 show vorticity plots for the wake behind the flat plate at Reynolds numbers of 180 and 230 respectively. At $Re = 180$, the vortices are circular and compact. However, at $Re = 230$ although the core is circular, regions of vorticity extend to give the vortices at $x/d \approx 6.4$ and 8.4 almost an 'S' shape.

Circular Cylinder The appearance of vortices shed from the cylinder does not change significantly as the Reynolds number is increased from 180 to 215. At both values, the vortices are compact but less circular than those from the flat

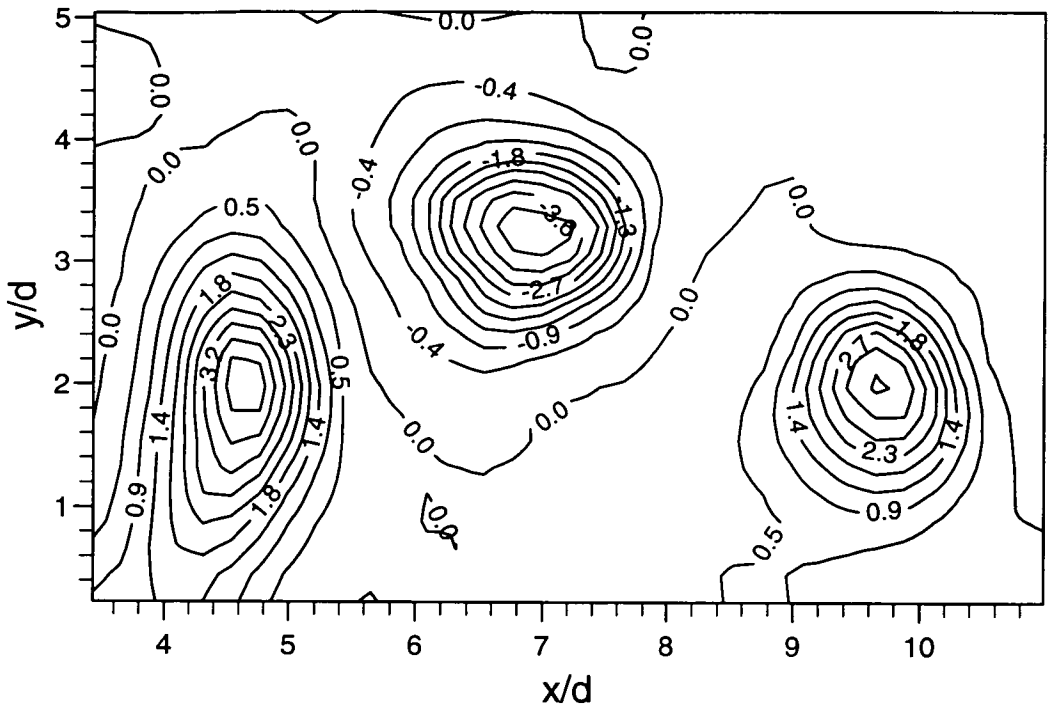

Figure 4.20: Vorticity plot (s^{-1}): Flat Plate; $Re = 180$

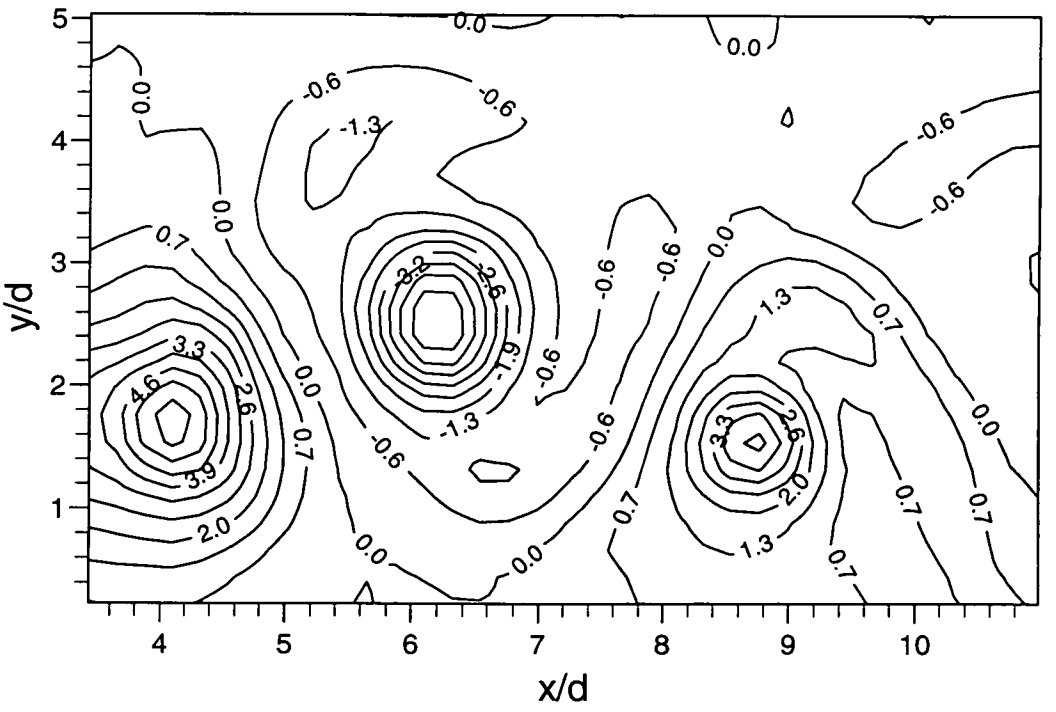

Figure 4.21: Vorticity plot (s^{-1}): Flat Plate; $Re = 230$

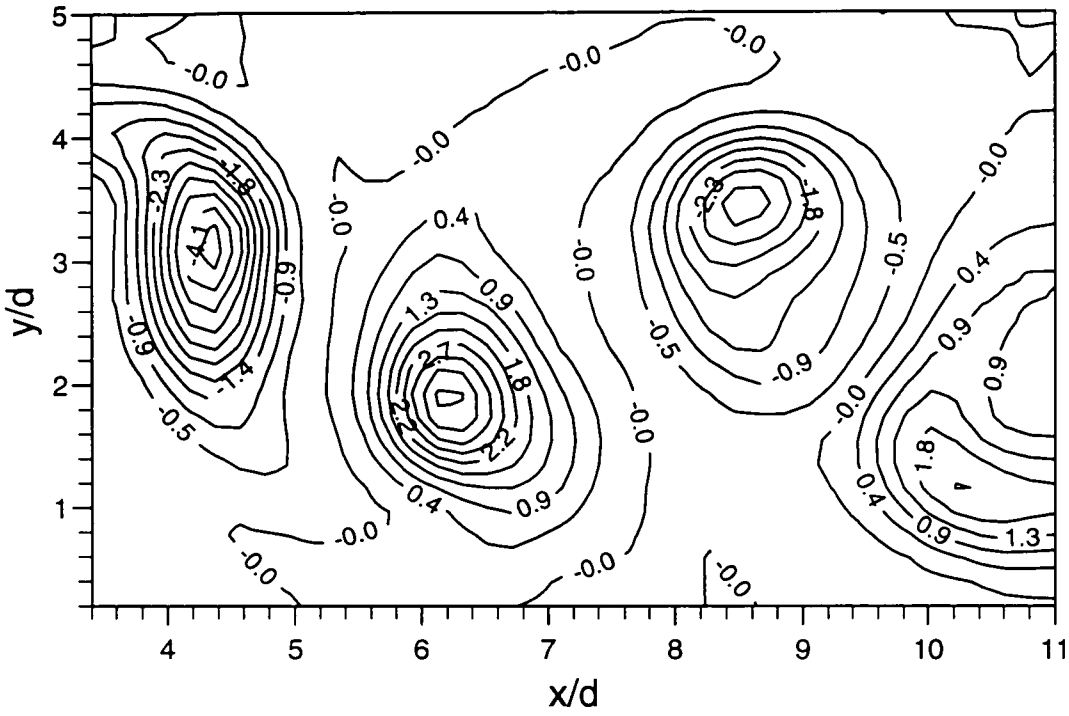

Figure 4.22: Vorticity plot (s^{-1}): Circular Cylinder; $Re = 180$

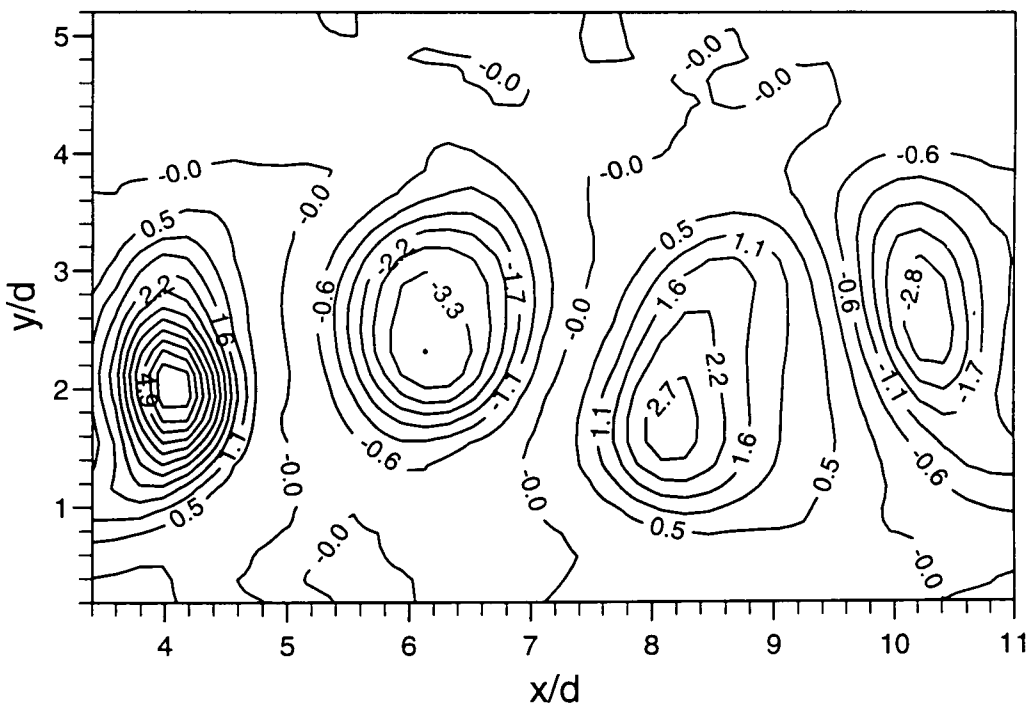

Figure 4.23: Vorticity plot (s^{-1}): Circular Cylinder; $Re = 215$

plate (refer to Figures 4.22 and 4.23). No vorticity extensions are visible for this body at the higher Reynolds number.

Wake Geometries/Vortex Strengths

The normalised vortex strengths for both the cylinder and the plate are shown in Figure 4.24.

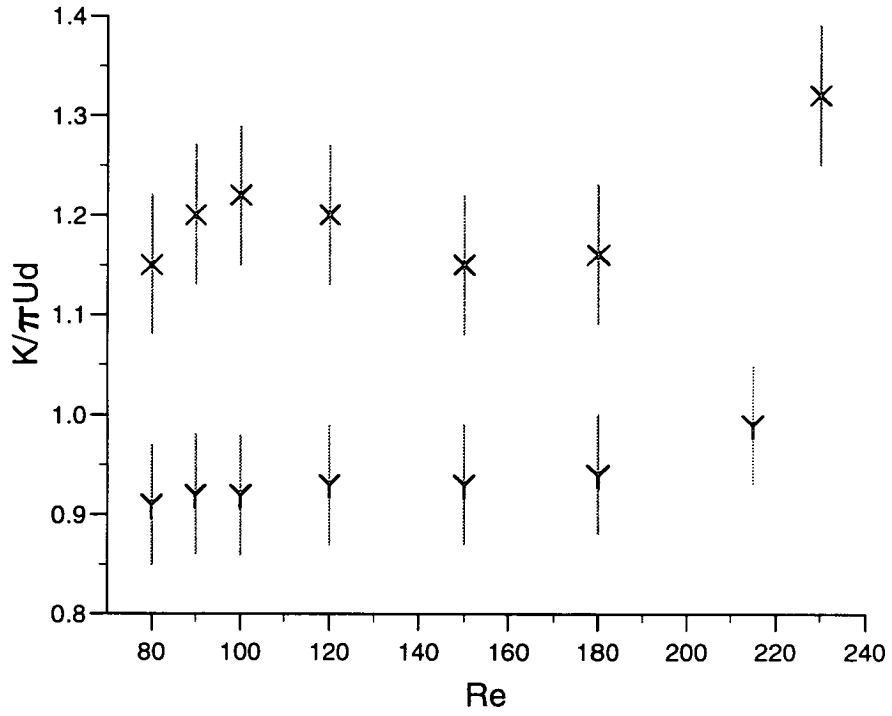

Figure 4.24: Variation of Vortex Strength with Reynolds Number: X, Flat Plate; Y, Circular Cylinder

Figures and 4.25(a) and 4.25(b) illustrate the normalised vortex spacings. These show that the cross-stream distance between the vortices does not vary significantly as the Reynolds number is increased above 150 whilst the variation of the streamwise spacings with Reynolds number is also slight. As with those at lower Reynolds numbers, all the transitional values are averages.

4.5.2 Flow Visualisation

Flow visualisation experiments were performed for both the flat plate and the circular cylinder at Reynolds numbers of 200 and 235. The purpose of these visualisations was to view the fluid in a different plane in order to investigate the presence of any three-dimensional modes within the flow. It was also of interest

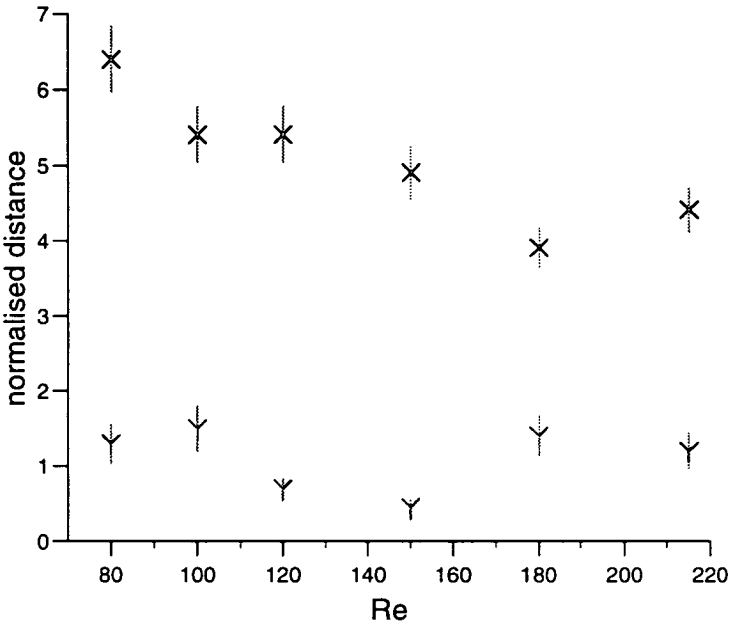

(a) Circular Cylinder

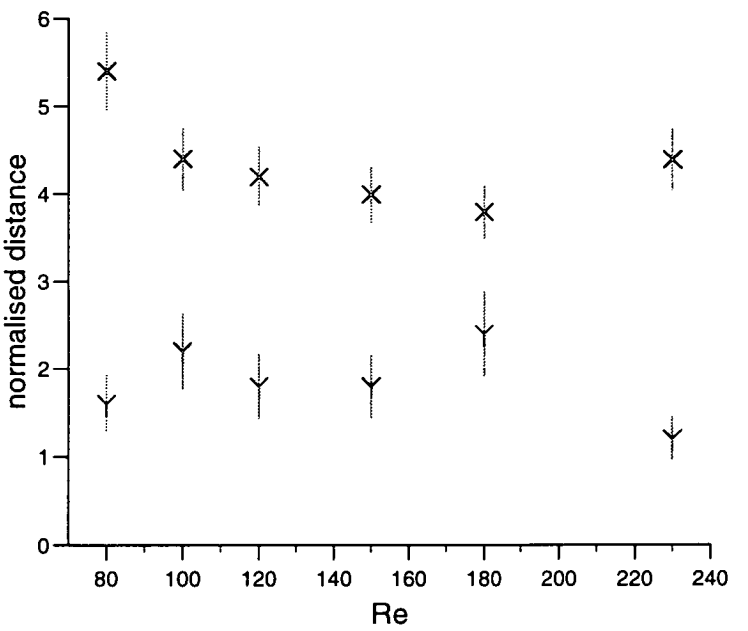

(b) Flat Plate

Figure 4.25: Wake Geometry: X, a/d ; Y, b/d

to check the top end condition (refer Section 2.3.4) as the Reynolds number was increased.

In common with previous experiments of this kind (Section 3.4.1), the bodies were painted with food dye and a CCD camera was used to capture the resulting flow pictures. The plane of the visualisation was the x-z plane, with the camera looking sideways onto the tank. Some of the resulting pictures are shown in Figures 4.27 and 4.26. The field of view of these visualisations starts approximately 60 d after the start of motion and covers a distance of approximately 40 d.

These visualisations were considered to be part of an initial study so the time between runs was reduced to approximately 45 minutes in order to facilitate increased data collection.

Circular Cylinder

At $Re = 200$, small loops are visible at regular intervals along the the vortex axes (Figure 4.26). As the Reynolds number is increased to 235, the spanwise wavelength of the loops decreases.

Flat Plate

The visualisations for the plate are less distinct than those of the cylinder. However, similar trends in the appearance of the vortex axes are visible in Figure 4.27.

Although the shedding in the above pictures is not always parallel to the body in the bulk of the fluid, the vortex axes can be seen to penetrate the surface normally. Thus two-dimensionality is enforced at the surface.

4.5.3 Discussion

Primary Vortex Behaviour

The PIV results of the surface flow primary vortices follow the trends of those in the strictly two-dimensional regime. The normalised vortex strengths of both bodies continue to show little variation with Reynolds number except at $Re = 230$ for the flat plate. The strength at this Reynolds number is significantly higher than the other values. This is because the vorticity remains higher than 10% of the maximum over a larger area than the other vortices. This increase in strength may be linked to the possible presence of Mode A structures in the fluid bulk (see

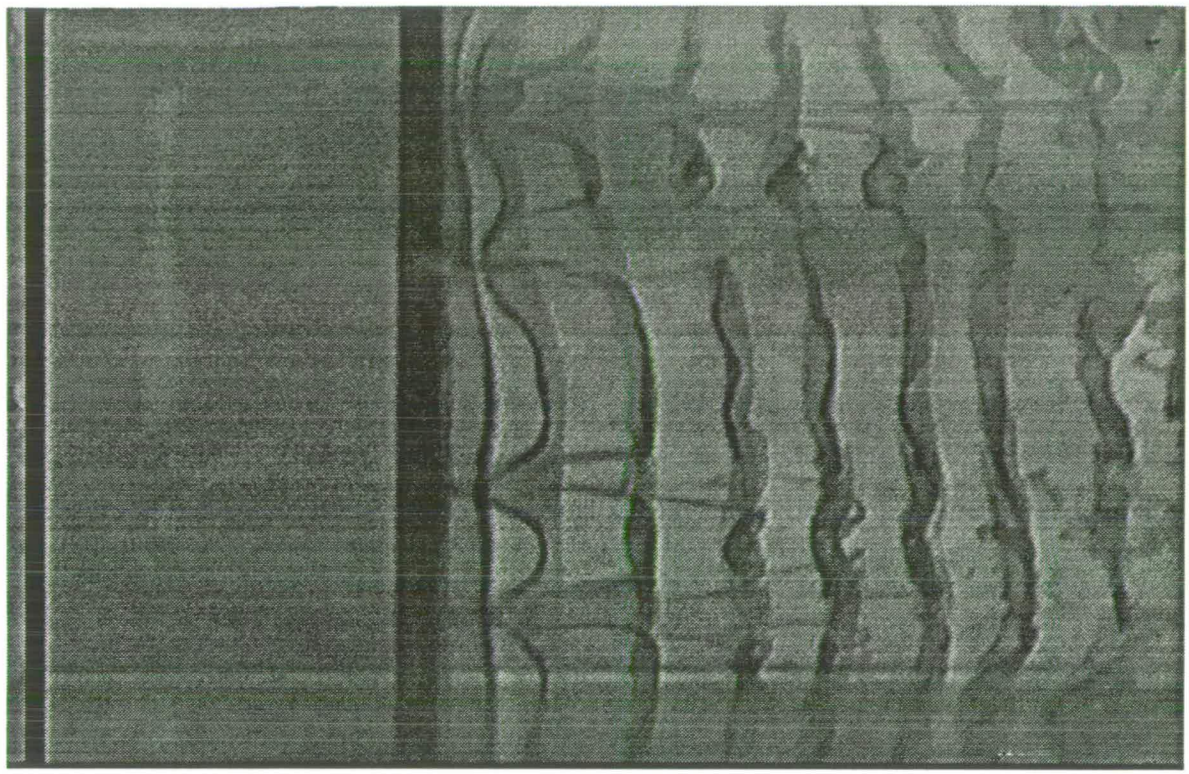

(a) $Re = 200$

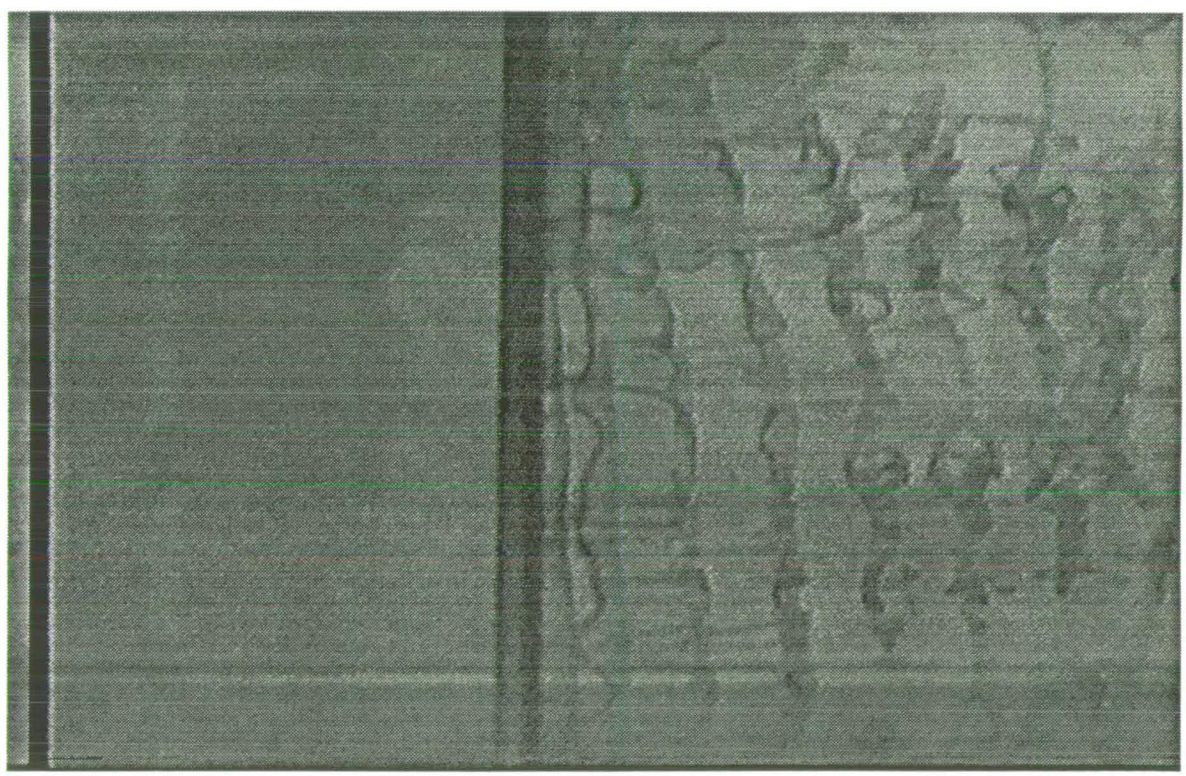

(b) $Re = 235$

Figure 4.26: Flow Visualisations of the Wake Behind a Circular Cylinder

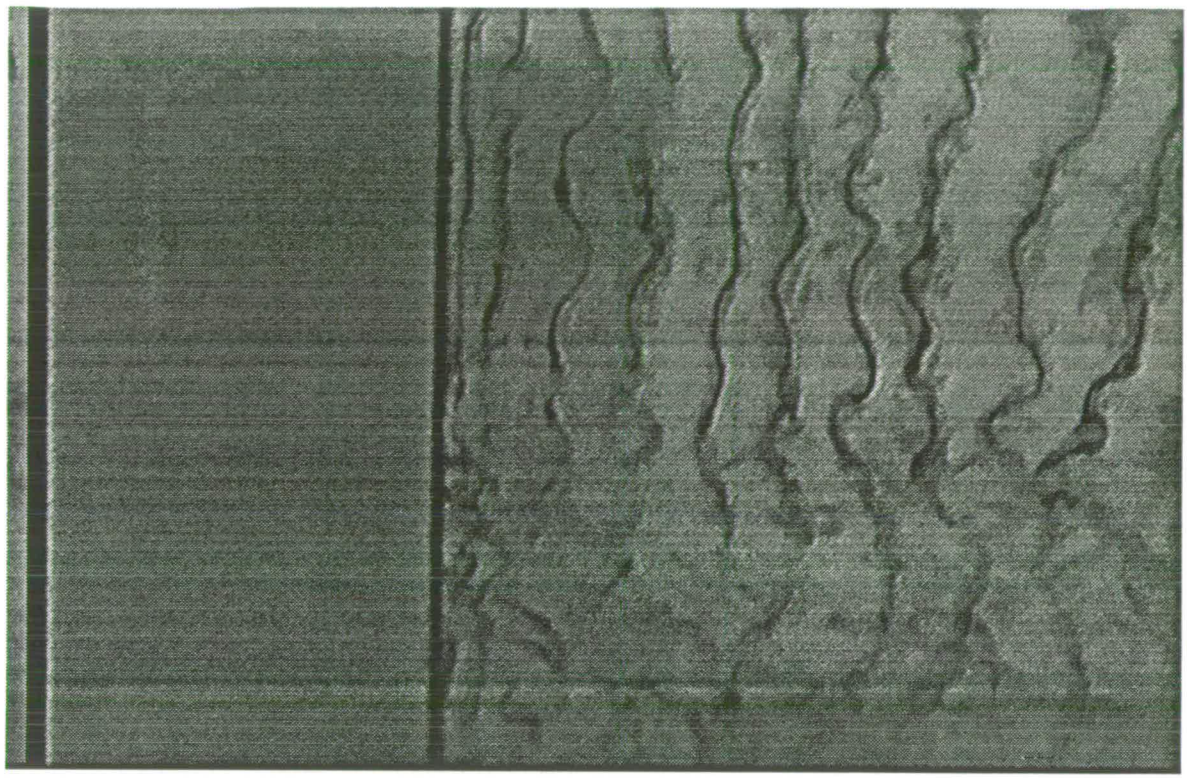

(a) $Re = 200$

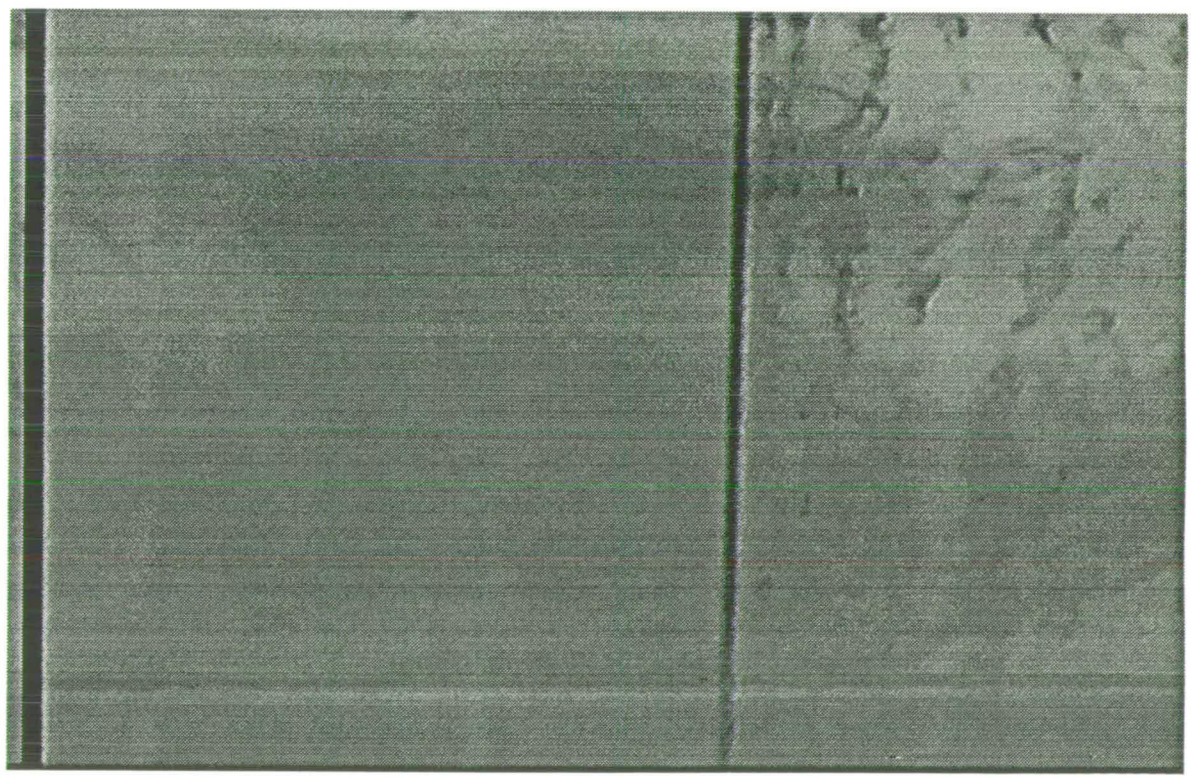

(b) $Re = 235$

Figure 4.27: Flow Visualisations of the Wake Behind a Flat Plate

below). If this is the reason then it may indicate that the strength does change when the wake becomes three-dimensional. However, this is only an initial result and more study would be required for clarification.

The variation of the wake geometry within the transitional regime is generally consistent with that at lower Reynolds numbers. A slight deviation is that with the addition of the points with $Re \geq 180$, the cross-stream distance of the cylinder appears to decrease and then increase with Reynolds number. This is probably a result of experimental variations. The vortices at these higher Reynolds are less consistent than at lower values with their shape and position being less regular from frame to frame.

Flow Visualisation

The flow visualisations suggest that three-dimensional structures are present within the bulk of the fluid. Although the correspondence between these structures and the appearance of accepted three-dimensional shedding modes is good, as described below, sources of misinterpretation of the flow visualisations need to be discussed.

Firstly, the reduced time between runs could have led to there being insufficient time for the water to settle. If there was background motion in the tank, the dye could have indicated this residual vorticity rather than genuine longitudinal vortices. Also, an inherent source of error in flow visualisations is that there is the possibility of tracer roll-up being mistaken for a vortex structure (Wu *et al* [112]).

Although the laminar regime for parallel shedding from a circular cylinder has been extended up to Reynolds number 194 and for transient experiments beyond 200 (Miller & Williamson [61]), it is highly probable nonetheless that flows of Reynolds number larger than 200 will be three-dimensional. Hence it is considered that the flow visualisations at $Re = 180$ are the most vulnerable to misinterpretation.

Transitional Structures

The loops of Figures 4.27(a) and 4.26(a) are very similar in appearance to the Mode A transition structures as described in various sources, for example Zhang *et al* [116] and Brede *et al* [10]. The spanwise wavelength of the structures does appear to be of the right order of diameters (approximately 4) and a Reynolds

number of 200 is sufficiently high for the structures to form.

Zhang *et al* and Brede *et al* have both shown that the shape of the primary von Karman vortices from a circular cylinder is modified when Mode *A* vortices are present. This modification takes the form of vorticity outgrowths which give the vortices an 'S' shape. This is the shape of the vortices shed from a flat plate at $Re = 230$. Figure 4.21 compares well with that of Brede *et al*'s Fig. 12 (for $Re = 210$).

The present study does not find such distortions of the primary vortices shed from a cylinder. However, there is evidence that Mode *A* shedding from a circular cylinder may not occur if the aspect ratio of the cylinder is low ([10], Wu *et al* [113]). Wu *et al* did not find Mode *A* vortices for a cylinder of aspect ratio 36 whilst Brede found that Mode *A* formed only for aspect ratios greater than approximately 70 (private communication). The true aspect ratio of the cylinder in the present experiments is approximately 25 but if the water surface boundary condition is considered (Green & Gerrard [37]) this value is doubled. However, this aspect ratio is still less than 70. If an insufficient aspect ratio is the reason for the absence of Mode *A* shedding for the cylinder, why the same mode should be present for a flat plate of the same aspect ratio is uncertain.

The structures shown in Figures 4.27(b) and 4.26(b) at Reynolds number 235 have the right appearance and spanwise spacing to be considered as Mode *B* vortices. The presence of this shedding mode does not appear to be sensitive to the aspect ratio of the body . In comparison with the effect of Mode *A* , Mode *B* vortices barely modify the shape of the primary vortices and so no effect would be expected on the surface, PIV vorticity plots.

Therefore, in summary, the flow visualisations indicate that three-dimensional structures, are present in the studied wakes. However, the behaviour of the primary vortices appears to be unaffected and consistent with that within the two-dimensional shedding regime.

4.6 Conclusions

This chapter was concerned with the results of a study to illustrate and quantify aspects of the laminar near wake behind a flat plate and a circular cylinder. The

primary source of information was from instantaneous velocity, and hence vorticity, fields acquired from PIV photographs.

The shape of a bluff body and hence the nature of the separation points had a profound effect on the vortex shedding. Although the same trends were generally exhibited by both the flat plate and the circular cylinder, the increased separation velocity from the former body was reflected in its wake behaviour.

The strengths of vortices shed from the cylinder and the plate were calculated using a vorticity summation method and those shed from the plate were approximately 20% higher than those from the circular cylinder. It was found that for both bodies the relationship of normalised vortex strength with Reynolds number was continuous over the range studied. This was in contrast to the interferometric study of Green & Gerrard [37] who found that for a circular cylinder there was a discontinuity at a Reynolds number of approximately 100. However, this continuous relationship is consistent with the behaviour of other mean flow properties such as the Strouhal number and base suction coefficient.

A commonly used vortex model, the Oseen vortex model, was applied to the velocity and vorticity distributions generated by these experiments. It was found that although the x and y distributions gave good fits to Oseen profiles, the two profiles were different. That is, there was an asymmetry in the distributions. This asymmetry remained even if the effect of the neighbouring vortices was considered in the fitting algorithm. Green & Gerrard assumed that a profile in a single direction would give an accurate measure of the strength of a vortex. It is proposed that it was this incorrect assumption which led to Green & Gerrard finding a discontinuity in the vortex strength at a Reynolds number of 100.

Further experiments were performed for the flat plate and circular cylinder to investigate wake behaviour at Reynolds numbers within the transitional wake regime. PIV results were consistent with those at lower Reynolds numbers whilst flow visualisations indicated the presence of three-dimensional Mode A and Mode B vortex structures within the bulk flow at $Re = 180$ and 235.

Chapter 5

Wake Behind a Rotating Flat Plate

5.1 Introduction

This chapter examines the effect on the wake of rotating the translating body. In contrast to the previous chapter only one body, the flat plate, will be considered. The plate was rotated at a range of rotation rates at Reynolds numbers of 100 and 200. The major points of interest are discussed later in this section but first an overview of previous work is given.

5.1.1 Background

The most detailed studies of the wake behind this body have been the numerical simulations of Lugt & Ohring [60] and Lugt [59]. Although both studies were strictly concerned with the flow behind rotating elliptic cylinders, the former were used only for ease of calculation. For a cylinder with a thickness to chord ratio of 0.1, any difference between the results and those for a flat plate were negligible (Lugt [59]).

Lugt & Ohring showed that two types of vortex shedding could be distinguished and were dependent on the spin parameter, S. This quantity is defined as $S = \Omega d/2U$ where U is the translation velocity, d the body diameter and Ω is the angular velocity of the body. At low values of spin parameter, $S = 0.5$ at $Re = 200$ was the example used, the vortex forming from the retreating (downstream moving) edge formed behind the plate as in the non-rotating case. However at $S = 2$ the rotation was so strong that the vortex behind the retreating edge developed on the other side of the plate. Hence the shed vortices always rotated in the opposite direction to the body rotation. This change in behaviour

will be shown to be relevant to the present study.

Lugt was concerned with the phenomenon of autorotation in which after being given an initial rotation the body continues to rotate without the aid of further impulses. He found that for $0.167 < S < 0.45$ the torque on the body was supportive. That is if the body were given an initial rotation such that $S > 0.167$, it would increase its angular velocity until $S = 0.45$. At this point the body would have zero net torque acting on it and it could continue to rotate at a constant velocity and hence be autorotative. Lugt concluded that a necessary condition for autorotation was the synchronisation of the vortex shedding frequency to that of rotation. The region overwhich lock-in occurred corresponded to $0.167 < S < 0.45$.

A study of autorotation by Barnes [6] used flow visualisation to investigate the flow behind a rotating plate at Reynolds numbers from 60 to 200. His results showed that the shedding was strongly dependent on the spin parameter of the flow. At low values of spin parameter ,approximately from $0.2 \leq S \leq 0.3$, the shedding and plate frequencies were synchronised. This regime corresponded to the simulations of Lugt. For $0.25 \leq S \leq 1.4$, Barnes found that the Strouhal number was constant and higher than that for a non-rotating plate. However, for $S > 1.4$ the Strouhal number continually decreased until $S \approx 2$. At this spin parameter the flow visualisations indicated that there were no longer coherent vortices within the wake and that vortex shedding had been suppressed.

5.1.2 Wake Control by Rotation

The question of whether vortex shedding can be suppressed by rotation is of interest within the context of wake control. As has been discussed in Section 1.3, the ability to control the vortex shedding from a body has many practical uses and is the subject of much study. Several investigations have been conducted in which the suppression of shedding from a rotating circular cylinder has been discussed.

Diaz *et al* [21, 22] examined a spinning cylinder at a Reynolds numbers of 9000. They found that the wake became increasingly asymmetrical and that the vortex shedding was suppressed when the maximum rotational velocity exceeded the translational velocity at spin parameters approximately in excess of 1.5. Coutanceau & Menard [15] and Badr & Dennis [4] studied experimentally

and numerically respectively the influence of rotation on an impulsively started circular cylinder. The former which was a flow visualisation study, found that at Reynolds number 200 for spin parameters greater than approximately 2, no vortices apart from an initial one were shed. The results of the latter study, although restricted to spin parameters of 0.5 and 1, agree with those of Coutanceau & Menard.

However, the results of a numerical study by Chen *et al* [12] also at Reynolds number 200 contradicted those of Coutanceau & Menard. Chen *et al* increased the time over which the shedding was examined and found that at $S = 3.25$, Coutanceau & Menard's highest spin parameter, an additional vortex was shed after the initial start-up vortex which had not been found by the previous study. Chen *et al* thus concluded that the vortex shedding from behind a circular cylinder could not be suppressed by rotation. They suggested that the results of Coutanceau & Menard were firstly due to the problem of resolving vortices which are being shed in a different reference frame to that of the observer and secondly due to the very short dimensionless times over which the experiments were conducted.

A more recent numerical study of the flow from a rotating and translating circular cylinder was conducted at $Re = 1000$ by Chew *et al* [13]. They found that the Karman vortex street structure deteriorated when the rotational velocity became greater than twice the translational velocity and disappeared for $S > 3$. They were able to study the flow for a longer dimensionless time than that of Badr *et al* [3] who experimentally and numerically studied the flow for $10^3 < Re < 10^4$. The latter's calculated flow reached a steady state for $S = 0.3$ whilst the experimental flow became turbulent. Thus the legitimacy of rotation being considered a method of suppressing vortex shedding, particularly at low Reynolds numbers, is still unresolved.

5.1.3 Present Study

The purpose of this study was to investigate the variation of the flow behind the rotating plate as the spin parameter was increased from the nominally synchronised region to values at which vortex shedding was seemingly suppressed. A low and high Reynolds number (100 and 200) were chosen to see if any of the rotational wake behaviour was Reynolds number dependent. Both PIV and flow

visualisation were used as complementary study techniques.

In particular, the wake behaviour with increasing rotation rates was examined for the following properties. Firstly to study the shedding frequency behaviour in the lock-in region highlighted by Lugt. If synchronisation did occur then the strengths of the pair vortices would be of interest. Secondly, to investigate the variation of Strouhal number and hence shedding frequency as the spin parameter was increased above 1.4. Thirdly, to examine the effect of the increasing rotation on the vortex strengths and the possibility of the shedding being suppressed at high values of spin parameter. PIV was particularly useful for examining this question since the derived vorticity plots could overcome the possible ambiguities of flow visualisations.

The results of this investigation are contained within two sections in this chapter. In the first section the variation of the flow properties are presented with vorticity plots and flow visualisation photographs. Then the mean wake behaviour is examined with emphasis on the variation of the mean velocity profiles with increasing spin parameter.

5.2 Variation of Shedding with Spin Parameter

This section describes the variation of the shedding patterns with spin parameter using the vorticity plots produced by PIV and flow visualisation. Both types of experiment were performed in order to optimise the overall acquired information. PIV provides instantaneous, quantitative data in this study over a restricted area whilst flow visualisation gives a dynamic but qualitative picture over a larger area.

The most extensive work was performed at a Reynolds number of 100 but a second value was also examined to see if there were any changes in the overall shedding behaviour as the Reynolds number was changed. The second value was $Re = 200$. As described in the previous chapter, when the plate is simply translated with no rotation, these two Reynolds numbers are within two different shedding regimes.

The plate was rotated anti-clockwise for all the results within this chapter and the rotation and translation were started simultaneously. The initial orientation of the plate was with the length lying parallel to the flow direction. The field of

view for the PIV photographs started at $x/d = 5.4$ and for the flow visualisations, at the plate itself. The flow visualisation field of view extended to approximately 25 d and 14 d downstream for $Re = 100$ and 200 respectively. The visualisations were performed first at $Re = 200$ with the smaller field of view. However when these visualisations were extended to include $Re = 100$ it was considered that a larger field of view would be more interesting. The position of the plate centre is at $y/d = 0$.

5.2.1 Reynolds Number: 100

Spin Parameter: 0.3

At $S = 0.3$, a vortex pair is shed with each half turn of the blade and a discernible vortex pair is formed. Photographs were taken at each plate half turn for this spin parameter. Figure 5.1 shows a vorticity plot with the pair vortices being situated at (7.2, -0.4) and (8.6, -1.4) for the negative and positive members respectively. It can be seen that the vortex side closest to the other in the pair is flatter than the other, more rounded, side. This mutual distortion arises from interactions between the pair vortices and can also be seen in the flow visualisation picture (Figure 5.2).

At this spin parameter the shedding was found to be very regular. Within the experimental run, these downstream positions of the vortices varied by $x/d = \pm$ 0.2 from frame to frame.

Spin Parameter: 0.5

It was not possible to produce satisfactory vorticity plots at $S = 0.5$ since the cross-stream field of view was insufficient. However, a flow visualisation was performed at this spin parameter and a resulting photograph is shown in Figure 5.3. The pair extend over a larger cross-stream distance than was available in the PIV frames.

Spin Parameter: 0.65

When the spin parameter is increased to 0.65, the shedding sequence changes again. In this case, the regularity of $S = 0.3$ returns, with the field of view being the same at each full turn of the plate. An example of this spin parameter is in Figure 5.4. The positions of the vortices within and between frames vary by $\pm$ 0.2 d in each direction.

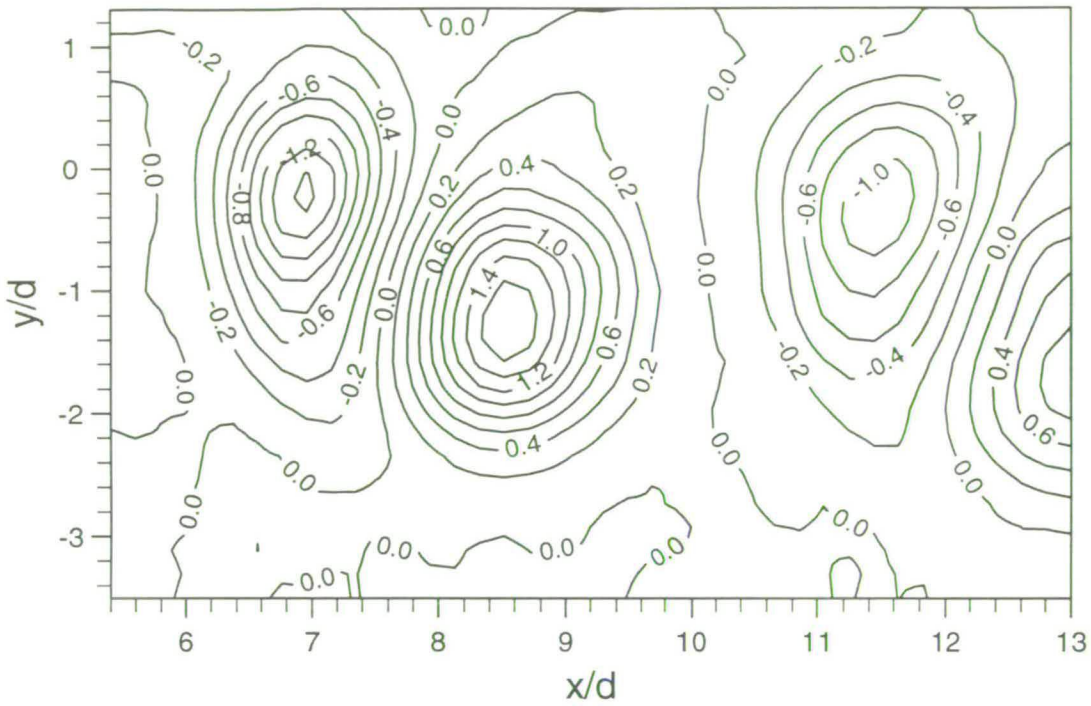

Figure 5.1: Vorticity plot (s^{-1}): $Re = 100$, $S = 0.3$

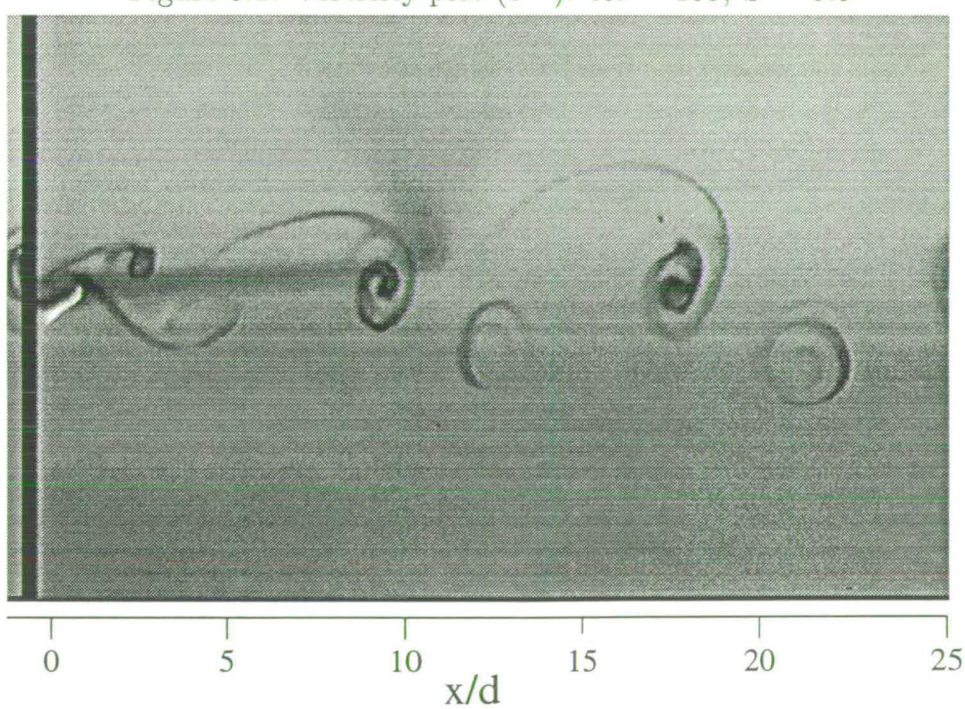

Figure 5.2: Flow visualisation: $Re = 100$, $S = 0.3$

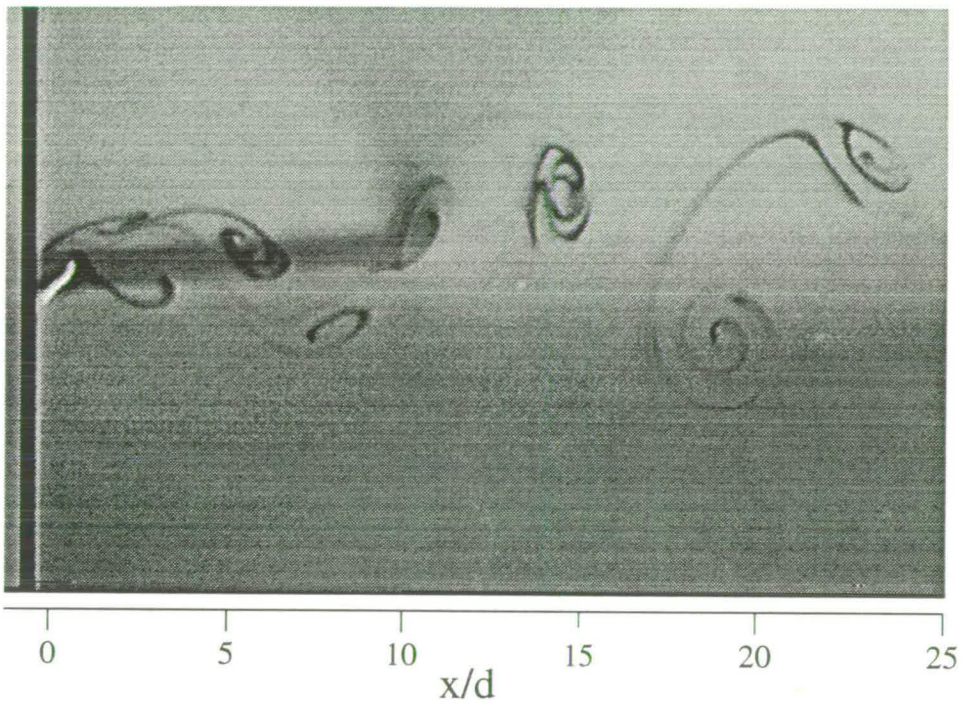

Figure 5.3: Flow visualisation: $Re = 100$, $S = 0.5$

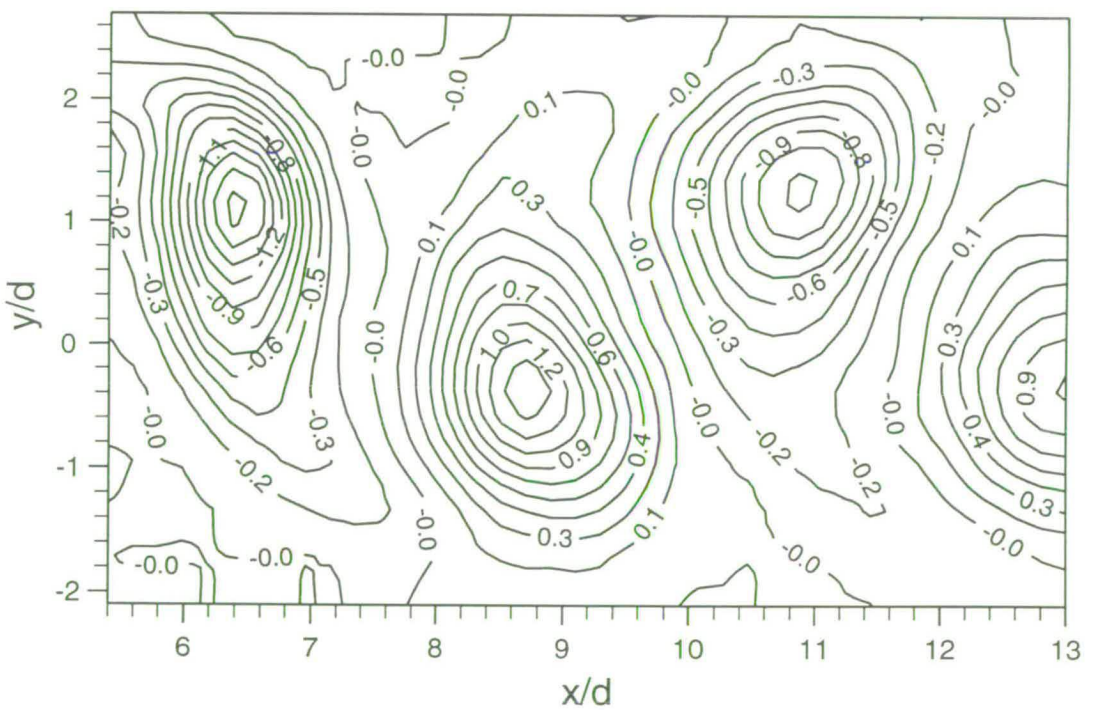

Figure 5.4: Vorticity plot (s^{-1}): $Re = 100$, $S = 0.65$

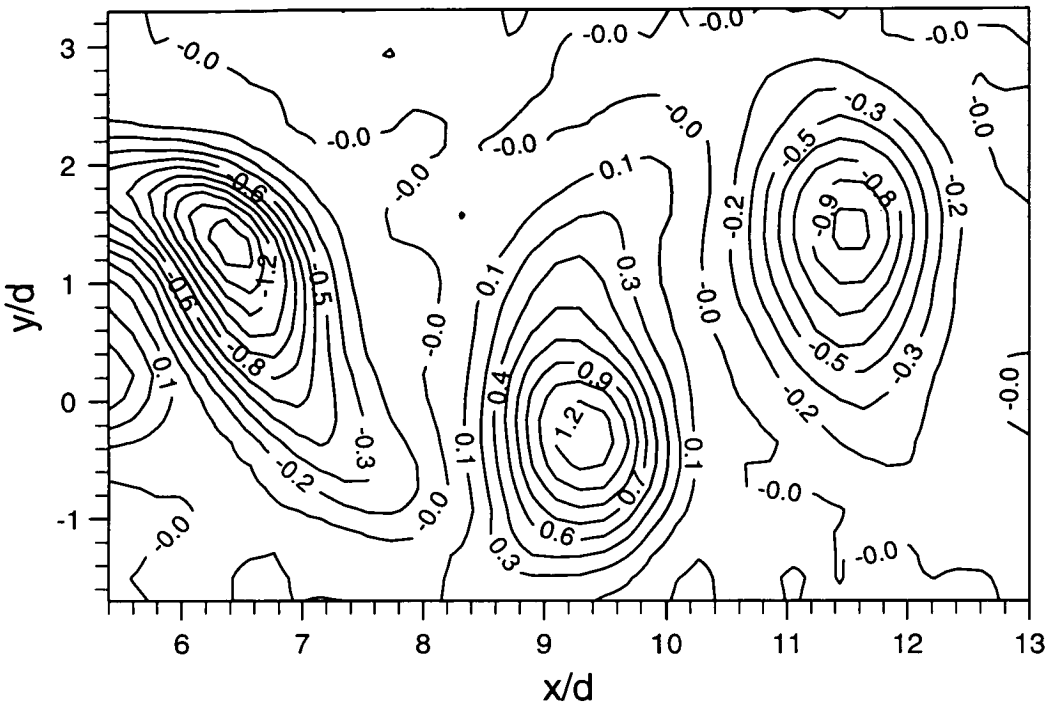

Figure 5.5: Vorticity plot (s^{-1}): $Re = 100$, $S = 0.8$

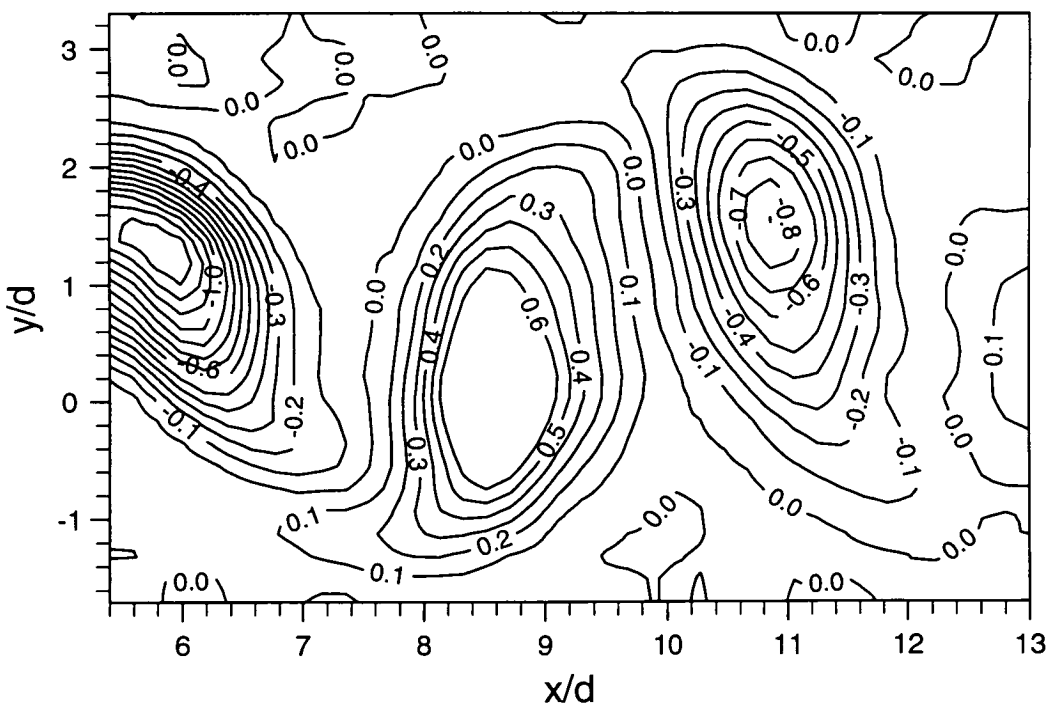

Figure 5.6: Vorticity plot (s^{-1}): $Re = 100$, $S = 1.0$

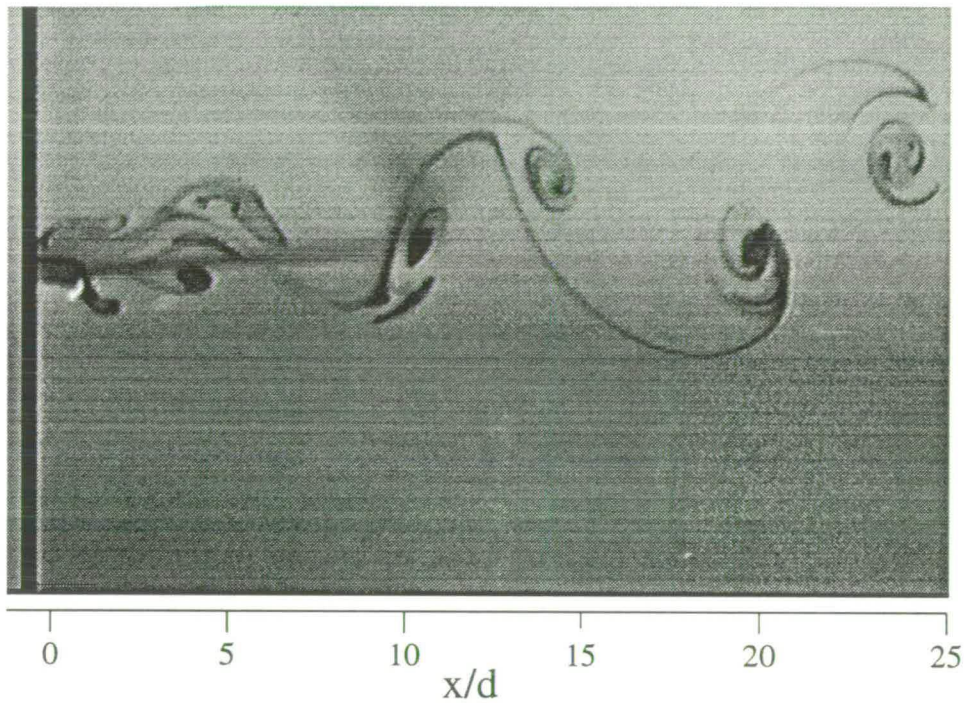

Figure 5.7: Flow visualisation: $Re = 100$, $S = 1.0$

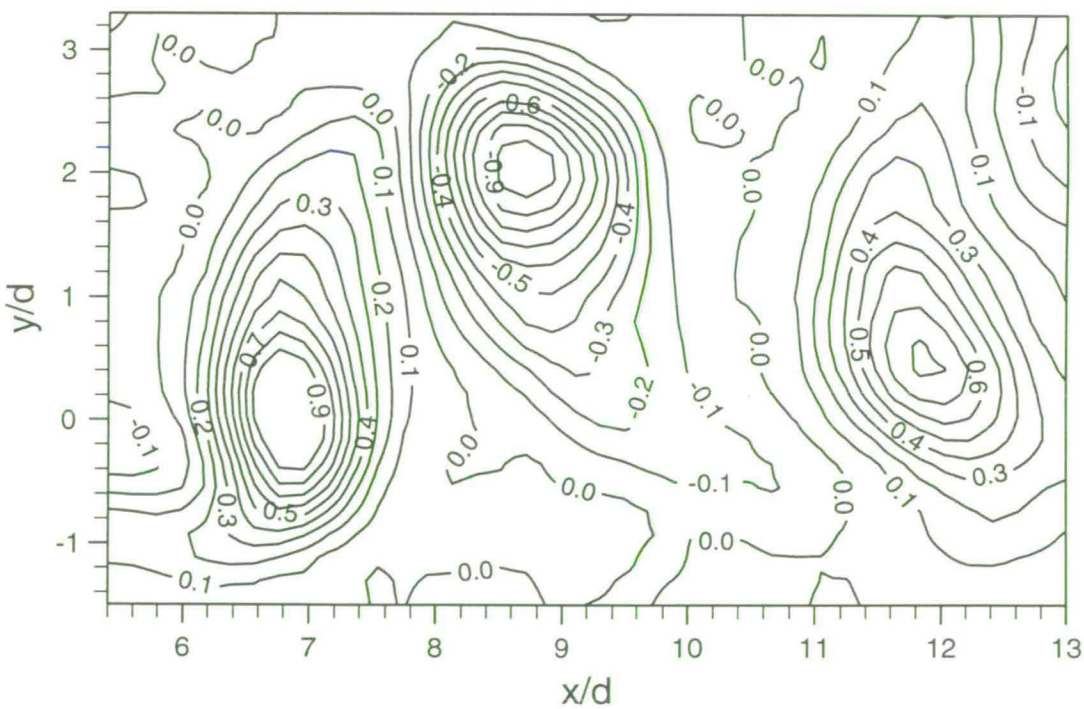

Figure 5.8: Vorticity plot (s^{-1}): $Re = 100$, $S = 1.4$

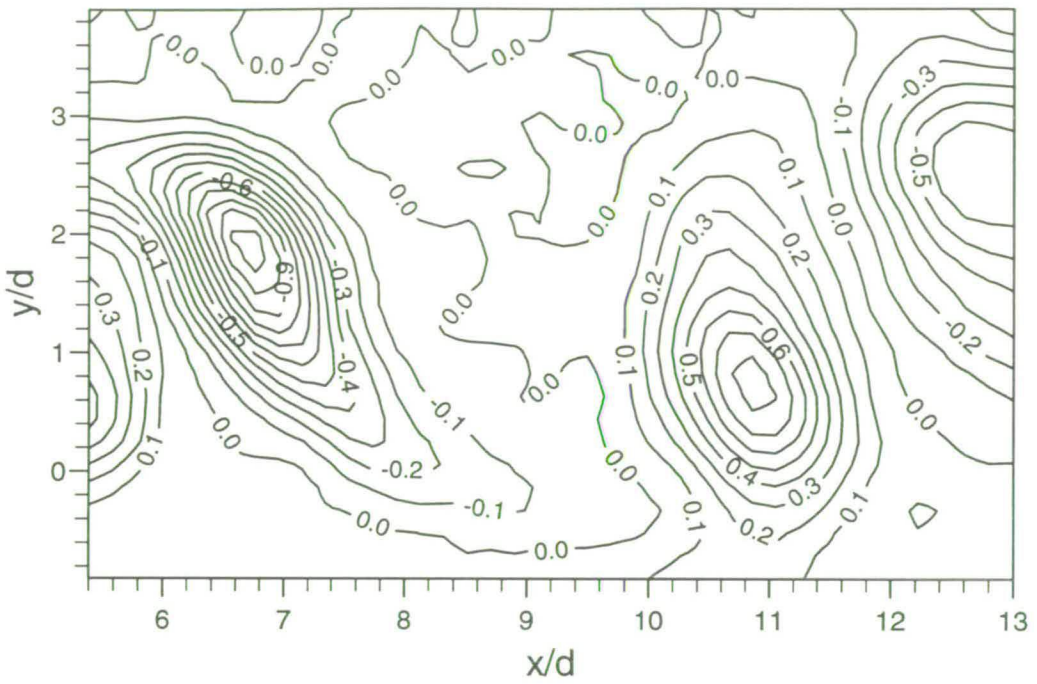

(a) Phase: T

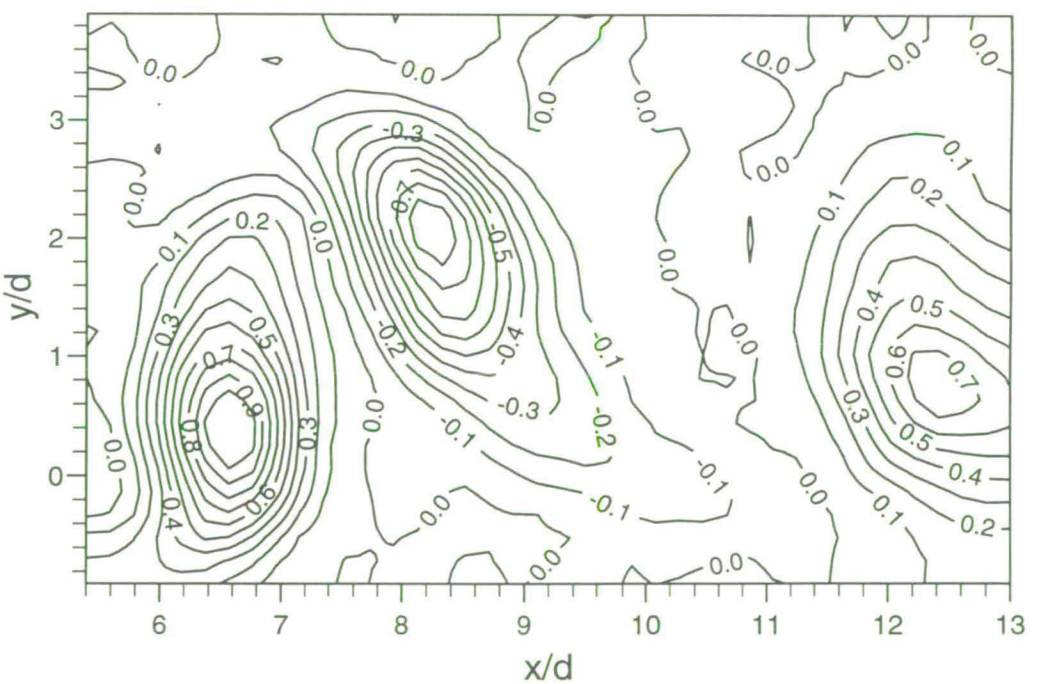

(b) Phase: $2T$

Figure 5.9: Vorticity plot (s^{-1}): $Re = 100$, $S = 1.8$

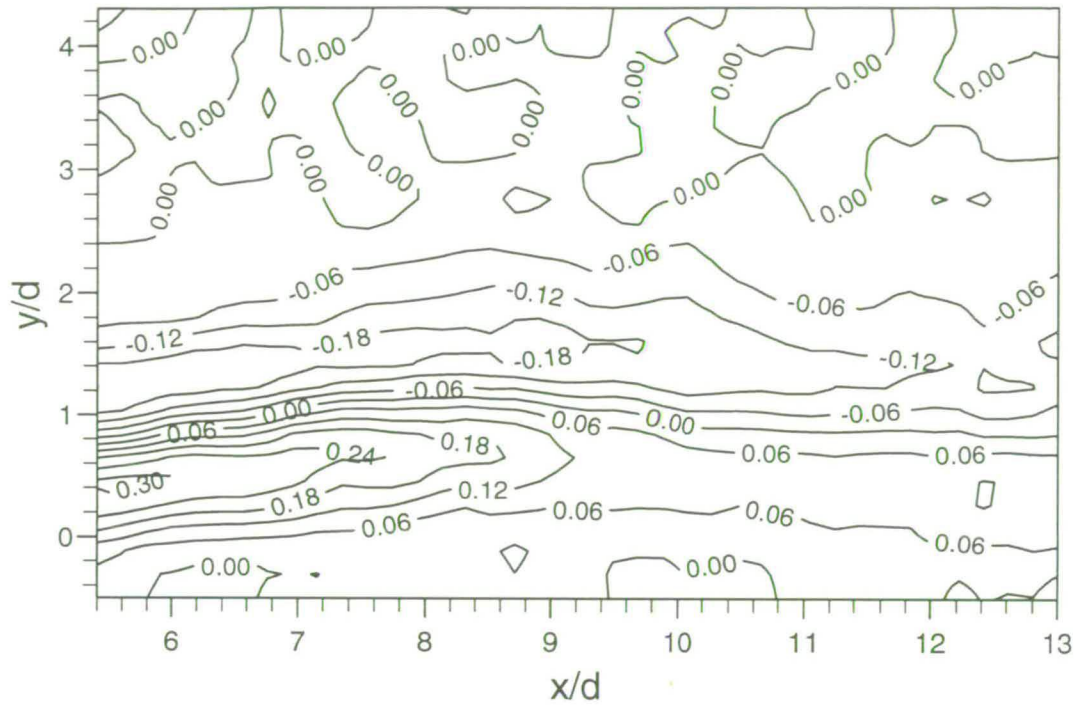

Figure 5.10: Vorticity plot (s^{-1}): $Re = 100$, $S = 2.4$

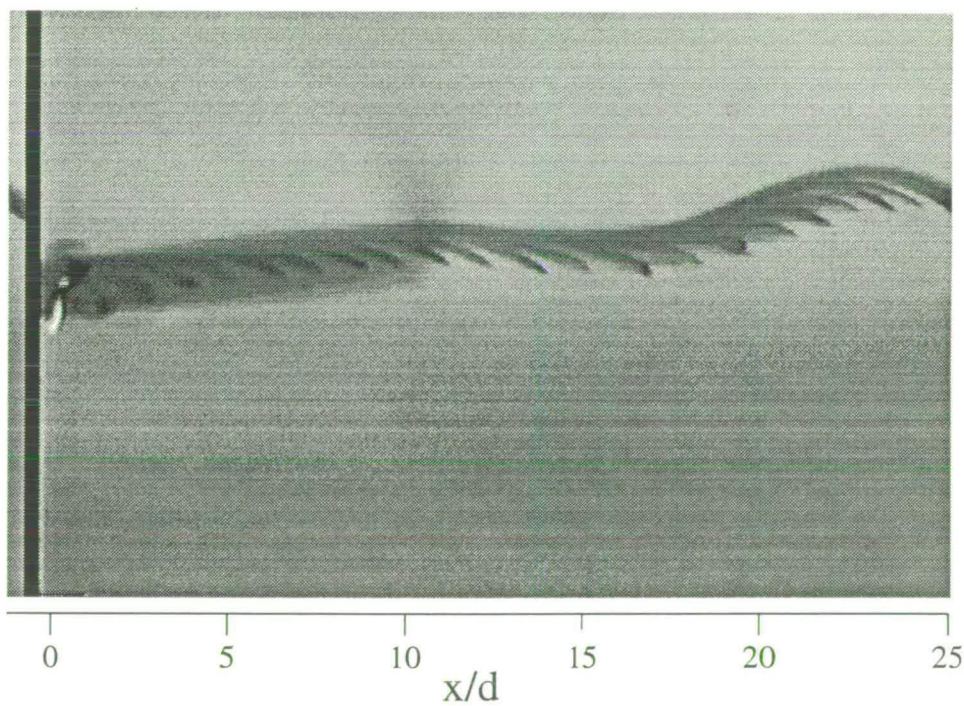

Figure 5.11: Flow visualisation: $Re = 100$, $S = 2.4$

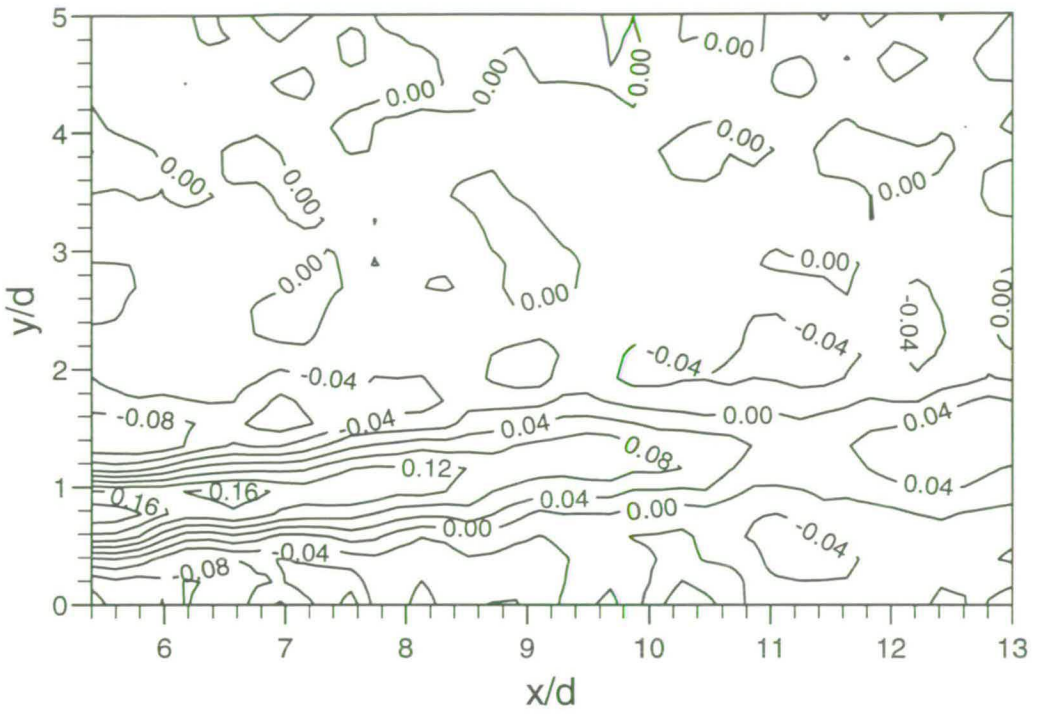

Figure 5.12: Vorticity plot (s^{-1}): $Re = 100$, $S = 3.5$

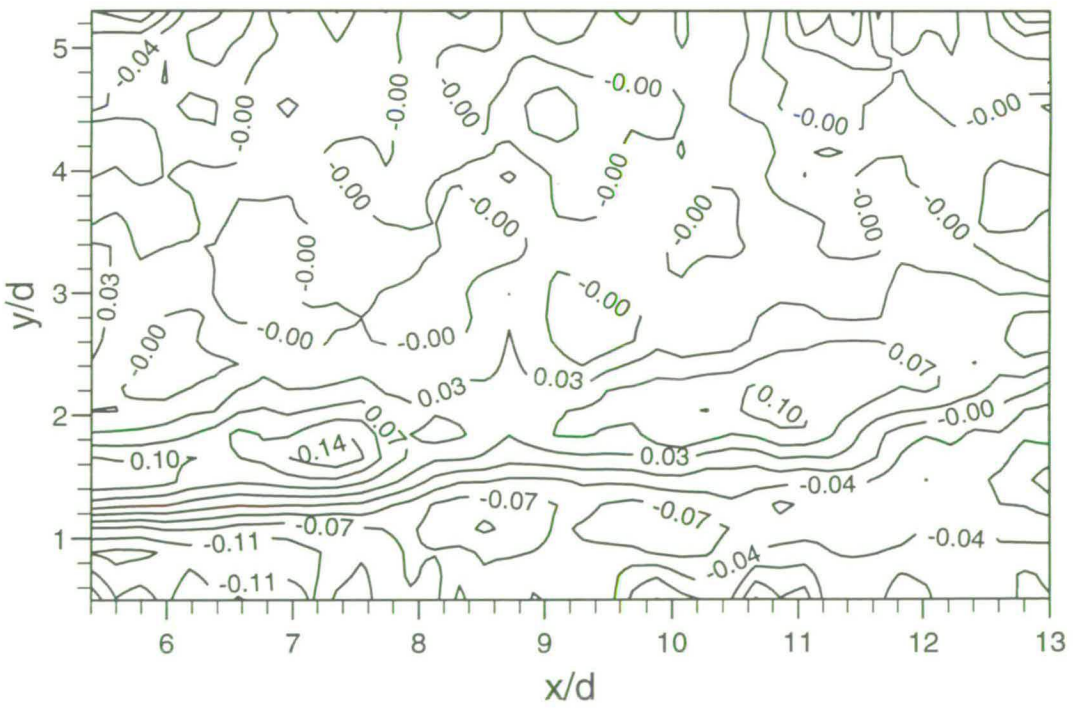

Figure 5.13: Vorticity plot (s^{-1}): $Re = 100$, $S = 4.5$

Spin Parameter: 0.8

At $S = 0.8$ the regularity in position of vortices in the same phase position is lost and the vortex sequence is different each half period. Figure 5.5 shows a typical frame taken at one of the two phase orientations available. Within this frame, the vortex at approximately (6.6, 1.4) has a very different orientation from those at $x/d \approx 9.4$ and 11.4.

Spin Parameter: 1.0

The example vorticity plot at $S = 1$ (Figure 5.6) shows that the vortices in the centre of the field of view do not have a vertical orientation. Their sense of rotation can be seen in the figure. Frames were taken at intervals of one plate period. The position of the vortices from frame to frame is not regular.

A flow visualisation picture taken at this spin parameter can be seen in Figure 5.7. At this spin parameter both the positive and negative vortices are an amalgam of more than one vortex. Sometimes three vortices combine whilst at other times, four vortices combine. The periodicity of the vortices is 3.5 half turns of the plate.

Spin Parameter: 1.4

Frames were taken at half blade period intervals for this spin parameter and a frame taken at one of phase positions is shown in Figure 5.8. The positive vortex at (6.8, 0) is effectively vertically orientated, whilst its negative partner is slightly inclined. Overall the frames show a periodicity of $5T/2$ where T is the rotational period of the plate. That is, the nth and the $(n + 5)$th frame have the x/d and y/d positions of the vortices to within $\pm$ 0.2 d of each other.

Spin Parameter: 1.8

Figures 5.9(a) and 5.9(b) show frames taken at T and 2 T. Over the period, the vortex at $x/d \approx 11.2$ convects to $x/d \approx 12.8$ whilst its cross-stream position remains constant at $y/d \approx 0.8$. The vortex at $x/d \approx 7$ in Figure 5.9(a) convects and slightly rotates to $x/d \approx 8.4$ a period later but is still far less vertically orientated than its positive partner.

Spin Parameter: 2.4

Figure 5.10 shows a vorticity plot taken from one experimental run at $S = 2.4$. This frame was taken 21 T after the plate had been simultaneously started rotating and translating. There is a thin band of negative vorticity between $0.9 \leq y/d \leq 1.7$ and a positive band between $0 \leq y/d \leq 0.7$ but the magnitudes of the vorticity of these bands are approximately only 10% the maximum value of the vorticity at $S = 1.8$. The separate coherent structures which have been previously a feature of the wake are no longer present.

When the flow is visualised using the dye, it can be seen that 'loops' of vorticity form in the wake (Figure 5.11). Vorticity is created every half period but apart from an initial negative vortex, there is no roll up into coherent structures.

Spin Parameter: 3.5

There is little change between the appearance of the wake at $S = 3.5$ and that at 2.4 apart from the sequence and position of the vorticity band. In this case, the band extends between $y/d \approx 0$ to $y/d \approx 2.0$ and a layer of positive vorticity is sandwiched between layers of negative vorticity. Again, the magnitude of this vorticity is between approximately 5% to 10% the maximum at $S = 1.8$.

Spin Parameter: 4.5

$S = 4.5$ was the highest spin parameter which could be produced by the rotation system at a Reynolds number of 100. The frame shown was taken at 33 T. It can be seen there is a positive band of vorticity at $y/d \approx 1.5$ and a negative one at $y/d \approx 0.9$.

5.2.2 Reynolds number: 200

Spin Parameter: 0.3

The vortex pair can be seen in Figure 5.15 at $x/d = 8.8$ and 10.6 for the negative and positive vortices respectively. As at Reynolds number 100, two vortices are shed at each half turn of the plate (one from each edge) and the x and y positions of the vortices are regular ($\pm$ 0.2 d) from frame to frame. Again the difference in shape between inner and outer sides of the vortices is probably an effect of the induced strain field.

At $S = 0.3$ the photograph of the flow (Figure 5.16) has the same appearance as that at $Re = 100$ except that the angle the vortex pair makes with the wake centreline is larger.

Spin Parameter: 0.5

The shedding pattern at $S = 0.5$ is more complicated than those at the other studied spin parameters. This complexity is not visible in the vorticity plot (Figure 5.17). However, it can be seen that unusually there is an positive vortex with a cross-stream position normally associated with that of a negative vortex ($y/d = 0.6$).

Flow visualisation reveals the shedding sequence illustrated in Figure 5.14. For positive vortices (A to D) and negative vortices (1 to 4) shed sequentially at each half turn of the plate, the resulting convected vortices are as follows. Vortices A and 1 are single vortices but the next two positive vortices (B and C) combine with the second negative vortex to form an overall positive vortex. The next negative vortex (3) convects as a single vortex but the fourth interacts with vortex D to form a double with net positive rotation. The sequence then repeats. Hence the overall shedding period is twice that of the plate. A flow visualisation of the vortices is shown in Figure 5.18.

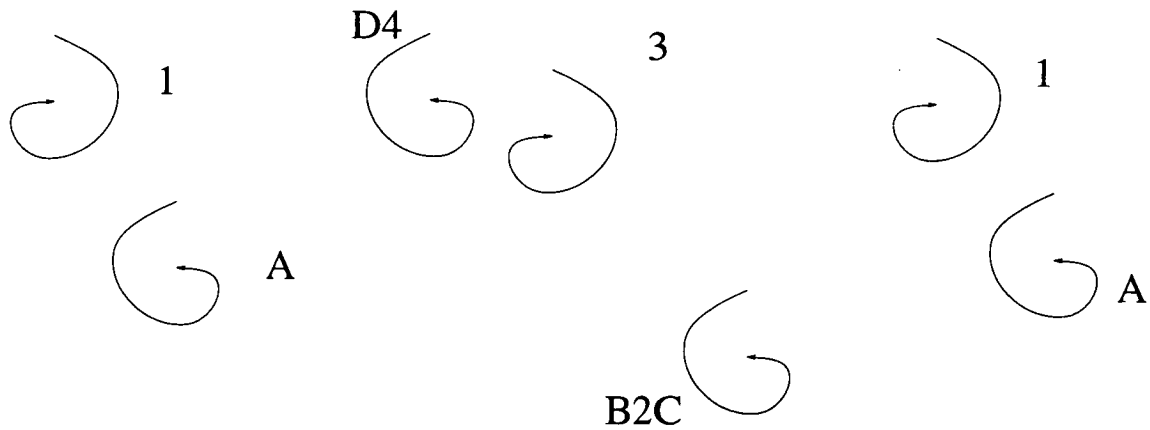

Figure 5.14: Vortex shedding sequence at $S = 0.5$ for $Re = 200$

Spin Parameter: 1.0

When the spin parameter is increased to $S = 1$, the shedding returns to a familiar vortex pairing. Both vortices are circular in shape and are shed above the wake centreline (Figure 5.19).

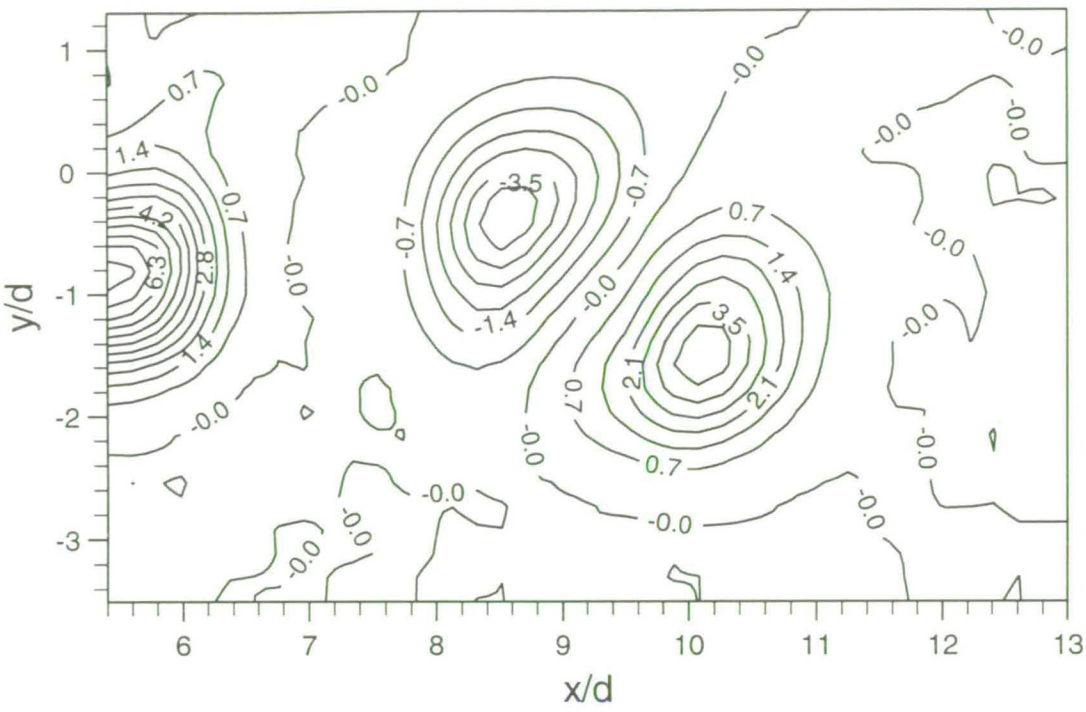

Figure 5.15: Vorticity plot (s^{-1}): $Re = 200$, $S = 0.3$

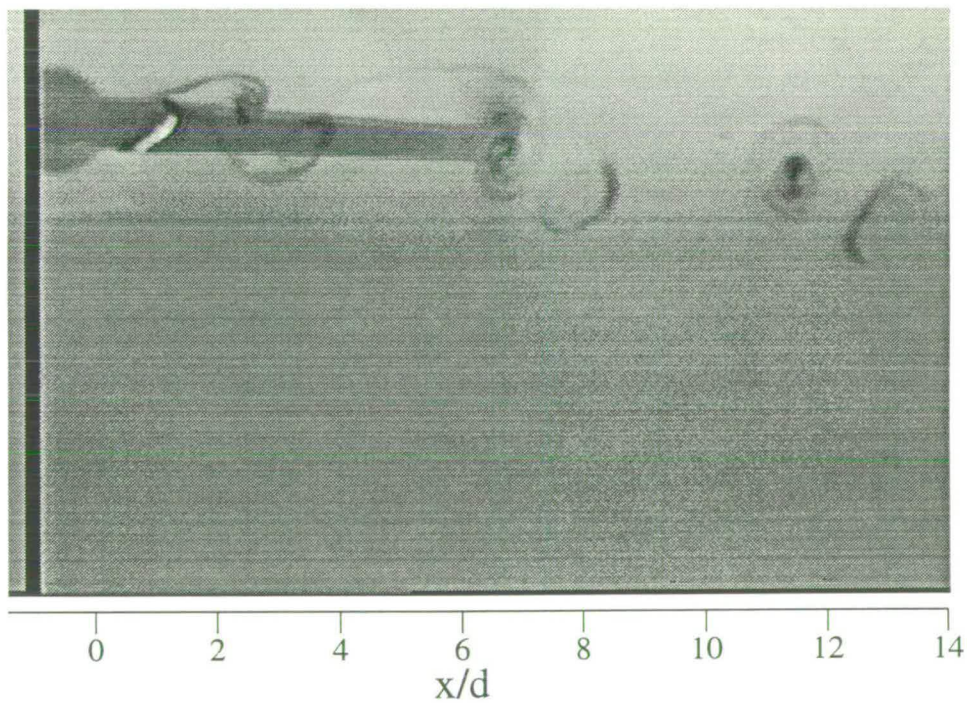

Figure 5.16: Flow visualisation: $Re = 200$, $S = 0.3$

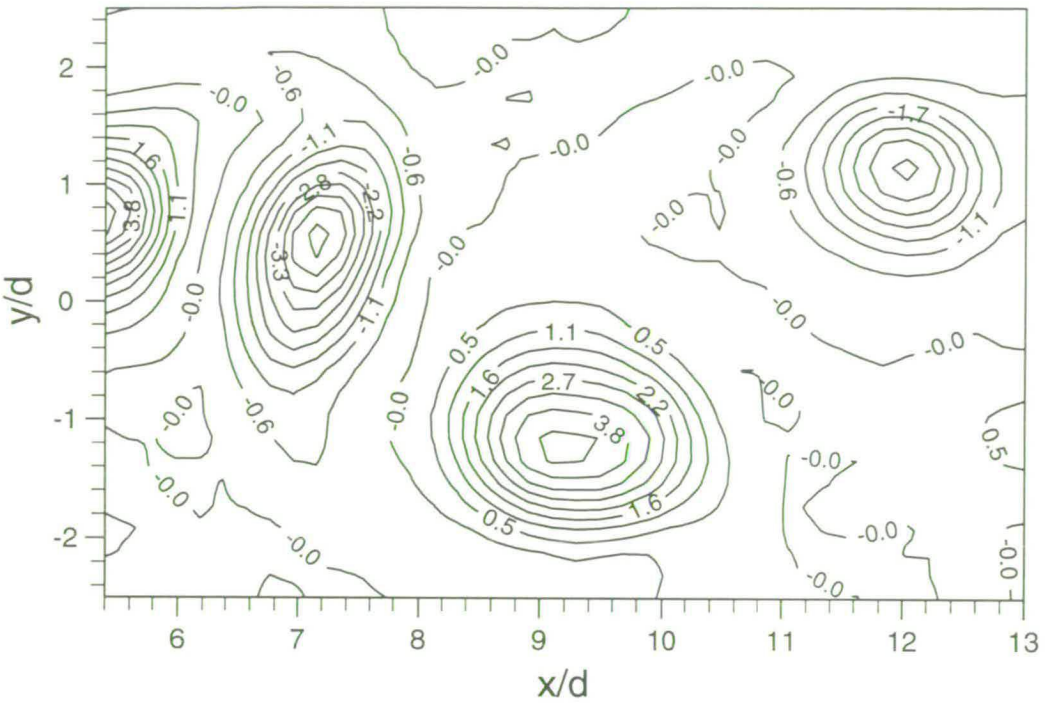

Figure 5.17: Vorticity plot (s^{-1}): $Re = 200$, $S = 0.5$

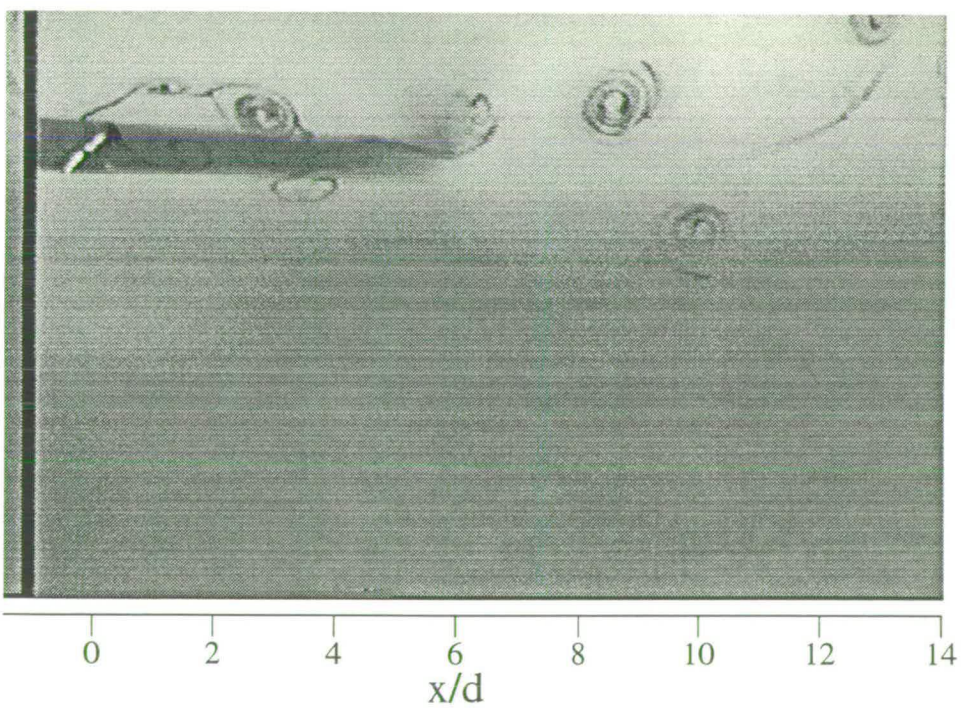

Figure 5.18: Flow visualisation: $Re = 200$, $S = 0.5$

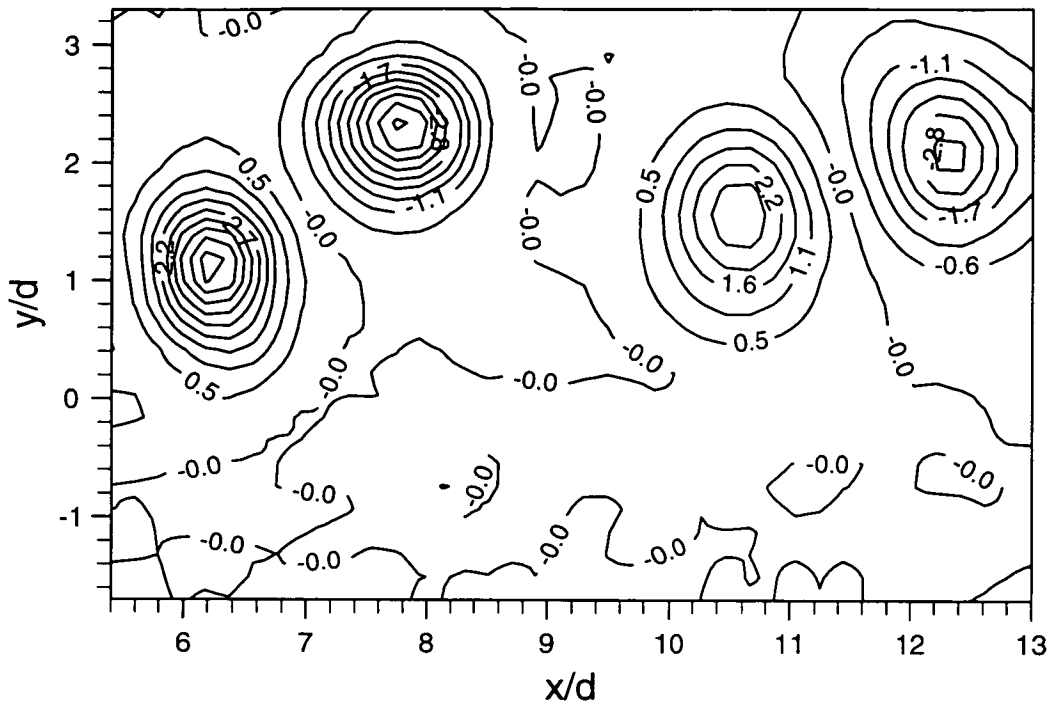

Figure 5.19: Vorticity plot (s^{-1}): $Re = 200$, $S = 1.0$

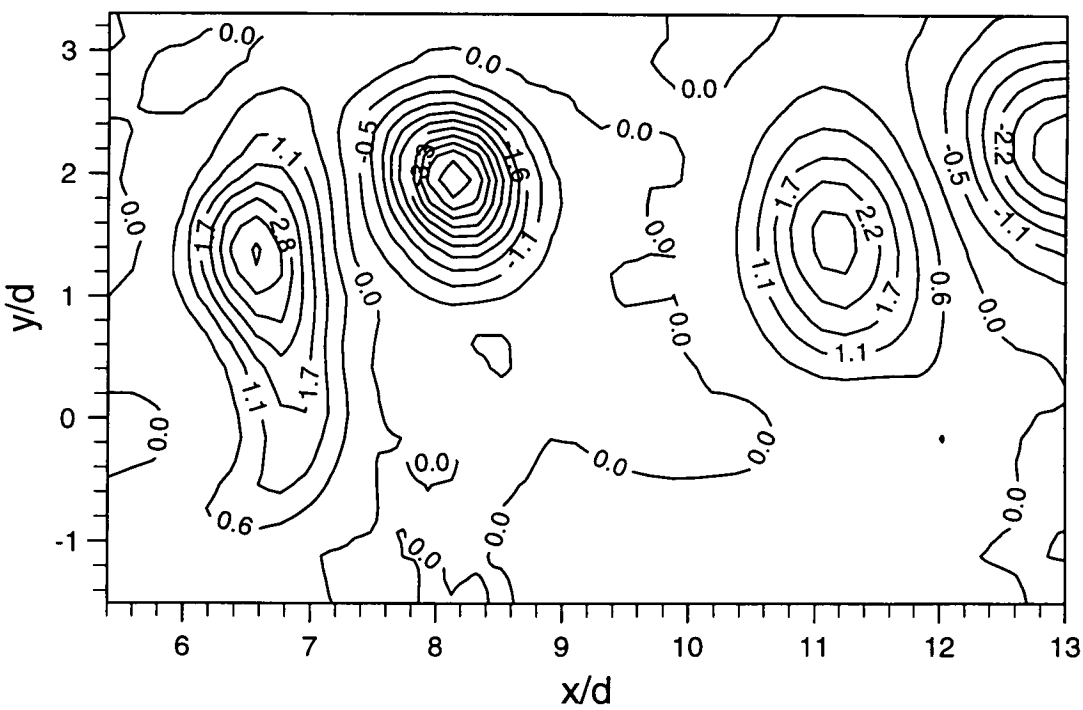

Figure 5.20: Vorticity plot (s^{-1}): $Re = 200$, $S = 1.4$

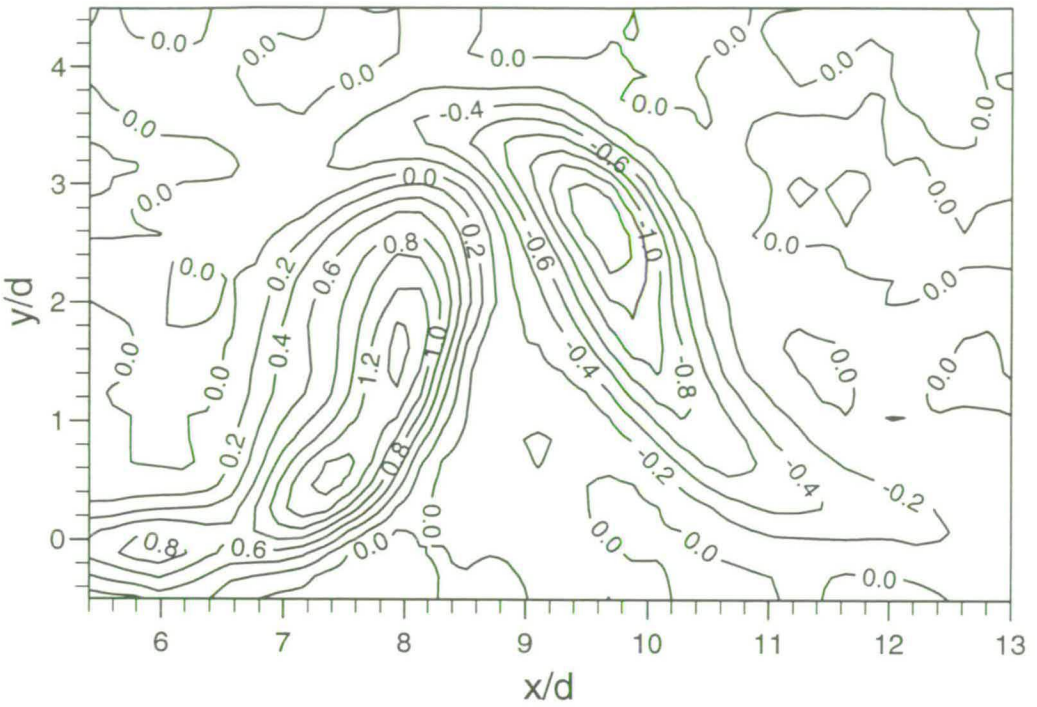

Figure 5.21: Vorticity plot (s^{-1}): $Re = 200$, $S = 2.4$

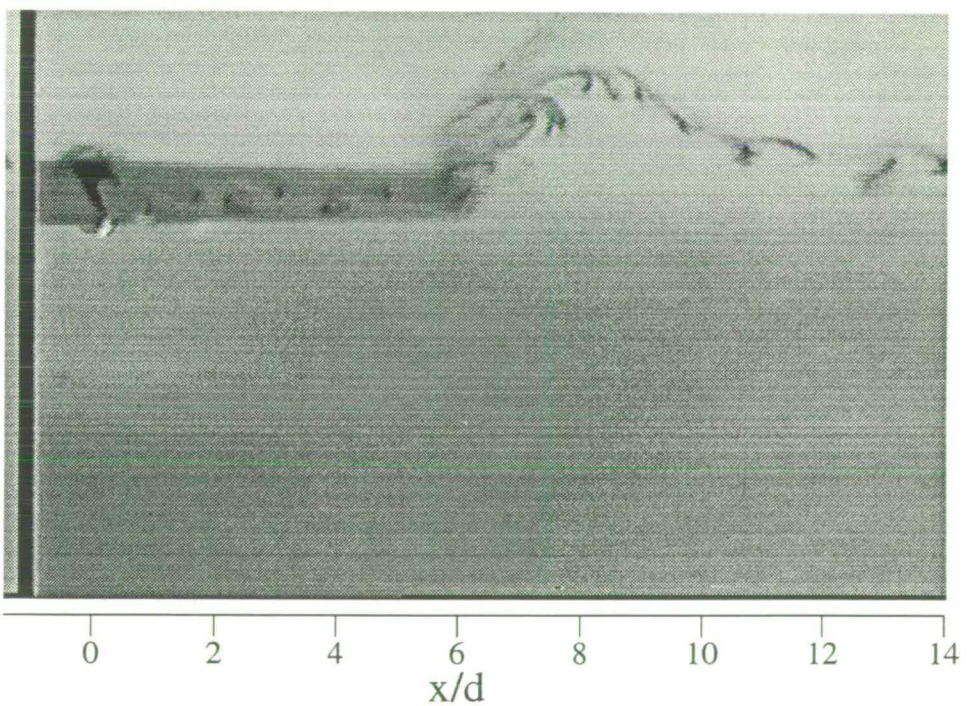

Figure 5.22: Flow visualisation: $Re = 200$, $S = 2.4$

Spin Parameter: 1.4

At $S = 1.4$ the negative vortex of the pair ($x/d = 8.6$) is circular in shape whilst the positive ($x/d = 6.8$) is thinner and extended in the cross-stream direction. The latter vortex becomes less stretched as it convects downstream. Figure 5.20 shows that the vortices are shed into the region of the wake above the centreline.

Flow visualisation at this spin parameter reveals that the number of plate half turns needed before a convecting vortex forms is increased and varies between either four and five giving a period of 4.5 half turns.

Spin Parameter: 2.4

The highest value of spin parameter possible with the system was $S = 2.4$. It is clear from Figure 5.21 that the vortices are very different from those at lower spin parameters. The frame shown was taken after 36 T and shows the steady flow condition. The vortices are long and stretched and it can not be seen in the field of view whether or not they rotate whilst convecting downstream.

Figure 5.22 shows a dye picture of the wake at $S = 2.4$. This picture was taken at a larger downstream distance than previously (from approximately $x/d = 26$ to 40). Closer to the plate just the feathered effect of the comparable $Re = 100$ picture is seen however, with the increase in distance, the wake rolls up to form weak vortex structures.

5.3 Wake Geometry

The wake geometry was determined from the vorticity plots. Distances were measured from vortex centre to vortex centre where these were taken to be the positions of maximum vorticity. Each analysed frame and hence vorticity plot was used in the calculations of the wake parameters. The values shown below are the averages of these calculations with the errors being the standard deviations from the mean.

5.3.1 Reynolds Number: 100

Figure 5.23 shows the variation of the wake geometry parameters as the spin parameter is increased from 0.3 to 1.8. The wavelength of the vortices shows an overall trend of increasing as the spin parameter increases (Figure 5.23). The wavelength for $S = 0.3$ is the same as that for $S = 0.65$ with a value of 4.4 ± 0.2

d. This increases to (5 ± 0.2) d for $S = 0.8$, 1.0 and 1.4. When the spin parameter is increased to 1.8 the wavelength is (5.8 ± 0.2) d.

The streamwise distance between the vortex pairs, x_p/d, increases from a value of 1.7 at $S = 0.3$ to approximately a constant value of 2.1 for $0.65 \leq S \leq 1.4$ and then decreases again at $S = 1.8$.

The cross-stream distance between the pairs, b/d, follows a similar trend to that of the streamwise. At $S = 0.3$, $b/d = 0.9$ which then increases to a constant level for the rest of the spin parameter range ($b/d \approx 1.4 \pm 0.2$).

The downstream progress of individual vortices was tracked using consecutive frames. The change in x/d of these vortices together with the time between frames was used to calculate their convection velocity, U_v. Figure 5.24 illustrates the variation of U_v with spin parameter and it can be seen that the convection velocity remains constant, to within experimental error, for $S \leq 1.4$. Above this spin parameter U_v increases.

5.3.2 Reynolds Number: 200

The wake parameters at Reynolds number 200 are shown in Figure 5.25. The shedding wavelength remains approximately constant over the range of spin parameter examined. The increase in wavelength as the spin parameter is increased from 0.3 at $Re = 100$, is not evident here at $Re = 200$.

The trends for both the streamwise and cross-stream vortex pair spacing are similar. Both parameters are constant to within experimental variation for spin parameters of 0.3, 1.0 and 1.4 ($x_p/d \approx 1.6$ and $b/d \approx 0.7$) but both show a large increase at $S = 0.5$.

5.3.3 Shedding Frequencies

The variation of the ratio of plate frequency to half the shedding frequency with spin parameter for $Re = 100$ and $Re = 200$ are shown in Figures 5.26(a) and 5.26(b). It can be seen from these figures that at $S = 0.3$ and $S = 0.5$ the quantity $2f_b/f_s$ has the same values at both Reynolds numbers, 1 and 2 respectively. The values at the other plotted spin parameters differ between the Reynolds numbers.

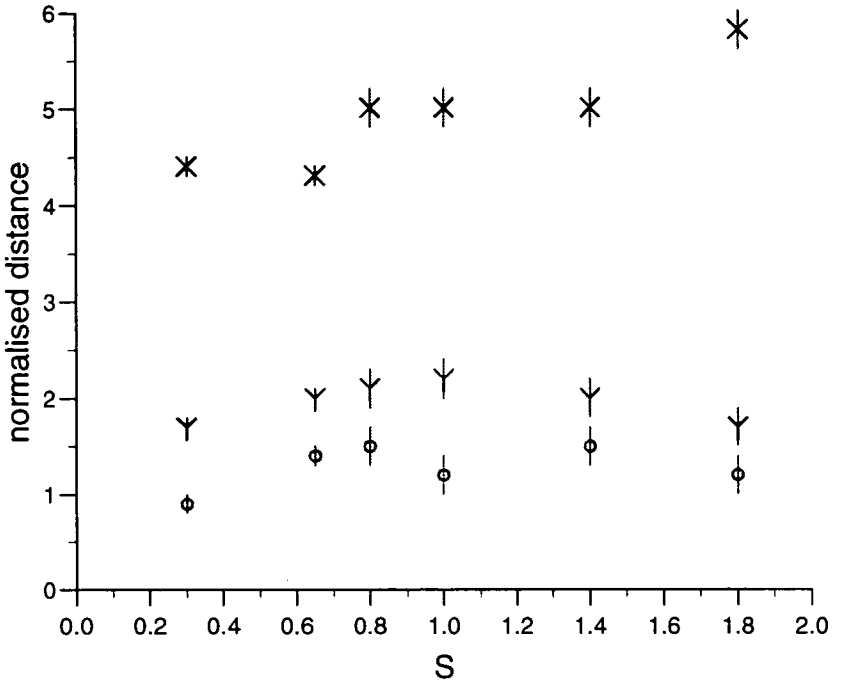

Figure 5.23: Wake Geometry for $Re = 100$: X, λ/d; Y, x_p/d; O, b/d

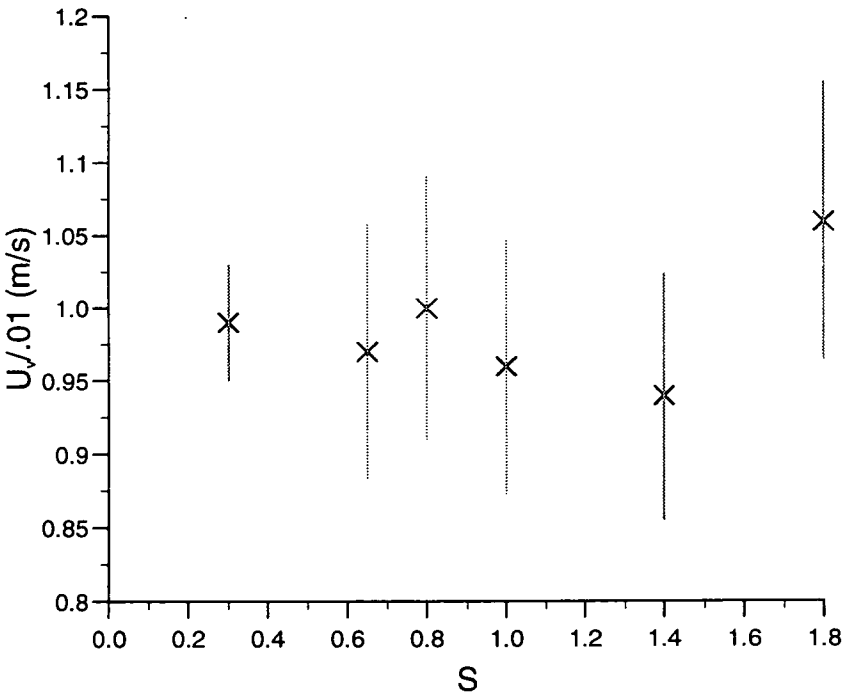

Figure 5.24: Variation of Vortex Convection Velocity with Spin Parameter at $Re = 100$.

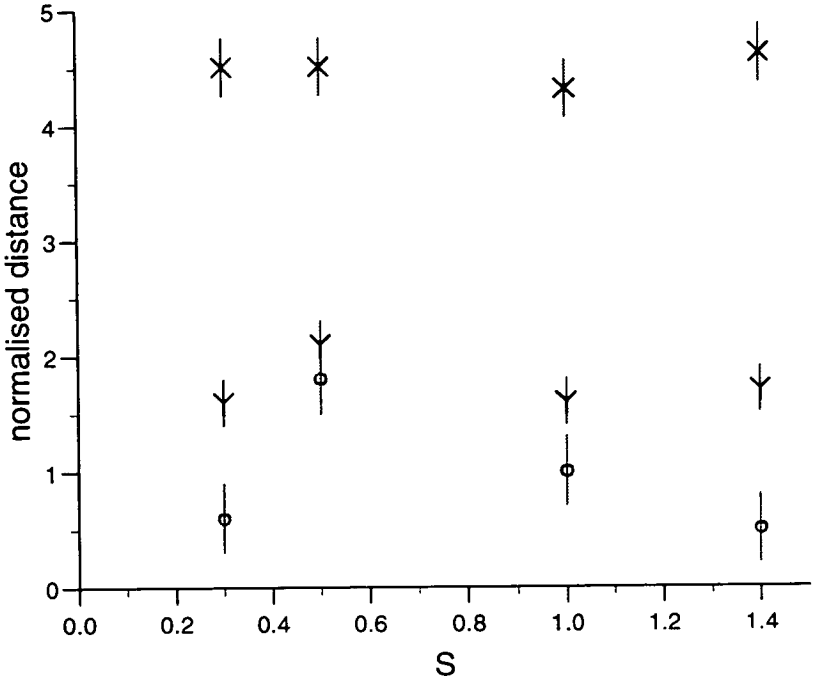

Figure 5.25: Wake Geometry for $Re = 200$: X, λ/d; Y, x_p/d; O, b/d

Apart from the values at $S = 0.5$, the points for $S \leq 1.4$ could be considered to be linear with an intersection at (0,0). However, when the spin parameter is increased to $S = 1.8$ for $Re = 100$, $2f_b/f_s$ increases to 7, which lies significantly above the extrapolated straight line through the values for $S \leq 1.4$. Thus, the fundamental frequency behaviour changes above $S > 1.4$ for $Re = 100$. This change has also been noted for $Re = 200$ by Barnes (private communication).

Since $U_v = \lambda f_s$, the previously calculated values of U_v can be used together with the shedding wavelength, λ, to estimate the shedding frequency of the flow. The estimated and measured values for $Re = 100$ match to within experimental error (Figure 5.27). The size of the error bars is due to the variation of the convection velocity which was of the order of 10% except at $S = 0.3$ when it was $\approx 4\%$. This error results from the variation of the wavelength from frame to frame.

The Strouhal number for the flow at $Re = 100$ within the constant frequency range can be calculated. It is found that it is approximately 13% higher than that for the flow from a non-rotating plate. The latter value can be calculated from equation 4.7.

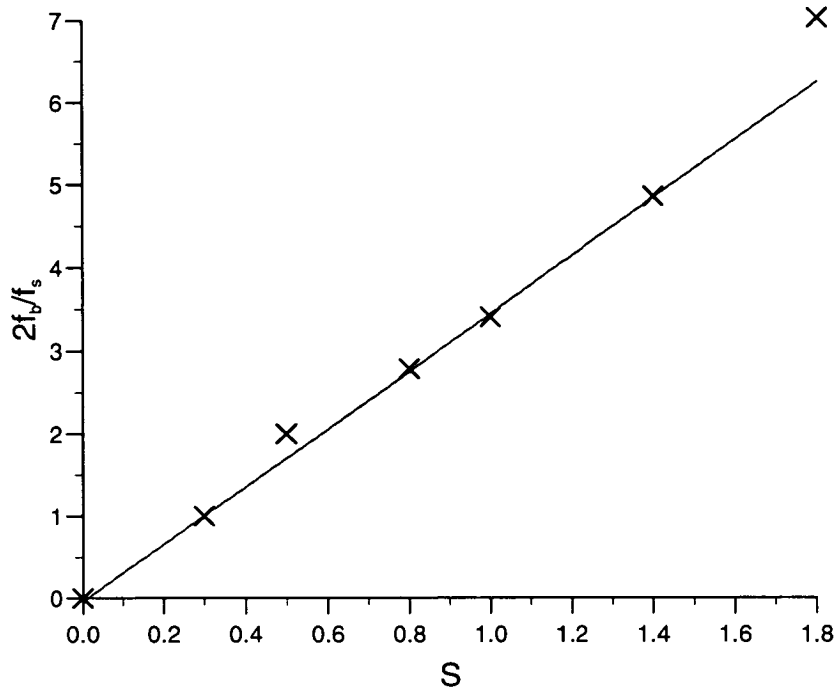

(a) $Re = 100$

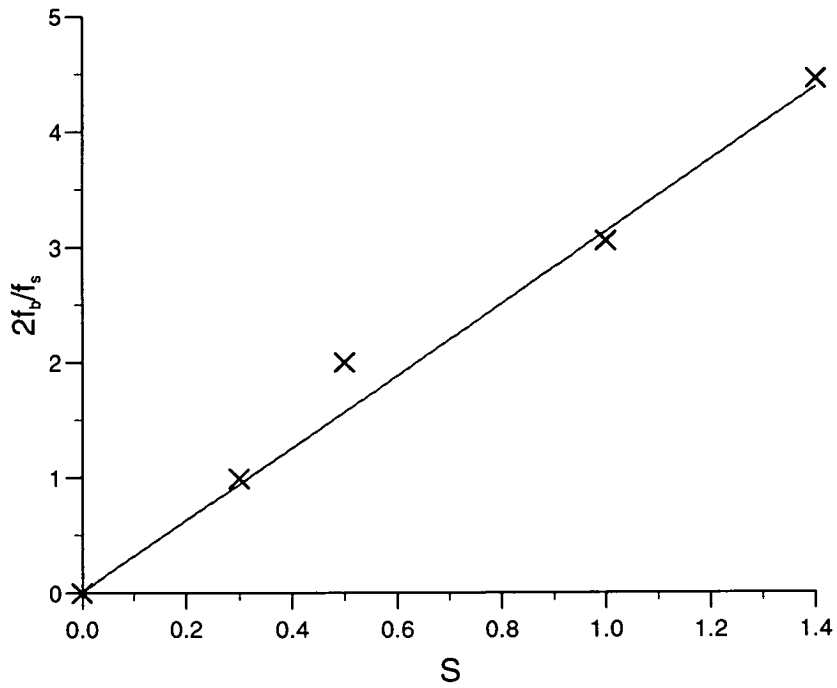

(b) $Re = 200$

Figure 5.26: Variation of Plate Rotational Frequency to Half Vortex Shedding Frequency with Spin Parameter: X, experiment; -, least squares best fit

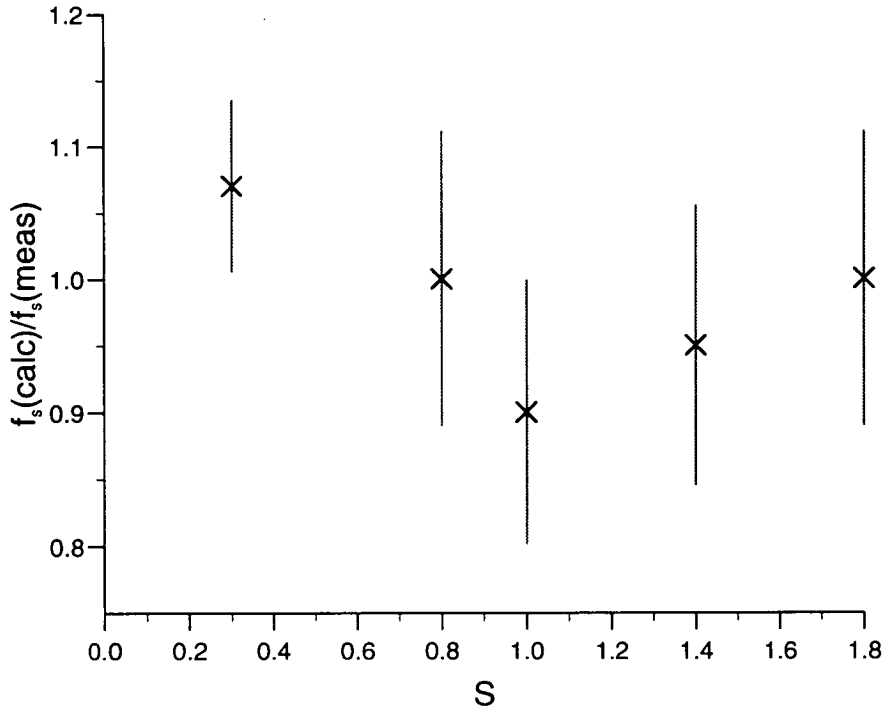

Figure 5.27: Comparison of Measured Vortex Shedding Frequency with Calculated Value from $f_s = U_v/\lambda$ for $Re = 100$

5.4 Vortex Strength Behaviour

The previous sections have shown that the shedding behaviour changes as the spin parameter is increased. This section considers if such shedding changes are reflected in the variation of vortex strength with spin parameter.

The vortices which were used in the calculations of the vortex strengths were those which were in a pair in the field of view. A vortex with a positive or negative partner missing from the frame was not used. Since at a particular spin parameter, the orientation of a pair is fixed this meant that the counted vortices generally were at same downstream distance. At $S = 0.65$ where there was no obvious pair formation, the vortices in the centre of the field of view were used.

Since the shedding at $S = 0.5$ for $Re = 200$ was more unusual than that at the other spin parameters, with both single, double and triple amalgam vortices being produced, the strengths of only single vortices were considered in these plots. In addition to these vortex selection procedures which were specific to the case of a rotating body, the usual criteria for vorticity summation were used (refer

to Section 3.3).

Figures 5.28 and 5.29 show the variation of normalised vortex strength with spin parameter for the positive and negative vortices at Reynolds numbers of 100 and 200. All plotted values are the mean strengths and the associated error is the standard deviation from the mean. At $Re = 100$, the normalised strength at $S = 0$ (the non-rotating case) has been included as a reference measurement.

At $Re = 100$ it can be seen the strengths of both sets of vortices decreases as the spin parameter increases. The positive vortex has strength of approximately 0.89 at $S = 0.3$ which reduces to 0.63 at $S = 1.8$, whilst the negative vortex decreases from 0.88 to 0.58 at the same spin parameters. The general trend at $Re = 200$ is the same as that at the lower Reynolds number. At $S = 0.3$ the strengths of the positive and negative vortices are 0.92 and 0.93 respectively which then decrease to 0.35 and 0.39 at $S = 2.4$. However, the behaviour at $S = 1.4$ would appear to be anomalous. This is discussed in Section 5.6.

The possibility of a growing asymmetry between the positive and negative pair vortices with increasing spin parameter was investigated and the results are plotted in Figure 5.30. It can be seen that at both $Re = 100$ and 200 there is little variation of K_-/K_+ with spin parameter. A difference between the two Reynolds numbers is that for $Re = 100$ the positive vortex appears to be stronger than the negative whilst at $Re = 200$ this condition has reversed.

5.5 Mean Wake Behaviour

As discussed in Section 1.3, wake control results from modifying the limit-cycle oscillation of the absolute instability of the wake. The instability characteristics of a flow are determined from analysis of the mean velocity profiles. Although such analysis is not attempted here and the downsteam positions are outside the region overwhich the wake is unstable (up to 5 radii, Karniadakis & Triantfyllou [48]), the mean velocity profiles are nonetheless useful indicators of changes within the flow regime.

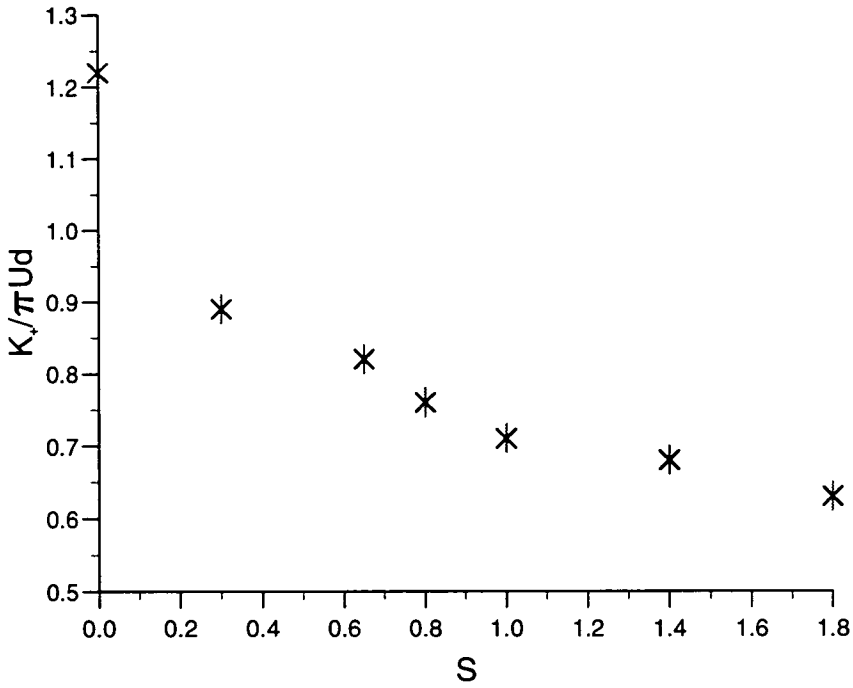

(a) Positive Vortex

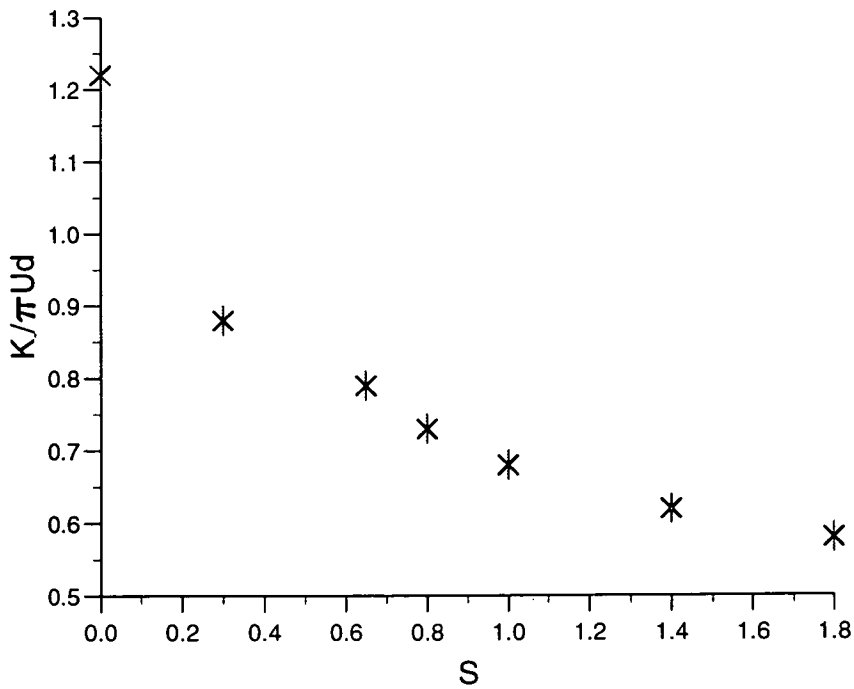

(b) Negative Vortex

Figure 5.28: Variation of Magnitude of Vortex Strength with Spin Parameter: $Re = 100$

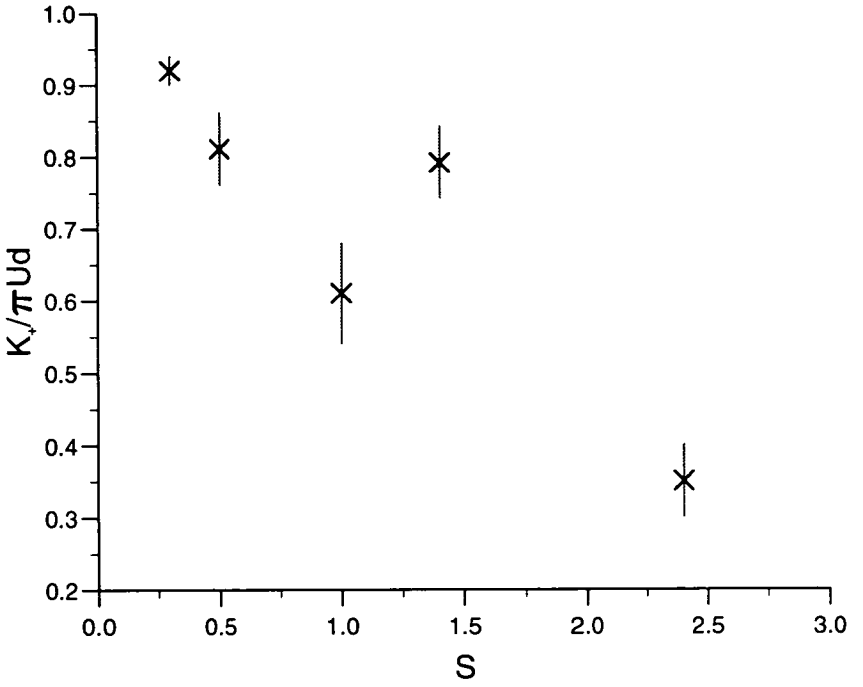

(a) Positive Vortex

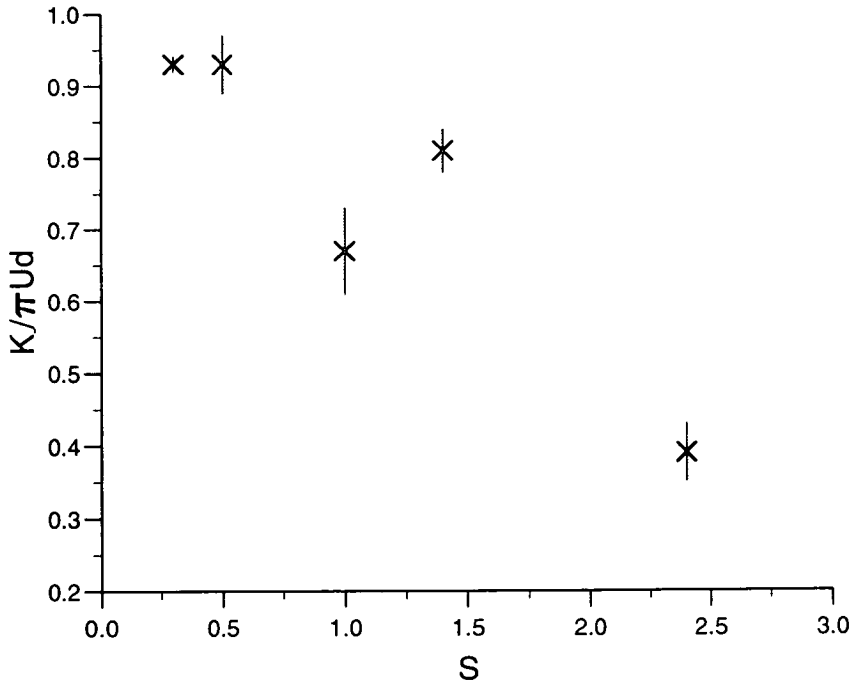

(b) Negative Vortex

Figure 5.29: Variation of Magnitude of Vortex Strength with Spin Parameter: $Re = 200$

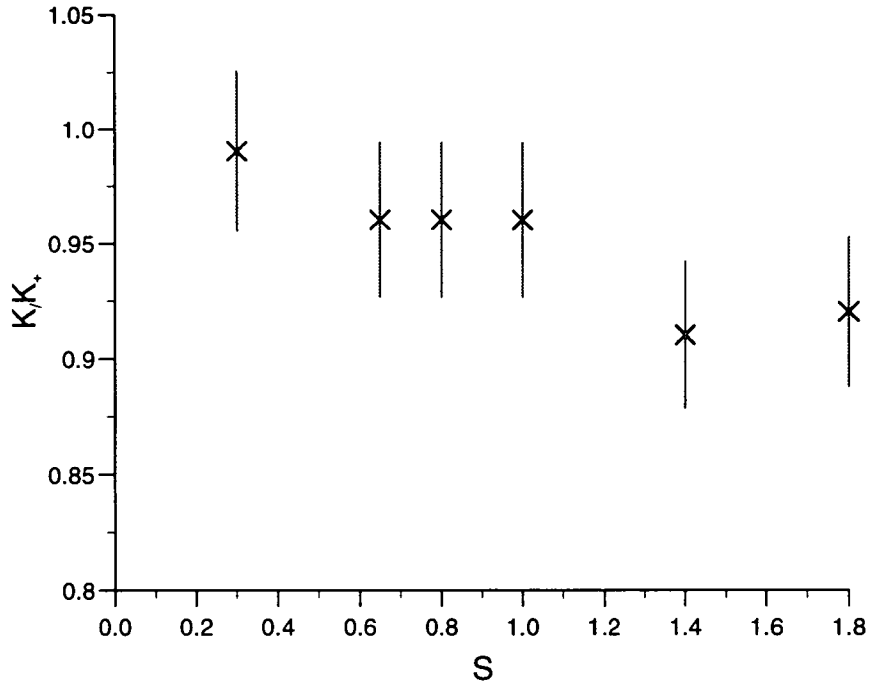

(a) $Re = 100$

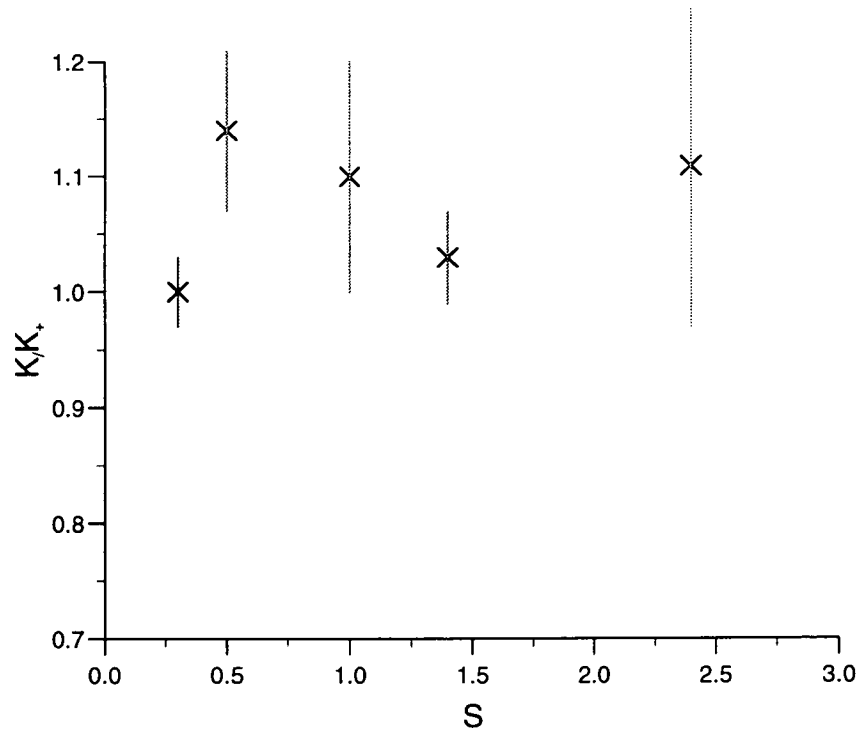

(b) $Re = 200$

Figure 5.30: Ratio of Vortex Pair Strength with Increasing Spin Parameter

5.5.1 Techniques

Mean Velocity Profiles

A PIV photograph gives an instantaneous velocity map of the studied flow field. This is in direct contrast to hot-wire techniques which build up an average picture of the flow at a point over time. In order to find the time-wise average velocity of the wake behind a rotating flat plate from velocity vector maps it was necessary to make the following assumption, that the mean streamwise velocity over a vortex shedding period at a particular cross-stream and downstream position could be approximated by averaging the streamwise velocities at the same cross-stream position over a wavelength of the shedding cycle.

$$\frac{1}{T}\int_0^T u dt \approx \frac{1}{n}\sum_{i=1}^{n} u(i) \tag{5.1}$$

for streamwise velocity points *u(i)* and *u(i+1)* being separated by a distance λ/n on the velocity map where λ is vortex wavelength, n the number of grid points over the wavelength and T is the shedding period.

A program was written to perform the averaging of the streamwise velocities over a wavelength. The program was used on each velocity field for which there was a shedding period present in the field of view. The exception to this was when the spin parameter was sufficiently high for the shedding to be suppressed. In this a slightly different method was used which will be described presently. For the velocity averaging, it was necessary to identify a common point on the vortices over which the wavelength could be easily defined. This was chosen to be the vortex centre. The co-ordinates of these positions on the velocity maps were assumed to coincide with the centres, or positions of maximum vorticity, on the vorticity maps. These positions had been previously identified for the vortex strength calculations. As discussed in Section 3.2, the reference frame for the velocity field was the one in which the carriage velocity had been subtracted. For $Re = 100$ where U_v/U was 0.89 ± 0.05 for $0.3 \leq S \leq 1.4$, the velocity at the vortex centre was approximately $0.21\ U$.

Hence the mean streamwise velocity profile in the cross-stream direction was found for each velocity map of a given spin parameter. A second program was used to find the average of these profiles for a given spin parameter. Thus the profiles which are shown below are derived from at least four velocity maps per spin parameter.

For the cases where there were no vortices present in the wake, the following procedure was adopted. Three sets of x/d positions were chosen within the field of view; $5.4 \leq x/d \leq 11.6$, $6.6 \leq x/d \leq 8.2$ and $8.6 \leq x/d \leq 11.4$. The streamwise velocities were averaged between each of these positions. These profiles were then averaged for each velocity map. The difference between the profiles taken between each of these streamwise positions was not significant. For the non-shedding spin parameters, the mean profiles shown below are the average of six to eight individual velocity maps for each spin parameter.

Half-Wake Width

The half-wake width, s_o, is calculated from the mean velocity profiles and a sketch showing how it is defined is shown in Figure 5.31. The value and cross-stream position of the maximum velocity deficit, u_m, were identified from the mean profile. The nearest y/d grid points corresponding to the positions of the $\pm u_m/2$ were then found. Hence, the value of s_o was calculated.

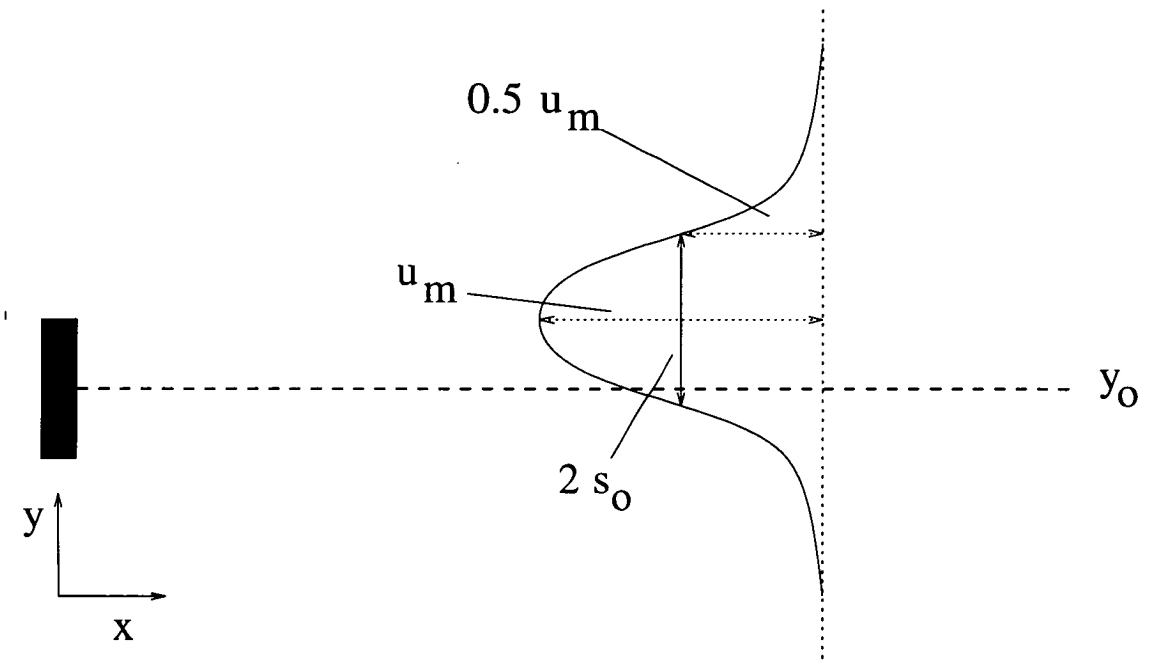

Figure 5.31: Definition of Half-Wake Width

5.5.2 Results

Wake Deficits

The mean velocity profiles of the wake at Reynolds number 100 can be seen in Figures 5.32 to 5.34. The velocities are normalised with respect to the carriage

velocity, U. It is clear that these profiles greatly change as the spin parameter is increased. The velocity profile at $S = 0$ was taken from velocity fields produced in Chapter 4. Looking at the profiles from $S = 0$ to $S = 0.8$ it can be seen that the velocity deficit decreases by approximately 60% as the spin parameter increases from zero to 0.3. This level then decreases by approximately 30% as the spin parameter increases from 0.65 to 0.8 but then remains constant at $u_{x/U} \approx 0.19$ until a decrease again at $S = 1.8$.

The major change in the wake profiles however is shown in Figure 5.34. The change in spin parameter from 1.8 to 2.4 corresponds to a change in the wake from a shedding to non-shedding regime. Over this spin parameter region the maximum value of the wake deficit decreases by approximately 50%. As the spin parameter is further increased the wake deficit again decreases until at $S = 4.5$ there is no longer a deficit but a surplus. At $S = 3.5$, the shape of the mean profile is different from that at other spin parameters since it is not symmetric about the position of maximum defect.

The behaviour of the mean velocity profiles at $Re = 200$ follows a similar trend (Figures 5.35 and 5.36). As the spin parameter is increased from zero to 0.3 the wake deficit decreases by approximately 80%. The deficit then increases at $S = 0.5$ but subsequently decreases to a value of 0.02 at $S = 2.4$. A brief experiment in which the plate was translated but not rotated was performed to provide a mean velocity profile for $S = 0$.

Maximum Position

Figure 5.37 illustrates the variation in cross-stream position of the maximum wake deficit, y_m/d with spin parameter for Reynolds number 100 and 200.

At $Re = 100$ this position changes from being coincident with the wake centreline when the plate is simply translated through the water to being below it by 0.7 d at $S = 0.3$ to 1.3 d above the centreline at $S = 1.8$. There is a slight decrease in y_m/d as the shedding is suppressed at $S = 2.4$ but the general upward trend continues and a value of 1.5 is reached at $S = 4.5$.

The non-rotating case at $Re = 200$ has its position of maximum deficit slightly below the wake centreline but this increases to approximately 1 d below at $S = 0.3$. The position of y_m/d then increases to be above the centreline as the spin

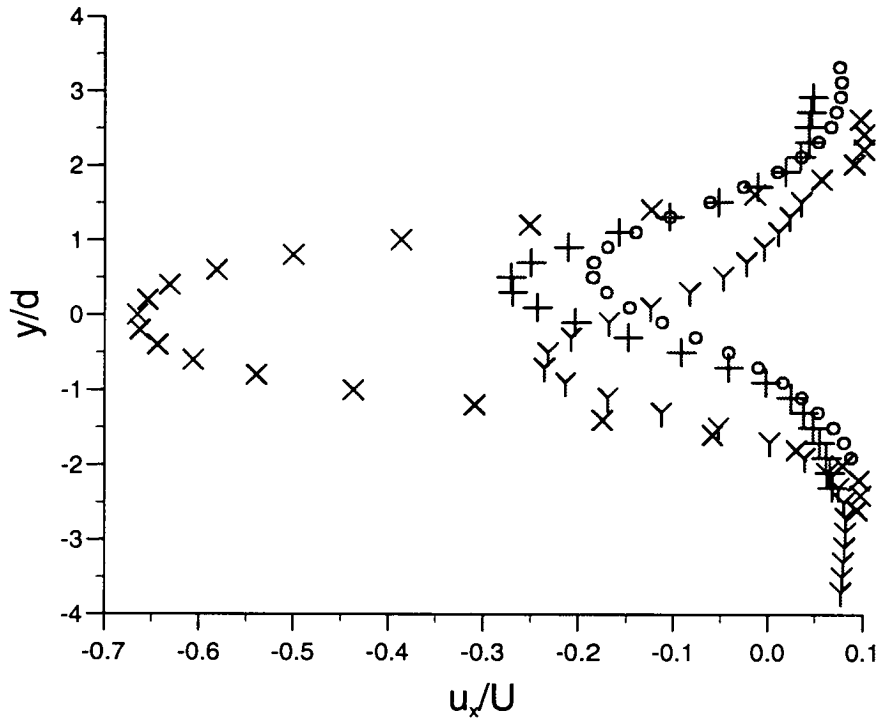

Figure 5.32: Mean Velocity Profiles, $Re = 100$: X, $S = 0$; Y, $S = 0.3$; $+$, $S = 0.65$; O, $S = 0.8$

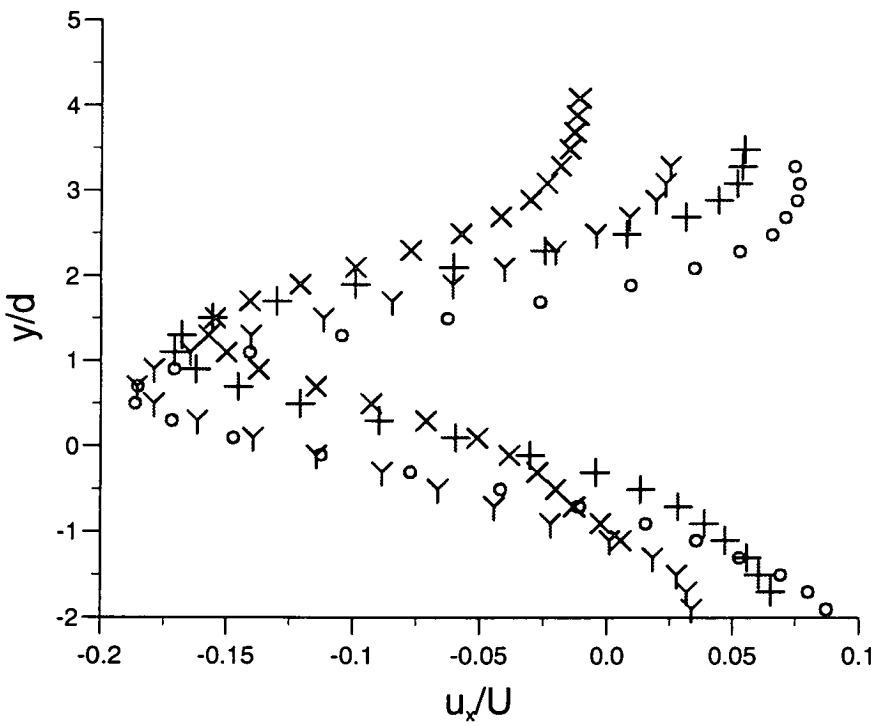

Figure 5.33: Mean Velocity Profiles, $Re = 100$: O, $S = 0.8$; Y, $S = 1.0$; $+$, $S = 1.4$; X, $S = 1.8$

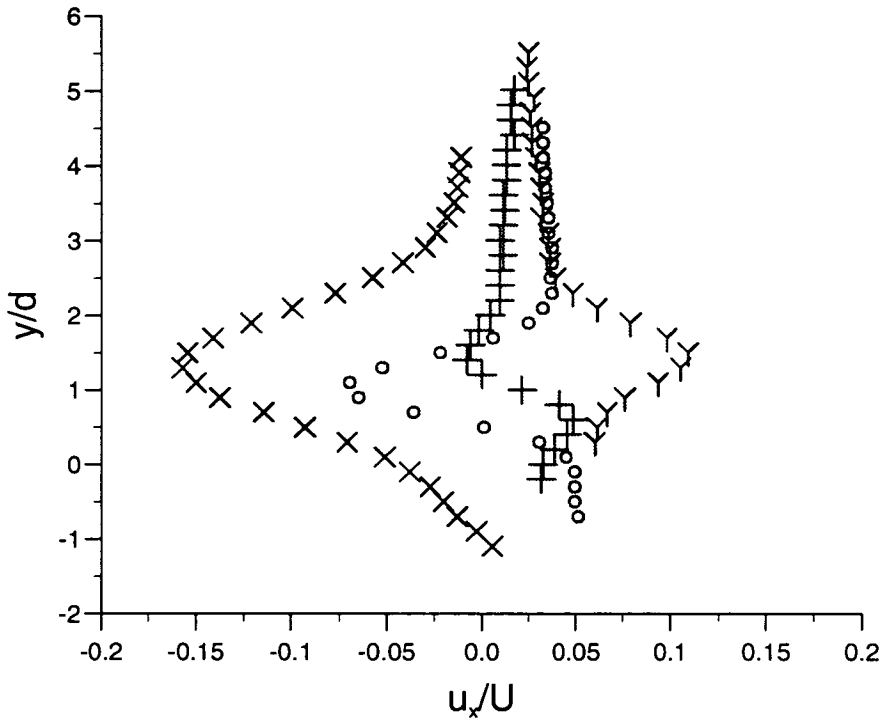

Figure 5.34: Mean Velocity Profiles, $Re = 100$: X, $S = 1.8$; O, $S = 2.4$; $+$, 3.5; Y, $S = 4.5$

parameter increases. As at $Re = 100$ there is a similar decrease in the distance of the maximum deficit from the centreline at $S = 2.4$ but at this Reynolds number the decrease is to a value of 0.1 d.

Wake Halfwidth

The variation of the wake halfwidth with spin parameter at both Reynolds number 100 and 200 is shown in Figure 5.38. This parameter remains approximately constant for $0.3 \leq S < 2.4$ at $Re = 100$ but decreases by approximately 50% at $S = 2.4$. However at $S = 4.5$, s_o increases again to the same level as at lower spin parameters. Although the profile at $S = 3.5$ is asymmetric, a value for the wake half width was estimated from the available data.

The behaviour at $Re = 200$ is slightly different since s_o decreases continuously over the range $0.3 \leq S \leq 2.4$. The value at $S = 2.4$ is approximately a fifth of the value at $S = 0.3$.

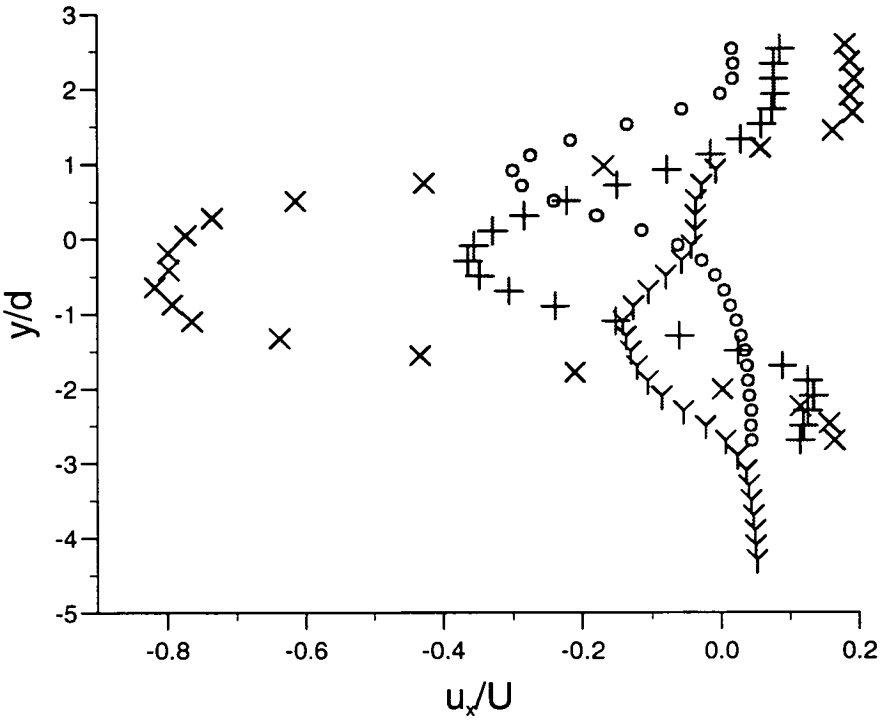

Figure 5.35: Mean Velocity Profiles, $Re = 200$: X, $S = 0$; Y, $S = 0.3$; $+$, $S = 0.5$; O, $S = 1.0$

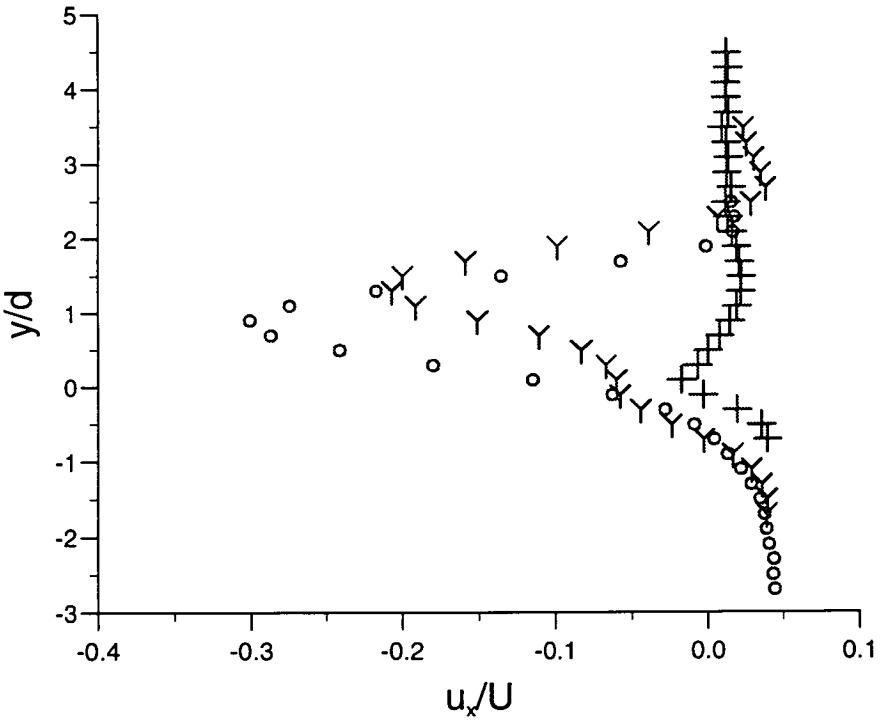

Figure 5.36: Mean Velocity Profiles, $Re = 200$: O, $S = 1.0$; Y, $S = 1.4$; $+$, $S = 2.4$

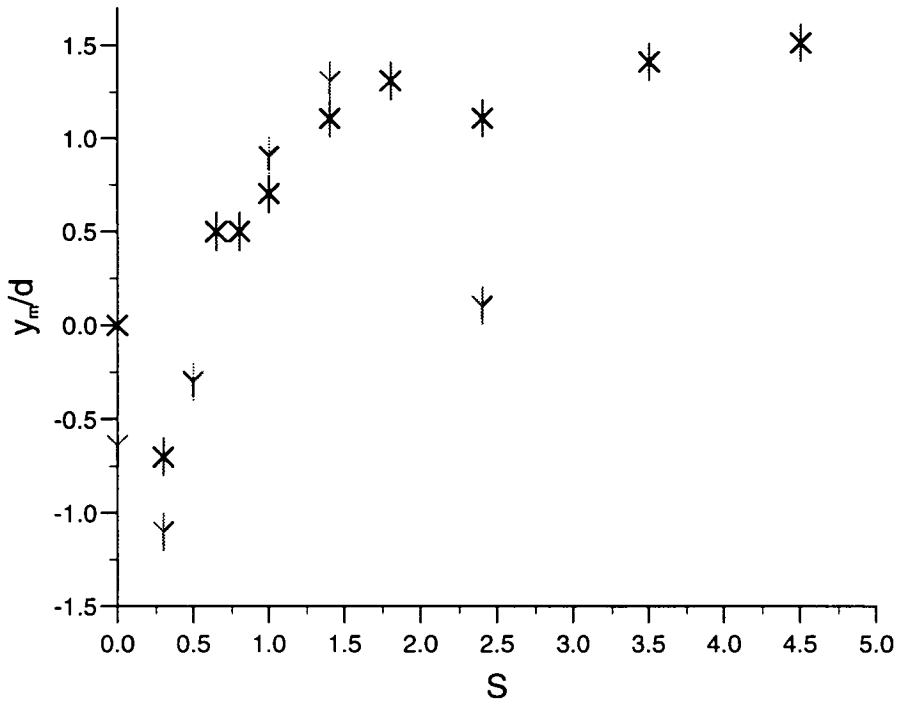

Figure 5.37: Variation of Position of Maximum Wake Velocity Deficit with Spin Parameter: X, $Re = 100$; Y, $Re = 200$

5.6 Discussion

5.6.1 Variation of Flow with Spin Parameter

Shedding Frequency Behaviour & synchronisation

It is clear from the previous section that the shedding from a rotating flat plate is different significantly from that behind a non-rotating plate. Perhaps the most noticeable difference is the changing appearance of the wake as the spin parameter is increased. Positive and negative vortices form pairs of varying regularity and combinations with the fusing of shed vortices to produce an amalgam which convects downstream. The combining of vortices as the rotation rate increases is intrinsically linked to the behaviour of the shedding frequency.

As illustrated by Figure 5.26, the variation of $2f_b/f_s$ with spin parameter is nominally linear for $0.3 \leq S \leq 1.4$ for both $Re = 100$ and 200 with deviations at $S = 0.5$. For $S > 1.4$ at $Re = 100$ the above quantity increases and deviates considerably from a value consistent with the previous linear behaviour. The deviation at $S = 0.5$ is significant since the value $2f_b/f_s$ jumps to is 2, that is the

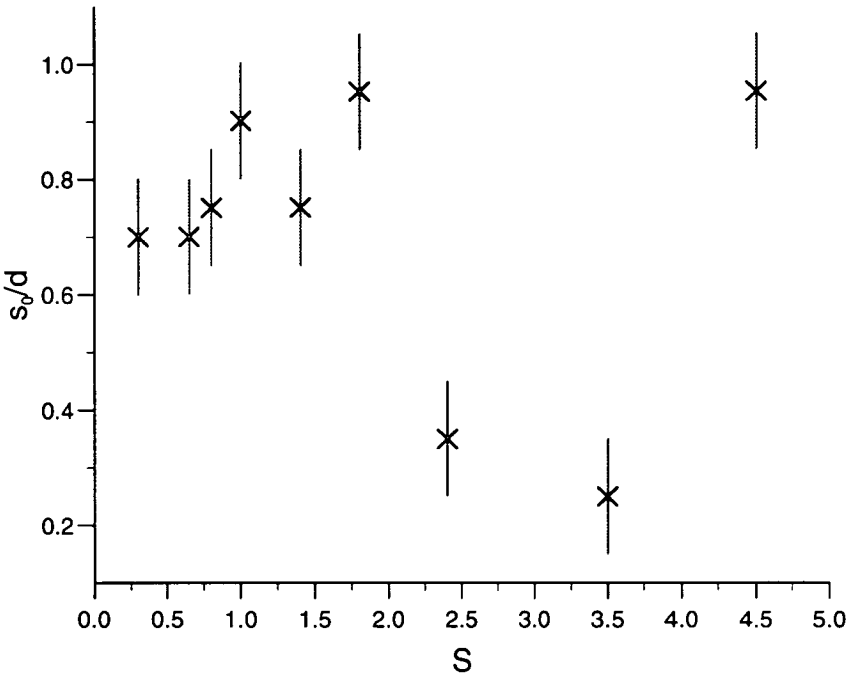

(a) $Re = 100$

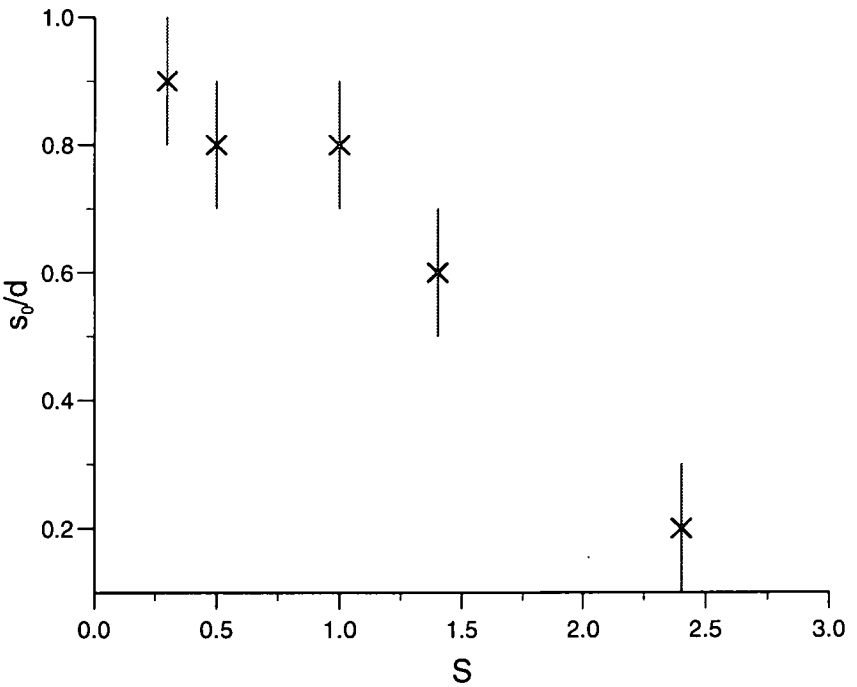

(b) $Re = 200$

Figure 5.38: Variation of Mean Profile Half Width with Spin Parameter

vortex shedding frequency is synchronised with that of the plate. Thus lock-in has occurred. However, as previously described, for $Re = 200$ the positions of the vortices are irregular and the vortex combination process is complex. A stronger case of lock-in occurs at $S = 0.3$ when a vortex pair is shed every half turn of the plate. Thus the shedding frequency is synchronised to half the plate frequency. For both Reynolds numbers the pair is very regular, with the downstream and cross-stream positions varying by only $\pm 0.2d$. For $Re = 100$ there is also synchronisation at $S = 0.65$. Although pairs are not formed, the vortices are very regular in position at each full turn.

As indicated by the linear nature of the above plots, for $S \leq 1.4$, when the shedding frequency is not locked in to the plate frequency it is constant. This is achieved by vortex combination. The vortices from the advancing edge (negative) are shed at constant frequency and the retreating edge, positive, vortices adjust by combining appropriately to give the vortex street. For example at $S = 1.4$ for $Re = 100$, the positive vortex which convects downstream is sometimes a combination of 4 shed vortices and at other times it is a combination of five. Thus overall, the shedding period is 4.5 plate half turns.

For $Re = 100$, when the spin parameter is increased above $S = 1.4$, the shedding frequency decreases. This is indicated by the increase in $2f_b/f_s$. The decrease in shedding frequency continues until the shedding ceases at $S \approx 2$ (Barnes, private communication). A decrease in shedding frequency also occurs at $Re = 200$.

A wake control experiment by Strykowski & Streenivasan [92] found that the shedding from behind a circular cylinder could be suppressed by placing a small, control cylinder into the wake. Although complete suppression could only be achieved for low Reynolds numbers, up to a maximum of $Re = 90$ in a water channel, the wakes at higher Reynolds numbers were nonetheless greatly affected by the presence of the control cylinder. Even if vortex shedding was not suppressed, the shedding frequency was reduced. Strykowski & Streenivasan noted that this decrease was consistent with Gerrard's [27] model of vortex street formation.

As discussed in Section 4.3.1, in Gerrard's model a vortex is shed when the shear layer from the opposite side of the body is drawn across the wake centreline and cuts off the circulation supply of the vortex. If the shear layers are weakened

sufficiently or prevented from interacting over a critical distance there is no vortex formation. However, if the shear layers are diffused or weakened, there is a reduced quantity of vorticity which can be drawn across the wake. Hence the time necessary for there to be a sufficient concentration of oppositely signed vorticity present to initiate shedding is increased and the shedding frequency is reduced.

Wake Geometry

The variation of the shedding wavelength with spin parameter should reflect the changes in the shedding frequency. Since $U_v = \lambda f_s$ where λ is the wavelength and U_v the convection velocity, then for a constant value of convection velocity and shedding frequency the wavelength should also be constant. Thus for $0.3 \leq S \leq 1.4$, except for where the frequency deviates from nominal linear behaviour, the wavelength should be constant. This deviation of the frequency occurs at $S = 0.5$ when the shedding and plate frequencies are locked in. The wavelength is found to be constant for $Re = 200$ and at $Re = 100$ for $0.65 < S \leq 1.4$. At $S = 1.8$ for $Re = 100$, the wavelength increases, the frequency decreases and U_v increases.

If the distance b/d is taken as a measure of the wake width and hence is considered to correspond to the same quantity in Section 4.2.2 then comparison shows that the wake behind a rotating plate is narrower than that behind a non-rotating one. For example, at $Re = 100$, a non-rotating plate has $b/d = 2.2$ whilst a rotating plate $b/d = 1.4$. Both values have an associated error of $\pm$ 0.2. This reduction in b/d is consistent with Strykowski & Streenivasan [92] who found that a controlled (suppressed) wake was narrower than an uncontrolled one.

Vortex Strengths

The results show that at both of the examined Reynolds numbers, the vortex strength is modified by the rotation of the plate. The strength decreases by approximately 20% as the spin parameter increases from zero, that is translation with no rotation, to a relatively slow rotation in which $S = 0.3$.

At $Re = 100$ both the positive and negative vortices undergo a steady decrease in strength as the spin parameter is increased from 0.3 to 1.8. At $S = 2.4$, the next spin parameter investigated, there are no vortex structures present. When the Reynolds number is increased to 200 there is again a decrease in strength with increased spin parameter.

There does not appear to be a significant asymmetry between the pair strengths as the spin parameter is increased. However, it was noted in the results that the positive vortices are consistently stronger than the negative ones at $Re = 100$ but the reverse is found at $Re = 200$. A possible explanation for this is as follows. With the anticlockwise rotation of these experiments it would be expected that based on the relative velocities of the plate tips that the vortex from the retreating edge (positive) would be weaker than the vortex from the advancing edge (negative). However, the rotation of the plate may impose a positive circulation on the flow and so increase the strength of the positive vortices. Since this would tend to be more effective when diffusion rather than convection is more influential within the wake, the inversion of the relative strengths would be more likely at low Reynolds numbers. Hence the positive vortices are stronger than the negatives at $Re = 100$ but not at $Re = 200$.

The decreasing trend for $Re = 200$ is not as smooth as that for $Re = 100$. It appears from Figure 5.29 that either the strength at $S = 1$ is lower than the trend would suggest or the strength at $S = 1.4$ is higher. To check that it was not the PIV analysis procedure which had led to the above effects, photographic frames from runs at both $S = 1$ and 1.4 were reanalysed. These produced the same vortex strengths as from previous analysis. Thus, further investigation of the vortex strengths as the spin parameter is increased above $S = 1$ is necessary to confirm this behaviour.

5.6.2 Variation of Mean Profiles with Spin Parameter

The changes in shedding behaviour which occur with an increasing spin parameter are reflected in the mean velocity profiles of the wake.

Wake Asymmetry

As the spin parameter is increased above $S \approx 0.7$, the position of the maximum wake deficit moves in the direction of rotation which in this case is anticlockwise. This implies that the wake becomes increasingly asymmetric. Such asymmetry is consistent with studies behind spinning cylinders for example those of Diaz *et al* [21, 22] and Sung *et al* [93] who found that the position of the maximum wake deficit moved in the direction of the rotation. Displacement of the profiles occurs due to the increasing difference in velocity between the upper and lower surfaces of the plate.

Wake Width

At spin parameters where there is vortex shedding, the wake width is dominated by the size and the presence of the vortices within the wake. Thus there is a clear change in the magnitude of this parameter, indicated here by the wake half width s_o (equation 5.38), when shedding has ceased. Although vortices are still present at $S = 2.4$ at $Re = 200$, they are longitudinally stretched and weaker than those formed at lower values of S. Therefore it is not inconsistent that s_o again should be lower at this spin parameter than at the preceding ones. The coincidence of a reduction in wake half width with the suppression of vortex shedding is consistent with the work of Diaz *et al* [22].

Diaz *et al* also found that for spin parameters at which vortex shedding was suppressed, the continued decrease in s_o with spin parameter was quasi-linear. Although for $Re = 100$, the half width at $S = 3.5$ is lower than that at $S = 2.4$, at the next spin parameter examined, 4.5, it sharply increases to a level comparable with one when shedding is present. However, as discussed below, the wake is very different at $S = 4.5$ and hence its behaviour is obviously different.

Velocity Deficit

The magnitude of the velocity deficit decreases as the spin parameter is increased. However, these decreases appear to occur in two stages, first as S increases from 0 to 0.3 and then, for $Re = 100$, when $S > 1.8$. For intermediate spin parameters there is little variation in the deficit magnitude. Since this magnitude is linked to the vortex strength, with the higher the strength the greater the deficit, these changes in deficit coincide with major decreases in the vortex strength. The results have shown that there is a decrease in the strength of shed vortices when the plate is first rotated and at $Re = 100$ for $S > 1.8$ when the shedding stops. Over the rest of the spin parameter range, the strength continually decreases. A significant change in the mean profiles occurs for $Re = 100$ at $S = 4.5$ when the wake deficit becomes positive. Thus at this spin parameter, the drag is negative and the profile has become that of a jet.

The generation of thrust behind a rotating body was noted by Lugt & Ohring [60] who performed numerical simulations of the flow past a rotating thin elliptic cylinder. They found that at $S = 2$ for $Re = 200$, the average drag became negative and a torque needed to be applied to the body to keep it rotating. Lugt & Ohring showed that this change in drag magnitude was due to a difference in

the vortex generation from the body's edges. This is summarised as follows and in Figure 5.39. For a flat plate rotating anti-clockwise at low spin parameters,

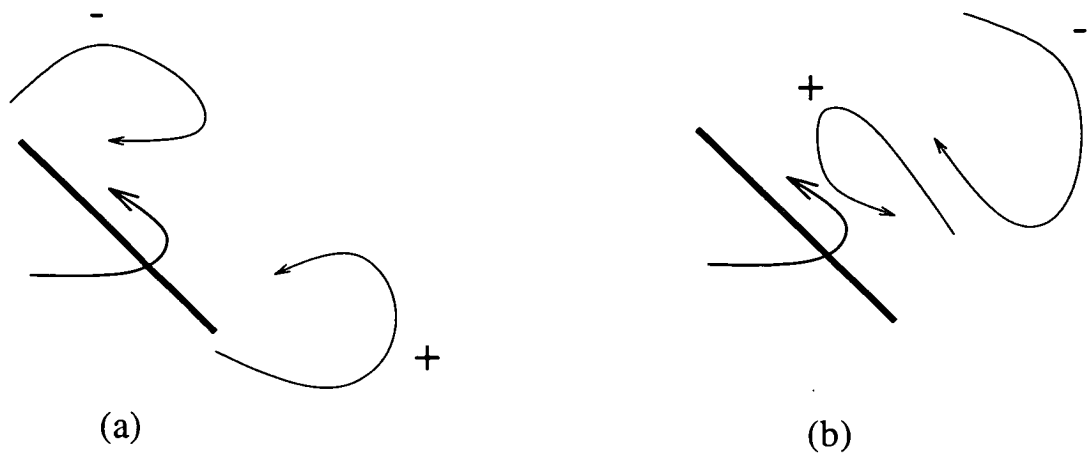

Figure 5.39: Changes in Shedding from a Flat Plate: (a), low S; (b), high S

negative and positive vortices are shed from the advancing and retreating edges respectively. At high spin parameters, the edges produce only clockwise, negative vorticity. However, a negative vortex can remain close to the plate and itself generate positive vorticity. Thus if the vortices are shed such that the relative positions in the wake are reversed, the mean profile has the form of a jet.

The generation of vorticity by the interaction of a vortex with a wall has been discussed by Doligalski *et al* [18]. Although concerned with boundary layers, Doligalski *et al* described how the presence of a vortex close to a surface could generate a region of reverse flow and hence an adverse pressure gradient. In a viscous fluid this could lead to separation and the production of a plume of vorticity erupting from the surface. Thus the presence of positive vorticity in the wake when the spin parameter is sufficiently high so that only negative vorticity would be expected can be explained by such a mechanism.

A reverse vortex street, rather than reverse vorticity bands of the present study, can be produced by oscillating an aerofoil. This was proposed by Von Karman & Burgess [47] and later found experimentally by, for example, Koochesfahani [53]. Again, such a street generates thrust. Examinations by Triantafyllou *et al* [102] have found that the maximum thrust efficiency occurs within a narrow Strouhal number range which is coincident with the range at which fish flap their fins.

5.6.3 Rotation as Wake Control

Although for $S \geq 2.4$ at $Re = 100$ coherent vortices are no longer present in the near wake, the bands of vorticity which form behind the plate have an internal structure. If vortex suppression as found by such studies as those of Strykowski & Streenisvan were occurring here, it might be expected that though there would be bands of vorticity, there would be no structure. The vorticity contours are weak but given that the absolute error on vorticity is $\pm 0.04 s^{-1}$ at this Reynolds number (from Figure 3.4.2), they can be considered as being above background. Even at $S = 4.5$, the higher contours in the bands remain above this noise level. Thus, there may be vortices still being produced by the interaction described by Doligalski *et al* [18] which between being formed, as shown by Lugt & Ohring [60], deform and interact in such a way as to form the vorticity bands found in the present study. As suggested by the flow visualisation at $S = 2.4$ for $Re = 200$, there may even have been roll up of these bands into vortices at larger downstream distances. Further investigation is necessary before any firm conclusions can be made about these observations. However, whatever the outcome of any further studies into larger wavelength structures at higher spin parameters, this investigation has shown that the primary von Karman street is eliminated at $S > 1.8$ for $Re = 100$. The results suggest also that at $S > 2.4$, the street at $Re = 200$ will also be suppressed.

The results of both Chen *et al* [12] and Coutanceau & Menard [15] for the wake from a rotating cylinder need to be discussed in the context of the present study. Coutanceau & Menard found that the vortex shedding at $Re = 200$ was suppressed at $S = 3.25$ whilst Chen *et al* continued to find a vortex shed in the studied time. However, Chen *et al* looked at flow up to a dimensionless time of 54. This corresponds to approximately 27 s in the present experiment and these results for $S \geq 2.4$ ($Re = 100$) and $S = 2.4$ ($Re = 200$) were taken at times typically greater than 50 s. It therefore is considered that Chen *et al*'s results could be a result of an insufficient runtime.

One of the comments of Chen *et al* on this major discrepancy between the two studies was that there may have been three-dimensionalities present at larger times in Coutanceau & Menard. Chen *et al* were unable to find any information regarding the effect of rotation on the transition of the wake from two to three dimensionality. A flow visualisation of the shedding within the bulk of the fluid at $Re = 200$ was performed to investigate the dimensional nature of the shedding

from the rotating plate. It was found that the shedding was parallel to the plate within the field of view of the CCD camera ($0 \leq x/d \leq 40$). This is contrary to the shedding from a purely translating plate (refer to Section 4.5) which displays three-dimensional modes at $Re = 200$. Thus rotating the plate stabilises the shedding to three-dimensional effects.

As discussed in Section 1.3, wake control is generally exerted by suppressing or interfering with the absolute instability of the wake. Since rotating the plate leads to the elimination of the primary vortex street, a possible explanation for this behaviour is that the rotation interferes with these instability modes. A stability analysis of the near wake behind a rotating flat plate therefore would be of interest to investigate the presence or absence of such modes for $S > 2$.

5.7 Conclusion

This chapter has shown that the wake behind a translating flat plate is significantly modified by simultaneous rotation. At both $Re = 100$ and 200, the shedding frequency synchronises to the plate frequency at spin parameters of 0.3 and 0.5. This lock-in is consistent with the numerical predictions of Lugt [59] and is particularly strong at $S = 0.3$. For $S \leq 1.4$, the shedding frequency is constant and the Strouhal number is higher than that for a non-rotating plate. However, once the spin parameter is further increased, the shedding frequency reduces significantly. For $Re = 100$, the primary vortex street is eliminated for $1.8 \leq S \leq 2.4$ and for $Re = 200$, the wake is different at $S = 2.4$, which was the highest spin parameter investigated. The strength of the vortices decreases with increasing spin parameter, and the strength at the lowest rotation rate is lower than that for a non-rotating plate. There does not appear to be a asymmetry between the strengths of the positive and negative vortices.

The behaviour of the mean velocity profiles also changes as the the spin parameter is increased. The magnitude of the velocity defect is reduced at both Reynolds numbers, with a significant difference between the non-rotating and rotating states. For $Re = 100$ at $S = 4.5$, the velocity defect becomes positive and the mean profile has the form of a jet. The last observation confirms the prediction made by Lugt & Ohring [60] that a jet would form behind a rotating elliptic cylinder.

Chapter 6

Conclusions & Future Work

6.1 Conclusions

6.1.1 Experimental & Analysis Techniques

Surface PIV

Surface PIV has be shown to be a very effective method of studying near wake flows. A combination of two flashguns, a delay box and a camera are sufficient to produce, with suitable analysis, velocity maps of the flow field. The error associated with a velocity vector on such a map is of the order of 1%.

Vortex Strength

The quantity vortex strength has been used extensively throughout this study. This was calculated by transforming a velocity to a vorticity field and then summing the vorticity over a given area. If a vortex were surrounded by zero vorticity this summation would be straightforward as all vorticity could be included. However, this is not possible in a wake flow since there is a background vorticity level. Consequently, it is necessary to define a vortex boundary. Different definitions of vortex boundary have been discussed and the method chosen for use in this study was, for a given vortex, to sum the vorticity within the vortex down to and including those values which were 10% of the maximum. The variation of vortex strength with percentage of the maximum vorticity chosen as the summation boundary has been found to be linear. The 10% boundary gives a value which is 90% of the total strength. This result is the same as that for an Oseen vortex. The associated error varies from 4% to 9% depending on the Reynolds number of the flow.

Circulation

The circulation of a vortex is equal to its vortex strength for the same boundary and is calculated by summing the velocities around a defined circuit. Since it is calculated from a velocity field, circulation has a lower inherent error and for the systems studied here this error has been calculated to be 2 - 3%. Again, defining the boundary is a difficult problem. Rectangular boundaries were used in the present work and these gave values of circulation which matched those of strength to within approximately 5%. However, due to the simpler, more flexible, method vortex strength was generally used in preference to circulation in this study.

6.1.2 Vortex Shedding from Bodies in Uniform Flow

Two-Dimensional Regime

The vortex shedding from a translating circular cylinder and a flat plate with its axis normal to the free-stream has been investigated for Reynolds numbers between 80 and 150. The principal conclusion of this study is that, for both bodies, the variation of vortex strength with Reynolds number is continuous. This is in contrast to the study of Green & Gerrard [37] who found, for a circular cylinder, a discontinuity at a Reynolds number of approximately 100. However, the present result is consistent with the the variation of both the Strouhal number and base suction coefficient with Reynolds number which are continuous. The vortex strength values of the present study also match those of Henderson [42] to within experimental error.

The shedding behaviour of the flat plate follows the same trends as the circular cylinder. However, the increased separation velocity at the edges slightly modifies this behaviour. For example, the strengths of vortices shed from the plate are approximately 20% higher than those from the circular cylinder.

Experimental vorticity profiles were fitted to those of an Oseen vortex to examine the validity of using such a model in wake studies. For a given vortex, the vorticity distributions in the x and y directions are different but both give good fits with their respective theoretical profiles. The vortex strengths yielded by this modelling are different in the x and y directions. In general, one of these strengths matched the value found by the vorticity summation method.

Vorticity plots have shown that the vortices shed from both a flat plate and a circular cylinder are elliptical in the region $3.4 \leq x/d \leq 11.4$. The asymmetry of the vorticity profiles is consistent with this vortex shape. It is suggested that it was their assumption of the vortices possessing circular symmetry which led Green & Gerrard to find a discontinuous variation of vortex strength with Reynolds number.

Three-Dimensional Transitional Regime

Flow visualisation and PIV have been used to illustrate the flow behaviour at Reynolds numbers of 180 for both bodies and 230 and 215 for the flat plate and circular cylinder respectively. Flow visualisation at Reynolds numbers of 180 and 235 show that the vortices penetrate the water surface normally, thus enforcing two-dimensionality at the surface. These visualisations also indicate that three-dimensional shedding modes (A and B) are present in the flow. The PIV results for wake quantities such as vortex strength and wavelength , are consistent with those at lower Reynolds numbers.

6.1.3 Wake behind a Rotating Flat Plate

It has been shown in this study that the wake behind a flat plate rotating about its axis is distinctly modified by the rotation. For both Reynolds numbers 100 and 200 the basic behaviour is the same, thus the overall trends are Reynolds number independent.

Frequency Lock-in

Synchronisation of the vortex shedding frequency and the plate rotational frequency occurs at $S = 0.3$ and 0.5. The frequencies are also locked-in at $S = 0.65$ for $Re = 100$. This spin parameter was not investigated for $Re = 200$. At spin parameters 0.3 and 0.65, the vorticity plots are very regular, whilst there is relatively more variation in vortex positions at $S = 0.5$.

Shedding Frequency Reduction

For spin parameters between 0.2 and 1.4 the variation of $2f_b/f_s$ with S is linear with the only exception being at lock-in at $S = 0.5$. Hence the shedding frequency is constant for this range. For $Re = 100$, as the spin parameter is further increased, the shedding frequency decreases. This is consistent with Barnes [6] who found that the shedding frequency decreased above $S = 1.4$ for both

$Re = 100$ and 200 until the shedding stopped at $S \approx 2$.

Within the constant shedding frequency region only the vortices shed from the advancing edge are shed at constant frequency, those shed from the retreating edge adjust their frequency by combining.

Vortex Strength Decrease

Rotation decreased the vortex strength. The difference between the normalised strength of a vortex from a non-rotating plate and one which was rotating with $S = 0.3$ was approximately 20%. The vortex strength continued to decrease as the spin parameter was further increased. There did not seem to be a significant asymmetry between the positive and negative vortices as the spin parameter increased.

Vortex Suppression

At $Re = 100$ the von Karman vortex street is suppressed at $S = 2.4$. Coherent vortices are no longer present in the wake. When the Reynolds number is increased to 200, the street is not completely suppressed at this spin parameter. However, the wake behaviour suggests that suppression is possible at a slightly higher spin parameter than is possible with the present system.

For $Re = 100$, there are vorticity bands at $S = 2.4$ which indicate the presence of some internal structure. This has been discussed within the context of vorticity eruptions (Doligalski *et al* [18]). When the spin parameter is increased to 4.5, the orientation of the vorticity bands in the wake changes; the positive and negative bands reverse.

Mean Velocity Profiles

The velocity deficit decreases with increasing rotation. The position of the maximum mean velocity moves in the direction of the rotation as the spin parameter is increased. An exception is at $S = 0.3$ when the locked-in pairs move below the wake centreline. At $S = 4.5$ for $Re = 100$, the sense of the velocity deficit becomes positive and the mean profile has the form of a jet. This is consistent with the spatial reversal of the positive and negative vorticities.

6.2 Future Work

6.2.1 Techniques & Data Analysis

The present PIV system does not allow visualisation of the bluff body wake between $0 \leq x/d \leq 3.4$. This region is critical in the vortex shedding process. If the carriage were modified, this important area could be photographed.

Possible improvements could be made if a more advanced form of PIV, digital PIV, were used. Gray [32] captures multiple images using a digital camera and mathematically performs the autocorrelation process. This has many advantages over traditional PIV since on-line imaging is possible and Young's fringe analysis system problems, such as minimum particle separation, can be avoided. In the present study the magnification of the photograph had to be chosen such that the velocity vectors within the vortices were resolvable. If a digital system were used, the autocorrelation could be performed regardless of the velocity gradients across the image. Thus there would fewer constraints on the field of view. DPIV also has the advantage that data taking and the analysis process are less time consuming than the present technique.

Improving the circulation calculation would be advantageous since the inherent error is less than that of the integrated vortex strength. This would involve developing a program to sum the velocities around a circuit which closely matched the vortex shape. However, the problem of defining a vortex boundary would still need to be addressed.

6.2.2 Near Wake Development

To date, there are few studies of the shedding from a bluff body itself which show the level of detail given by the technique used in the present investigation. For example, the DPIV of Gharib [29] does not clearly illustrate the features of the vortices shedding from a circular cylinder. Thus extending the work of the translating flat plate and circular cylinder into the region $0 \leq x/d \leq 3.4$ could provide further information about near wake dynamics.

6.2.3 Wake Modification & Control by Rotation

As discussed in Chapter 5, there is a considerable amount of further work which could be performed for this study. Data capture in the region $0 \leq x/d \leq 5.4$ would enable the shedding vorticity and developing vortices to be studied. This

would be particularly useful for spin parameters larger than 2 when flow visualisations and PIV indicate the suppression of the primary vortex street.

The data produced at smaller x/d could be used in stability analysis calculations. As mentioned previously, vortex street suppression and general wake control is achieved by interfering with the absolute instability of the wake. Hence it would be of interest to see if rotating a body about its axis affected one of these instability modes.

The present results suggest that there may be longer wavelength vorticity structures present in the wake after the von Karman vortex street has been eliminated. Hence PIV studies at larger downstream distances for $S > 2$ would help to provide more information about wake behaviour at these spin parameters.

Extending the Reynolds number 200 work to cover more spin parameters would allow investigation of the decreasing frequency region. Modification of the rotation system would enable the flow to be studied at higher spin parameters than $S = 2.4$. Hence it could be seen if there was jet formation as at $Re = 100$.

Although the present study found that, for $Re = 200$, the vortex strength decreased for $0.3 \leq S \leq 2.4$, the trend at $S = 1$ and 1.4 was not so well defined with $K(1.4)/\pi Ud > K(1)/\pi Ud$. Thus the strengths above $S = 1$ need to be reinvestigated to try to clarify the strength behaviour in this region.

Bibliography

[1] G. Arakaki. The growth and development of the wake behind inclined flat plates at low Reynold number. *Journal of Science of Hiroshima University*, A2; 32(9):191, 1968.

[2] B.J. Armstrong, F.H. Barnes, and I. Grant. A comparison of the structure of the wake behind a circular cylinder in a steady flow with that in a perturbed flow. *Physics of Fluids*, 30(1):19–26, 1987.

[3] H.M. Badr, M. Coutanceau, S.C.R. Dennis, and C. Menard. Unsteady flow past a rotating circular cylinder at Reynolds number 10^3 and 10^4. *Journal of Fluid Mechanics*, 220:459–484, 1990.

[4] H.M. Badr and S.C.R. Dennis. Time-dependent viscous flow past an impulsively started rotating and translating circular cylinder. *Journal of Fluid Mechanics*, 158:447–488, 1985.

[5] D. Barkley and R.D. Henderson. Three-dimensional Floquet stability analysis of the wake of a circular cylinder. *Journal of Fluid Mechanics*, 319:1–27, 1996.

[6] F.H. Barnes. A flow visualisation study of autorotation. Unpublished.

[7] P. W. Bearman. Vortex shedding from oscillating bluff bodies. *Annual Reviewof Fluid Mechanics*, 16:195–222, 1984.

[8] W. Berger and R. Wille. Periodic flow phenomena. *Annual Review of Fluid Mechanics*, 4:313–340, 1972.

[9] M.S. Bloor and J.H. Gerrard. Measurements on turbulent vortices in a cylinder wake. *Proceedings of the Royal Society of London: Series A*, 294:319–342, 1966.

[10] M. Brede, H. Eckelmann, and D. Rockwell. On secondary vortices in the cylinder wake. *Physics of Fluids*, 8(8):2113–2124, 1996.

[11] R. Chein and J. N. Chung. Discrete-vortex simulation of flow over inclined and normal flat plates. *Computers and Fluids*, 16:405–427, 1988.

[12] Y.-M. Chen, Y.-R. Ou, and A.J. Pearlstein. Development of the wake behind a circular cylinder impulsively started into rotatory and rectilinear motion. *Journal of Fluid Mechanics*, 253:449–484, 1993.

[13] Y.T. Chew, M. Cheng, and S.C. Luo. A numerical study of flow past a rotating circular cylinder using a hybrid vortex scheme. *Journal of Fluid Mechanics*, 299:35–71, 1995.

[14] M. Coutanceau and R. Bouard. Experimental determination of the main features of the viscous flow in the wake of a circular cylinder in uniform translation. Part 1. Steady flow. *Journal of Fluid Mechanics*, 79:231–256, 1977.

[15] M. Coutanceau and C. Menard. Influence of rotation on near-wake development behind impulsively started circular cylinder. *Journal of Fluid Mechanics*, 158:399–446, 1985.

[16] M.E. Davies. Wake structure of a stationary and oscillating body. *Journal of Fluid Mechanics*, 75:209–231, 1975.

[17] S. C. R. Dennis, W. Qiang, M. Coutanceau, and J.-L. Launay. Viscous flow normal to a flat plate. *Journal of Fluid Mechanics*, 248:605–635, 1993.

[18] T.L. Doligalski, C.R. Smith, and J.D.A. Walker. Vortex interactions with walls. *Annual Review of Fluid Mechanics*, pages 573–616, 1994.

[19] H. Eisenlohr and H. Eckelmann. Vortex splitting and its consequence in the vortex street wake of cylinders at low Reynolds number. *Physics of Fluids*, A1:189–192, 1989.

[20] A. Fage and F.C. Johansen. On the air flow behind an inclined flat plate of infinite span. *Proceedings of the Royal Society of London*, 116:170–197, 1927.

[21] F.Diaz, J. Gavalda, J.G. Kawall, and F. Giralt. Vortex shedding from a spinning cylinder. *Physics of Fluids*, 26(12):3454–3460, 1983.

[22] F.Diaz, J. Gavalda, J.G. Kawall, and F. Giralt. Asymmetrical wake generated by a spinning cylinder. *AIAA Journal*, 23(1):49–54, 1985.

[23] J.R. Filler, P.L. Marston, and W.C. Mih. Response of the shear layers separating from a circular cylinder to small amplitude rotational oscillations. *Journal of Fluid Mechanics*, 231:481–499, 1991.

[24] B. Fornburg. Steady viscous flow past a circular cylinder upto Reynolds number 600. *Journal of Computational Physics*, 61:297–320, 1985.

[25] P. Freymuth, F. Finaish, and W. Bank. Visualization of the vortex street behind a circular cylinder at low Reynolds numbers. *Physics of Fluids*, 29(4):1321–1323, 1986.

[26] M. Gaster. Vortex shedding from circular cylinders at low Reynolds numbers. *Journal of Fluid Mechanics*, 46:749–756, 1971.

[27] J. H. Gerrard. The mechanics of the vortex formation region of vortices behind bluff bodies. *Journal of Fluid Mechanics*, 25:401–413, 1966.

[28] J. H. Gerrard. The wakes of cylinderical bluff bodies at low Reynolds number. *Philosophical Transactions of the Royal Society of London*, 288:351–382, 1978.

[29] M. Gharib. The experimentalist in the age of supercomputers. In *Proceedings of the ASME/JSME Fluids Engineering Division Summer Meeting*, 1995.

[30] M.L. Grant. The large eddies of turbulent motion. *Journal of Fluid Mechanics*, 4:149–190, 1958.

[31] C. Gray. *The Development of Particle Image Velocimetry for Water Wave Studies.* PhD thesis, University of Edinburgh, 1989.

[32] C. Gray. VidPIV for Microsoft Windows - Analysis tools for Particle Image Velocimetry, 1994.

[33] C. Gray and C. A. Greated. The application of Particle Image Velocimetry to measurement under water waves. *Optics and Lasers in Engineering*, 9:265–276, 1988.

[34] C. Gray, C. A. Greated, W. J. Easson, and N. E. Fancey. Application of particle image velocimetry to measurement under waves. In *Proceedings of Second International Conference on Laser Anemometry*, 1987.

[35] C. Gray, C. A. Greated, D. R. McCluskey, and W. J. Easson. An analysis of the scanning beam PIV illumination system. *Measurement Science and Technology*, 2:714–724, 1991.

[36] R. B Green. *Measurement of vorticity and vortex strength in the wake of a circular cylinder at low Reynolds number.* PhD thesis, University of Manchester, 1989.

[37] R. B. Green and J. H. Gerrard. An optical interferometric study of the wake of a bluff body. *Journal of Fluid Mechanics*, 226:219–242, 1991.

[38] R. B. Green and J. H. Gerrard. Vorticity measurements in the near wake of a circular cylinder at low Reynolds numbers. *Journal of Fluid Mechanics*, 246:675–691, 1993.

[39] O. M. Griffen. A note on bluff body vortex formation. *Journal of Fluid Mechanics*, 284:217–224, 1995.

[40] O. M. Griffen and M. Hall. Vortex shedding and lock-on and flow control in bluff body wakes. *Journal of Fluids Engineering*, 113:526–537, 1991.

[41] F.R. Hama. Three-dimensional vortex pattern behind a circular cylinder. *Journal of Aeronautical Sciences*, 24:156, 1957.

[42] R. D Henderson. *Unstructured spectral element methods: Parallel algorithms and simulations.* PhD thesis, Princeton University, 1994.

[43] R. D. Henderson and D. Barkley. Secondary instability in the wake of a circular cylinder. *Physics of Fluids*, 8(6):1683–1685, 1996.

[44] X. Y. Huang. Feedback control of vortex shedding from a circular cylinder. *Experiments in Fluids*, 20(3):218–224, 1996.

[45] J. D. Hudson and S. C. R. Dennis. Flow of a viscous incompressible fluid past a normal flat plate at low and intermediate Reynolds numbers : the wake. *Journal of Fluid Mechanics*, 160:369–383, 1985.

[46] D. S Joshi. *Numerical studies of the wake of a plate normal to a free stream.* PhD thesis, University of Illinois at Urbana-Champaign, 1993.

[47] T. Von Karman and J.M. Burgers. General aerodynamic theory - Perfect fluids. In W.F. Durand (1935), editor, *Aerodynamic Theory*, page 308. Peter Smith Publishers, 1976.

[48] G.E. Karniadakis and G.S. Triantafyllou. Frequency selection and asymptotic states in laminar wakes. *Journal of Fluid Mechanics*, 199:441–469, 1989.

[49] R. D. Keane and R. J. Adrian. Optimisation of particle image velocimeters. part 1 : Double pulsed systems. *Measurement in Science and Technology*, 1:1202–1215, 1990.

[50] R. D. Keane and R. J. Adrian. Optimisation of particle image velocimeters. part 2 : Multiple pulsed systems. *Measurement in Science and Technology*, 2:963–974, 1991.

[51] M. Kiya and M Matsumura. Incoherent turbulence structure in the near wake of a normal plate. *Journal of Fluid Mechanics*, 190:343–356, 1988.

[52] M. Koenig, B.R. Noack, and H. Eckelmann. Discrete shedding modes in the von Karman vortex street. *Physics of Fluids*, A5:1846–1848, 1993.

[53] M.M. Koochesfahani. Vortical patterns in the wake of an oscillating aerofoil. *AIAA Journal*, 27(9):1200–1205, 1989.

[54] K. Kwon and H. Choi. Control of laminar vortex shedding behind a circular cylinder using splitter plates. *Physics of Fluids*, 8(2):479–486, 1996.

[55] J. C. Lecordier, L. Hamma, and P. Paranthoen. The control of vortex shedding behind heated cylinders at low Reynolds numbers. *Experiments in Fluids*, 10:224–229, 1991.

[56] J.-C. Lin, J. Towfighi, and D. Rockwell. Near-wake of a circular cylinder: Control by steady and unsteady surface injection. *Journal of Fluids and Structures*, 9:659–669, 1995.

[57] D Lisoski. *Nominally two-dimensional flow about a normal flat plate.* PhD thesis, California Institute of Technology, 1993.

[58] L. Lourenco and A. Krothpalli. On the accuracy of velocity and vorticity measurements with PIV. *Experiments in Fluids*, 18:421–428, 1995.

[59] H.J. Lugt. Autorotation of an elliptic cylinder about an axis perpendicular to the flow. *Journal of Fluid Mechanics*, 99:817–840, 1980.

[60] H.J. Lugt and S. Ohring. Rotating elliptic cylinders in a viscous fluid at rest or in a parallel stream. *Journal of Fluid Mechanics*, 79:127–156, 1977.

[61] G.D. Miller and C.H.K. Williamson. Control of three-dimensional phase dynamics in a cylinder wake. *Experiments in Fluids*, 18:26–35, 1994.

[62] T. Miyagi. Standing vortex pair behind a flat plate normal to uniform flow of viscous fluid. *Journal of Physical Society of Japan*, 45(5):1751–1755, 1978.

[63] P. A. Monkewitz. Feedback control of global oscillations in fluid systems. Technical Report 89-0991, AIAA, 1989.

[64] P. A. Monkewitz. Wake control. In H. Eckelmann, J. M. R. Graham, P. Huerre, and P. A. Monkewitz, editors, *Bluff-Body Wakes, Dynamics and Instabilities*, pages 227–240. Springer-Verlag, 1993.

[65] P. A. Monkewitz and L. N. Nguyen. Absolute instability in the near wake of two-dimensional bluff bodies. *Journal of Fluids and Structures*, 1:165–184, 1987.

[66] M. V. Morkovin. Flow around a circular cylinder - kaleidoscope of challenging fluid phenomena. In *Proceedings of ASME Symposium on Separated Flows*, 1964.

[67] I. G. Morrison. *The hydrodynamic performance of an oscillating water column wave energy converter.* PhD thesis, University of Edinburgh, 1995.

[68] F. M. Najjar and S. P. Vanka. Simulations of the unsteady separated flow past a normal flat plate. *International Journal for Numerical Methods in Fluids*, 21:525–547, 1995.

[69] M. Nakano and D. Rockwell. Wake from a cylinder subjected to amplitude-modulated excitation. *Journal of Fluid Mechanics*, 247:79–110, 1993.

[70] M. Nakano and D. Rockwell. Flow structure in the frquency-modulated wake of a cylinder. *Journal of Fluid Mechanics*, 266:93–119, 1994.

[71] J.M. Nguyen Duc and J. Sommeria. Experimental characterisation of steady two dimensional couples. *Journal of Fluid Mechanics*, 192:175–192, 1988.

[72] B.N. Noack, F. Ohle, and H. Eckelmann. On cell formation in vortex streets. *Journal of Fluid Mechanics*, 227:293–308, 1991.

[73] H. Oertel. Wakes behind blunt bodies. *Annual Review of Fluid Mechanics*, 22:539–564, 1990.

[74] D. S. Park, D.M Ladd, and E.W. Hendricks. Feedback control of von Karman vortex shedding behind a circular cylinder at low Reynolds number. *Physics of Fluids*, 6(7):2391–2405, 1994.

[75] A. E. Perry, M. S. Chong, and T. T. Lim. The vortex shedding process behind two-dimensional bluff bodies. *Journal of Fluid Mechanics*, 116:77–90, 1982.

[76] A.E. Perry and T.R. Steiner. Large-scale vortex structures in turbulent wakes behind bluff bodies. Part 1. Vortex formation processes. *Journal of Fluid Mechanics*, 174:233–270, 1987.

[77] A. Prasad and C. H. K. Williamson. The instability of the separated shear layer from a bluff body. *Physics of Fluids*, 8(6):1347–1349, 1996.

[78] M. Provansal, C. Mathis, and L. Boyer. Benard-von Karman instability: transient and forced regimes. *Journal of Fluid Mechanics*, 182:1–22, 1987.

[79] P. A. Quinn, D. J. Skyner, C. A. Greated, and W. J. Easson. A critical analysis of the Particle Image Velocimetry technique as applied to water waves. In *Proceedings of Euromech. 279 Colloquium*, 1991.

[80] A. Roshko. On the development of turbulent wakes from vortex streets. Technical Report 1191, Rep. Nat. Adv. Com. Aero., Washington, 1954.

[81] A. Roshko. On the wake and drag of bluff bodies. *Journal of Aeronautical Science*, 22:124–132, 1955.

[82] K. Roussopoulis. Feedback control of vortex shedding at low Reynolds numbers. *Journal of Fluid Mechanics*, 248:267–296, 1993.

[83] T. Sarpkaya. An inviscid model of two-dimensional vortex shedding for transient and asymptotically steady separated flow over an inclined plate. *Journal of Fluid Mechanics*, 68:109–128, 1975.

[84] J.W. Schaefer and S. Eskinazi. An analysis of the vortex street generated in a viscous fluid. *Journal of Fluid Mechanics*, 6:241–260, 1958.

[85] G. Schewe. On the force fluctuations acting on a circular cylinder in cross-flow from subcritical up to transcritical Reynolds numbers. *Journal of Fluid Mechanics*, 133:265–285, 1983.

[86] L. Schiller and W. Linke. Druck und reibungswiderstand des zylinders bei Reynoldsaachen zahlen 5,000 bis 40,000. *Z. flugtech. Motorluft*, 24:193, 1933.

[87] M. Schumm, E. Berger, and P. A. Monkewitz. Self-excited oscillations in the wake of two-dimensional bluff bodies and their control. *Journal of Fluid Mechanics*, 271:17–53, 1994.

[88] S. K. Sinha. Improving the accuracy and resolution of particle image or laser speckle velocimetry. *Experiments in Fluids*, 6:67–68, 1988.

[89] D. J. Skyner. *The mechanics of extreme water waves.* PhD thesis, University of Edinburgh, 1992.

[90] A. Slaouti and J.H. Gerrard. An experimental investigation of the end effects on the wake of a circular cylinder towed through water at low Reynolds numbers. *Journal of Fluid Mechanics*, 112:297–314, 1981.

[91] V. Strouhal. Uber eine besondered art der tonerregung. *Ann. Phys. und Chemie.*, 10:216, 1878.

[92] P. J. Strykowski and K. R. Sreenivasan. On the formation and suppression of vortex shedding at low Reynolds numbers. *Journal of Fluid Mechanics*, 218:71–107, 1990.

[93] H.J. Sung, C.K. Chun, and J.M. Hyun. Experimental study of uniform-shear flow past a rotating cylinder. *Journal of Fluids Engineering*, 117:62–67, 1995.

[94] H. R. Tamaddon-Jahromi, P; Townsend, and M. F. Webster. Unsteady viscous flow past a flat plate orthogonal to the flow. *Computers Fluids*, 23:433–446, 1994.

[95] S. Taneda. Experimental investigation of the wakes behind circular cylinders and plates at low Reynolds numbers. *Journal of the Physical Society of Japan*, 11:302, 1956.

[96] S Taneda. Standing twin-vortices behind a thin flat plate normal to the flow. *Rep. Res. Inst. Appl. Mech. Kyushu Univ.*, 16(54):155, 1968.

[97] S. Taneda and H. Honji. Unsteady flow past a flat plate normal to the direction of motion. *Journal of the Physical Society of Japan*, 30:262–272, 1971.

[98] M. Thompson, K. Hourigan, and J. Sheridan. Three-dimensional instabilities in the wake of a circular cylinder. *Experimental Thermal and Fluid Science*, 12:190–196, 1996.

[99] A. Timme. On the velocity distribution in vortices. *Ing. Arch.*, 25:205, 1957.

[100] P. T. Tokumaru and P. E. Dimotakis. Rotary oscillatory control of a cylinder wake. *Journal of Fluid Mechanics*, 224:77–90, 1991.

[101] G.S. Triantafyllou, M.S. Triantafyllou, and C. Chryssostomidis. On the formation of vortex streets behind stationary cylinders. *Journal of Fluid Mechanics*, 170:461–477, 1986.

[102] M.S. Triantafyllou, G.S. Triantafyllou, and R. Gopalkrishnan. Wake mechanics for thrust generation in oscillating foils. *Physics of Fluids*, A3(12):2835–2837, 1991.

[103] D.J. Tritton. Experiments on the flow past a circular cylinder at low Reynolds numbers. *Journal of Fluid Mechanics*, 6:547–567, 1959.

[104] M. F. Unal and D. Rockwell. On vortex shedding from a cylinder: Part 1. the initial instability. *Journal of Fluid Mechanics*, 190:491–512, 1988.

[105] M. F. Unal and D. Rockwell. On vortex shedding from a cylinder: Part 2. Control by splitter plate interference. *Journal of Fluid Mechanics*, 190:513–529, 1988.

[106] C. H. K. Williamson. Defining a universal and continuous Strouhal-Reynolds number relationship for the laminar vortex shedding of a circular cylinder. *Physics of Fluids*, 31(10):2742–2744, 1988.

[107] C. H. K. Williamson. Oblique and parallel modes of vortex shedding in the wake of a circular cylinder at low Reynolds numbers. *Journal of Fluid Mechanics*, 206:579–627, 1989.

[108] C. H. K. Williamson. The natural and forced formation of spot-like 'vortex dislocations' in the transition of a wake. *Journal of Fluid Mechanics*, 243:303–441, 1992.

[109] C. H. K. Williamson. Vortex dynamics in the wake of a cylinder. In S. I. Green, editor, *Fluid Vortices*, pages 155–234. Kluwer Academic Publishers, 1995.

[110] C. H. K. Williamson. Vortex dynamics in the cylinder wake. *Annual Review of Fluid Mechanics*, 28:477–539, 1996.

[111] C. H. K. Williamson and A. Roshko. Measurements of base pressure in the wake of a cylinder at low Reynolds number. *Zeitschrift fur Flugwissenschaften und Weltraumforschung*, 14:38–46, 1990.

[112] J. Wu, J. Sheridan, J. Soria, and M.C. Welsh. An experimental investigation of streamwise vortices in the wake of a bluff body. *Journal of Fluids and Structures*, 8:621–625, 1994.

[113] J. Wu, J. Sheridan, M.C. Welsh, and K. Hourigan. Three-dimensional vortex structures in a cylinder wake. *Journal of Fluid Mechanics*, 312:201–222, 1996.

[114] Y. Yoshida and T. Nomura. A transient solution method for the finite elementa incompressible Navier Stokes equations. *International Journal for Numerical Methods in Fluids*, 5:873–890, 1985.

[115] M. H. Yu and P. A. Monkewitz. The effect of nonuniform density on the absolute instability of two-dimensional inertial jets and wakes. *Physics of Fluids*, A2:1175–1181, 1990.

[116] H.-Q. Zhang, U. Fey, B.R. Noack, M. Koenig, and H. Eckelmann. On the transition of the cylinder wake. *Physics of Fluids*, 7(4):779–794, 1995.

[117] Y. Zhou and R.A. Antonia. Convection velocity measurements in a cylinder wake. *Experiments in Fluids*, 13:63–70, 1992.